

# **Sorption and diffusion of Neptunium in Opalinus Clay**

Thesis submitted for  
obtaining the degree of

Doktor der Naturwissenschaften  
doctor rerum naturalium

in Nuclear Chemistry

at the Department of Chemistry, Pharmacy, and Geosciences of the Johannes  
Gutenberg University Mainz

**Prashánta Jonathan Benjamin Börner**

Born in Kirchheimbolanden

Mainz, 2017



Dekanin: Prof. Dr. Angelika Kühnle

Date of oral examination: 14.12.2017



“I hereby declare, that I wrote the dissertation submitted without any unauthorized external assistance and used only sources acknowledged in the work. All textual passages, which are appropriated verbatim or paraphrased from published and unpublished texts as well as all information obtained from oral sources are duly indicated and listed in accordance with bibliographical rules. In carrying out this research, I complied with the rules of standard scientific practice as formulated in the statutes of the Johannes Gutenberg University Mainz to insure standard scientific practice”

Jonathan Börner



## Abstract

This thesis is about the studies on the possible migration of the long-lived and hazardous radionuclide Np from a deep geological repository for high-level nuclear waste (HLW) in argillaceous host rock into the environment. The transuranium element  $^{237}\text{Np}$  is assumed to outlive the technical barriers due to a half-life of 2.1 million years. In this regard, its retention by the geological barrier has to be investigated intensively. For this purpose the sorption, diffusion, and speciation of Np were studied in the naturally occurring Opalinus Clay (OPA), from the “Felslabor Mont Terri” in Switzerland. To further investigate the specific sorption behaviour of Np on clay mineral phases, sorption studies with kaolinite (KGa-1b) and Na-illite (illite du Puy) were performed.

These studies were funded by the Federal Ministry for Economic Affairs and Energy (BMWi) as part of the joint research project “Retention of long-lived radionuclides in natural argillaceous host rock and saline systems” to investigate the effects of temperature and salinity on the sorption and diffusion of Np in OPA. Saline systems are of highest interest, as some of the most suitable argillaceous host rock formations for a repository in Germany are located in the north. The groundwaters in this region differ from those in southern Germany due to the higher salinity. A further aim of this study was the investigation of the influence of the heat dissipation of HLW on radionuclide retention. The temperature and salinity effects were investigated in batch experiments using OPA clay powder and in-diffusion experiments using massive OPA bore cores. Both experimental methods provided sorption data, whereby additional diffusion parameters could be obtained by modeling the Np diffusion.

Based on the redox-sensitivity of Np, knowledge of the speciation is most relevant for the understanding of its migration and for more precise and reliable predictions thereof. Under natural conditions the oxidation states +V and +IV are most important for Np, where Np(V) can be seen as the mobile Np species and Np(IV), due to a lower solubility and stronger sorption, as the immobile one. For this reason, the determination of the oxidation state during the diffusion is of highest importance. The related speciation investigation was successfully done with diffusion profiles of Np in OPA using spatially-resolved synchrotron radiation for X-ray absorption near edge structure spectroscopy at the Swiss Light Source (PSI, Switzerland). The combination of this data with the related chemical images of the diffusion profiles by X-ray fluorescence and X-ray diffraction patterns for analysis of specific crystal phases of interest increased the understanding about occurring redox reactions during diffusion.





## Zusammenfassung

In dieser Arbeit wurde die mögliche Ausbreitung des langlebigen und umweltschädlichen Radionuklids Neptunium aus einem Endlager für hochradioaktiven Abfall in Tongestein in die Umwelt untersucht. Da davon auszugehen ist, dass Np mit seiner Halbwertszeit von 2,1 Millionen Jahren ( $^{237}\text{Np}$ ) die technischen Barrieren eines radioaktiven Endlagers überdauern wird, muss die mögliche Ausbreitung von Np in der sogenannten geologischen Barriere – dem umgebenden Wirtsgestein – ausführlich untersucht werden. Für diesen Zweck wurde das natürliche Tongestein Opalinuston (OPA, Mont Terri, Schweiz) ausgewählt, um Sorptions-, Diffusions- und Speziationsuntersuchungen mit Np durchzuführen. Zur genaueren Bestimmung der Sorption an den einzelnen Tonmineralphasen wurden zusätzlich Sorptionsexperimente mit Np an Kaolinit (KGa-1b) und Na-Illit (Illit du Puy) durchgeführt.

Die Untersuchungen wurden durch das Bundesministerium für Wirtschaft und Energie (BMWi) gefördert und waren größtenteils in das Verbundprojekt „Rückhaltung endlagerrelevanter Radionuklide im natürlichen Tongestein und in salinaren Systemen“ eingebunden. Salinare Systeme sind von großer Bedeutung, da sich in Deutschland einige der für ein Endlager geeigneten Gebiete mit Tongesteinsvorkommen in Norddeutschland befinden, wo das Grundwasser salzhaltiger ist, als beispielsweise in Süddeutschland. Im Rahmen dieser Arbeit sollten daher insbesondere Effekte von höher salinarem Grundwasser auf die Rückhaltung von Np in Tongestein untersucht werden. Da bei hochradioaktivem Abfall von einer starken Wärmeentwicklung auszugehen ist, lag ein weiterer Fokus dieses Projektes auf dem Einfluss höherer Temperaturen auf die Sorption und Diffusion von Np. Um dies zu erreichen, fanden zwei unterschiedliche experimentelle Methoden Anwendung. Zum einen wurden Tonsuspensionen aus gemahlenem OPA hergestellt und in Batch-Experimenten eingesetzt. Zum anderen wurden massive Bohrkerne aus OPA in Diffusionsexperimenten genutzt. Die Diffusion von Np in die Bohrkerne konnte anschließend modelliert und die entsprechenden Diffusionsparameter erhalten werden. Für Np sind unter natürlichen Bedingungen die Oxidationsstufen +IV und +V relevant. Np(V) ist hierbei als die mobile und gefährlichere Spezies anzusehen, wohingegen Np(IV) auf Grund geringerer Löslichkeiten und starker Sorption weitestgehend immobilisiert ist. Für die Abschätzung der Np Migration ist daher die Bestimmung der Speziation bei der Diffusion sehr wichtig. Dies wurde durch die Kombination unterschiedlicher orts aufgelöster röntgenspektroskopischer Methoden mittels Abtastung der Probenoberfläche durch  $\mu$ -Synchrotronstrahlung entlang von Np-Diffusionsprofilen erreicht. Das EU-Projekt TALISMAN förderte die hierfür nötigen Untersuchungen an der Swiss Light Source des Paul Scherrer Instituts (Villigen, Schweiz).

# TABLE OF CONTENTS

<b>INTRODUCTION</b> .....	1
<b>Motivation</b> .....	1
<b>Fundamentals</b> .....	11
<b>Radionuclide diffusion in argillaceous rock</b> .....	11
<b>Radionuclide retardation</b> .....	15
<b>The diffusion experiment</b> .....	19
<b>Methods of investigation</b> .....	21
<b>Analytical techniques</b> .....	21
<b>Diffusion experiments</b> .....	22
<b>OBJECTIVES AND OUTLINE</b> .....	28
<b>MANUSCRIPTS</b> .....	30
<b>Temperature and salinity dependency of the Np(V) sorption     and diffusion in Opalinus Clay</b> .....	32
<b>Speciation of neptunium during sorption and diffusion in natural clay</b> .....	35
<b>Speciation study of Np diffusion in Opalinus Clay</b> .....	37
<b>NEPTUNIUM SORPTION ON PURE CLAY MINERALS</b> .....	38
<b>Experimental</b> .....	38
<b>Determination of the correction parameter A for pH measurement         in brine solutions</b> .....	38
<b>Materials</b> .....	38
<b>Batch sorption experiments</b> .....	42
<b>XRF and XANES measurements</b> .....	43
<b>Sorption modeling</b> .....	45
<b>Investigation of diffusion experiments with imaging plates</b> .....	46

<b>RESULTS .....</b>	<b>49</b>
<b>Np(V) sorption on pure mineral phases .....</b>	<b>49</b>
<b>Diffusion experiment investigations with IPs .....</b>	<b>56</b>
<b>CONCLUSIONS AND OUTLOOK .....</b>	<b>63</b>
<b>LIST OF ABBREVIATIONS AND TERMS .....</b>	<b>66</b>
<b>REFERENCES .....</b>	<b>69</b>
<b>LIST OF FIGURES .....</b>	<b>78</b>
<b>LIST OF TABLES .....</b>	<b>81</b>
<b>ACKNOWLEDGEMENT .....</b>	<b>82</b>
<b>CURRICULUM VITAE .....</b>	<b>83</b>

# INTRODUCTION

## Motivation

The discovery of nuclear fission is a coin with two sides. There is the military application with the bombings of Hiroshima and Nagasaki on the one side and the peaceful civilian application with the biggest advantages being seemingly endless and clean energy from nuclear power plants on the other side. The word “seemingly” is used at this point to indicate that also this side of the coin has its nicks and scratches. Especially the nuclear disasters of Chernobyl (1986) and most recently of Fukushima Daiichi (2011) demonstrated the possible risks of this kind of energy. Reducing these risks is, besides climate change mitigation, one of the main objectives of the German Energiewende (energy transition). In the initial energy concept of the German federal government from 28 September 2010 the German Energiewende was still outlined with nuclear energy as an important climate-neutral bridging technology. However, this was revised six months later due to the exceptionally strong earthquakes on 11 March 2011 in Japan and the connected tsunami, which finally led to the well-known nuclear disaster of Fukushima. The subsequent final nuclear energy phase-out for Germany is planned for the end of the year 2022, with currently 9 of formerly 19 nuclear power plants which operated in the year 2001 still in operation.

The remnants of these power plants with their activation products will be a concern far beyond the end of their active lives. Many parts of the buildings on the sites of the power plants can probably be decontaminated and released from regulatory control after the accomplishment of the mandatory clearance measurements. However, the reactor containment with its steel and cement and several other parts will be highly activated, but the most dangerous remnants are the heat-generating spent nuclear fuels containing long-lived actinides and fission products. Spent nuclear fuel is called high-level waste (HLW), which is determined by high activity inventory and significant heat dissipation. This heat derives from the decay heat of the radioisotopes of the fission products and actinides. At first, the spent nuclear fuel must be stored after usage in a spent fuel pool to guarantee sufficient cooling. Further classifications of radioactive waste include intermediate-level waste (ILW) and low-level waste (LLW), both of which are not heat-generating. The specific inventory of spent nuclear fuel in Germany is given in Table 1 in kg per metric tonne heavy metal (kg/tHM).

**Table 1:** Average inventory of spent nuclear fuel in Germany, one year after removal from a reactor with initial 4%  $^{235}\text{U}$  and a burn-up of 40 GWd/t [1].

	kg/tHM
Uranium	948
Fission products	40.2
Plutonium	10.1
Minor actinides	0.83

The actinides contained in spent nuclear fuel are divided according to their quantities into the major actinides U and Pu and the minor actinides such as Np, Am, and Cm. The danger emanating from radionuclides to living beings can be described by the radiotoxicity. This takes the absorbed dose and the decay mode into consideration. Ionizing radiation from  $\alpha$ -decay is biologically the most hazardous radiation. The  $\alpha$ -particle (helium nucleus) is very short-ranged, but interacts strongly with its surrounding matter by ionization. Therefore, it is weighted higher than the  $\beta$ - or  $\gamma$ -decay.

Figure 1 shows the progression of the radiotoxicity in Sv/tHM against time in a logarithmic scale. In the first 100 years radiotoxicity derives mostly from the rather short-lived fission products  $^{137}\text{Cs}$  and  $^{90}\text{Sr}$ . While 300 years later, Am and Pu remain as major contributors to the total radiotoxicity. In contrast, the radiotoxicity of the decay chains further increases and shows a maximum in some hundred thousand years. This is similar to the radiotoxicity of Np. Its isotope  $^{237}\text{Np}$  is part of the eponymous decay chain the neptunium series, which is based on the mass numbers of  $4n + 1$ . It is not the starting point of this decay chain, but it is, compared to its predecessors  $^{241}\text{Am}$ ,  $^{241}\text{Pu}$ ,  $^{245}\text{Cm}$ , and  $^{249}\text{Cf}$ , the most stable radioisotope. This finally leads to an enrichment of  $^{237}\text{Np}$  in the spent nuclear fuel over the first thousands of years. The half-life, activity inventory, and effective dose factor for ingestion of the long-lived radionuclides contained in spent nuclear fuel are shown together in Table 2. As one can see, the transuranic elements  $^{237}\text{Np}$  (half-life 2.14 million years) and  $^{239}\text{Pu}$  (half-life 24,000 years) exhibit a hazardous combination of a long half-life, high activity inventory, and high effective dose factor. For this reason, their secure and sustained isolation from the biosphere must be ensured and therefore studied intensively.

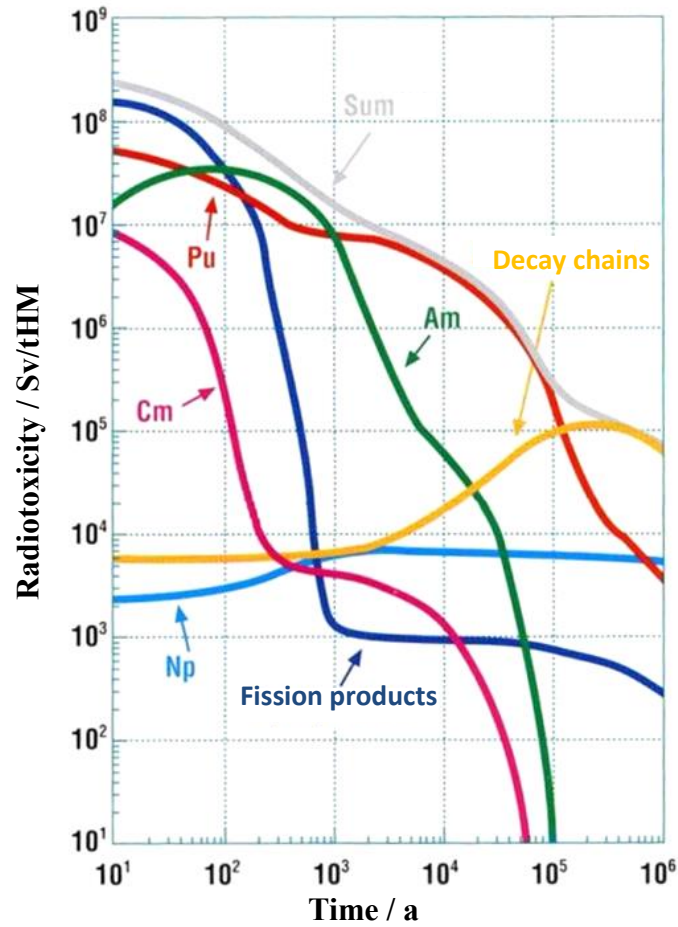


**Figure 1:** Radiotoxicity of the activity inventory per tHM from ingestion (4%  $^{235}\text{U}$ , burn-up: 40 GWd/t) [1].

**Table 2:** Half-life, activity inventory, and effective dose factor for ingestion of long-lived radionuclides contained in spent nuclear fuel [1].

Isotope	half-life / a	activity inventory / Bq/tHM	effective dose factor for ingestion / Sv/Bq
$^{93}\text{Zr}$	$1.53 \times 10^6$	$8.03 \times 10^{10}$	$2.80 \times 10^{-10}$
$^{99}\text{Tc}$	$2.13 \times 10^5$	$6.10 \times 10^{11}$	$7.79 \times 10^{-10}$
$^{129}\text{I}$	$1.57 \times 10^7$	$1.23 \times 10^9$	$1.10 \times 10^{-7}$
$^{135}\text{Cs}$	$2.30 \times 10^6$	$2.26 \times 10^{10}$	$2.00 \times 10^{-9}$
$^{237}\text{Np}$	$2.14 \times 10^6$	$1.47 \times 10^{10}$	$1.10 \times 10^{-7}$
$^{238}\text{Pu}$	$8.78 \times 10^1$	$1.39 \times 10^{14}$	$2.31 \times 10^{-7}$
$^{239}\text{Pu}$	$2.41 \times 10^4$	$1.30 \times 10^{13}$	$2.50 \times 10^{-7}$
$^{240}\text{Pu}$	$6.57 \times 10^3$	$1.96 \times 10^{13}$	$2.50 \times 10^{-7}$
$^{241}\text{Pu}$	$1.44 \times 10^1$	$5.20 \times 10^{15}$	$4.70 \times 10^{-9}$
$^{242}\text{Pu}$	$3.74 \times 10^5$	$7.92 \times 10^{10}$	$2.40 \times 10^{-7}$
$^{241}\text{Am}$	$4.33 \times 10^2$	$1.53 \times 10^{13}$	$2.00 \times 10^{-7}$
$^{243}\text{Am}$	$7.37 \times 10^3$	$7.93 \times 10^{11}$	$2.00 \times 10^{-7}$
$^{244}\text{Cm}$	$1.81 \times 10^1$	$9.72 \times 10^{13}$	$1.20 \times 10^{-7}$
$^{245}\text{Cm}$	$8.51 \times 10^3$	$7.20 \times 10^9$	$2.10 \times 10^{-7}$

Even though nuclear power plants have operated worldwide for decades, no country has so far achieved an operational final repository for HLW. HLW storage demands the highest safeguards to prevent the release of the contained activity into the environment. Furthermore, any misuse, including nuclear proliferation, must be prevented. Adequate long-term safety can be provided by the storage in a deep-geological repository hundreds of meters below the surface. Such a repository concept is passively safe and does not require intensive institutional control in the post-closure period. This is one of the safety requirements of the International Atomic Energy Agency (IAEA) for HLW repositories [2].

Before disposing of radioactive waste in a deep geological repository, the different waste categories must be further processed or conditioned. This means for LLW and ILW a transformation into a compacted, disposable form, which generally includes, for example, a solidification of liquids by evaporation or transformation into a cement or bitumen matrix, pyrolysis of organic substances or melting of radioactive metals. Spent nuclear fuel is often further treated in reprocessing plants, even though it is not mandatory. Initially, reprocessing or partitioning was developed for the construction of the nuclear bomb in the Manhattan Project during World War II [3]. However, it can also provide positive effects with regard to the environment [4]. To achieve this, the nuclear fuel rods must be dissolved, so that U and Pu can be extracted and finally reused in MOX fuel (mixture of uranium dioxide and plutonium dioxide) in an additional fuel cycle in nuclear power plants. For Germany these separated nuclides contained in liquid high-active waste concentrates (HAWC) have been vitrified in glass coquilles, which represent a very durable and resistant matrix. PUREX (Plutonium Uranium Redox Extraction) is an approved extraction method for this purpose and can also be modified to extract minor actinides [5, 6]. An additional separation of minor actinides from the HLW would reduce significantly the radiotoxicity and interim storage time due to less heat dissipation. Furthermore, the repository capacity would be increased. Nuclear transmutation and fission of the separated minor actinides by using the high neutron flux of fast reactors is well-known and feasible [7-9]. Transmutation of minor actinides could reduce the shown radiotoxicity of HLW in Figure 1 substantially, but this must be further researched. However, France and the United Kingdom are conducting research on a future nuclear fuel cycle, including partitioning, minor actinide transmutation, and related reactor technologies [10, 11].

In Europe, reprocessing plants are located in La Hague (France) and Sellafield (United Kingdom), where spent nuclear fuel from Germany was also reprocessed. In addition, the

reprocessing plant WAK (Wiederaufbereitungsanlage Karlsruhe) operated in Germany until the year 1990. There, HAWC was vitrified from 2009 until 2011.

For Germany, the reuse of spent nuclear fuel in MOX fuel is impossible in connection with the planned nuclear power phase-out. Moreover, for safety reasons the transport of spent nuclear fuel to reprocessing plants has been prohibited since 2005 and the vitrified HAWC are excluded from any reuse, as the vitrification is almost irreversible. Nevertheless, partitioning and transmutation could never have been a complete alternative for a final disposal, as HLW will always remain.

The further path for a deep geological repository in Germany has been paved by the “Arbeitskreis Auswahlverfahren Endlagerstandorte” (AkEnd) and the law of the “Standortauswahlgesetz” in 2013. Furthermore, the final report of the commission “Lagerung hoch radioaktiver Abfallstoffe” in July 2016 was an important step towards a repository [12]. This report provides numerous needed recommendations for the German Bundestag and Bundesrat. This involves, for example, recommendations for the selection process of a future repository and related exclusion criteria for the location, and the retrievability of the HLW in case of problems. Furthermore, the report also concentrates on social aspects of this process like public information and participation.

Based on this report, the amount of HLW reaches a total volume of about 30,000 m<sup>3</sup> or 17,000 tons, including the additional consumption of the present nuclear power plants until the year 2022. They will produce an additional 850 tons of spent nuclear fuel. The total volume of radioactive waste, including LLW and ILW, is expected to reach 600,000 m<sup>3</sup>. This is a factor of 20 more than for the HLW. However, 99% of all radioactivity is contained in the HLW.

The selection of the final location is set to take the whole country and all types of host rock into consideration. When the initial search for a final repository started in 1973, it was limited to salt domes as host rock. Today, also argillaceous and crystalline rocks are considered as host rocks, as is the case for other countries. Transparency is given by law for this new process with determined selection criteria and the requirements of the commission “Lagerung hoch radioaktiver Abfallstoffe”. The plan is to avoid the critical and controversial discussions which have arisen in connection with the premature selection of the Gorleben salt dome as a radioactive waste repository. However, the Gorleben site is not excluded from this process.

Despite the search for an HLW repository, several deep-geological repositories for ILW and LLW already exist in Germany or are being planned. The former iron ore mine “Pit Konrad”



(Schacht Konrad) at Salzgitter has been licensed since 2002 for the storage of 303,000 m<sup>3</sup> of radioactive waste. A plan approval decision was passed in 2007. Its conversion into a repository started in the same year and is expected to be finished in 2022 [13].

The former salt mine “Asse II” (Lower Saxony) already contains ILW and LLW. However, these wastes must be retrieved due to reports about contaminated brine solution in the repository [14]. The waste volume is estimated at 175,000–220,000 m<sup>3</sup>, including contaminated salt.

ERAM (Endlager für radioaktive Abfälle Morsleben) is a repository for radioactive waste constructed by the DDR in the former salt mine Bartensleben in Morsleben (Saxony-Anhalt). It contains 36,754 m<sup>3</sup> of ILW and LLW, which were deposited there until 1998 ([12] p. 155). The Federal Office for Radiation Protection (Bundesamt für Strahlenschutz, BfS) officially applied for initiation of a plan approval procedure according to the Atomic Energy Act (AtG) for a decommissioning of the repository, which is still in progress. The backfilling of the mine with salt concrete is expected to take a further 15–20 years. This little overview of the projects in Germany and their timescales demonstrates the great challenges, which are connected with the disposal of radioactive waste.

The general concept of a deep geological repository is shown in Figure 2. Because the waste is protected by several barriers, it is called a multi-barrier concept. The applied barriers can be further divided into the technical barriers and the natural or geological barriers. The first barrier is the solid waste form, which should fixate and incorporate the radionuclides as long as possible.

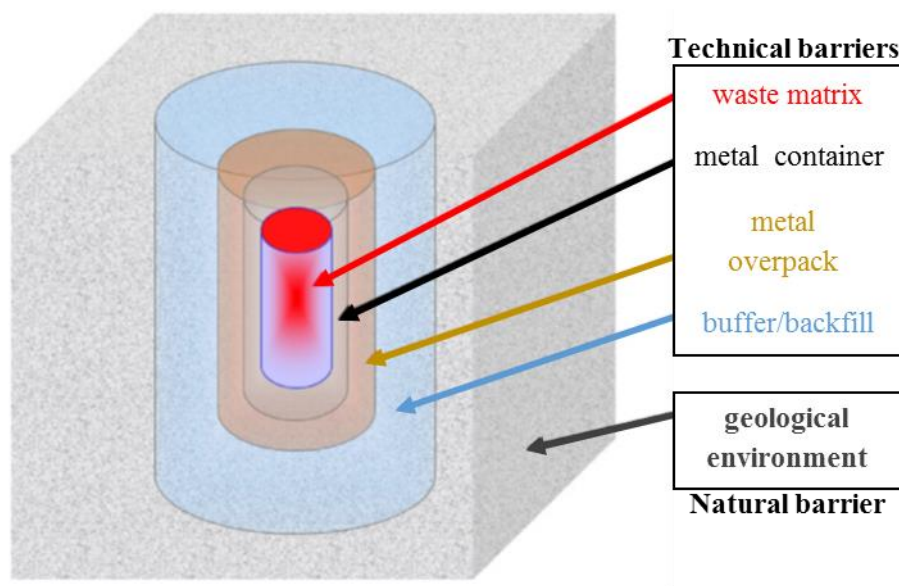


**Figure 2:** Schematic illustration of the multi-barrier concept for deep geological disposal [15].

The container for the HLW must guarantee retrievability for the whole operation time of the repository, which is supposed to be 100 years and manageability for a further 500 years after the closure of the repository. This shall guarantee that the repository can be opened and the containers taken out if necessary. Container concepts for salt rock developed in Germany in the 1980s are, for example, the POLLUX- and BSK3-container (Brennstabkanister 3). Additionally, CASTOR (cask for storage and transport of radioactive material) containers are in use for transport and temporary storage of spent nuclear and reprocessed fuel. Apart from the aspect of stability and shielding, the steel containers also provide the possibility of sufficient heat dissipation, which is very important for HLW. However, those concepts will be further adjusted to meet the requirements of the final host rock. To increase the resistance of steel containers against corrosion, different metals or materials could be used as overpack. The KBS-3 concept for repositories in crystalline rock in Sweden and Finland uses copper as overpack for the HLW canisters [16-18]. Copper is known to be very corrosion resistant and it is expected that a 50 mm thick copper overpack could increase the lifespan of the canisters to more than 100,000 years.

The waste containers are embedded in the buffer or backfill material, which is the next barrier. For argillaceous host rock the natural clay buffer bentonite will probably be used as buffer material and salt concrete for salt rock, as it was done at ERAM in Morsleben ([12] p. 155). This concept maintains as much homogeneity as possible within the host rock. Bentonite as backfill material has the great advantage that it is self-sealing in the case of water inflow into the repository. For this reason the KBS-3 concept also uses bentonite as backfill material for a repository in crystalline host rock.

The last barrier is not further a technical barrier, but the natural barrier, i.e. the specific host rock, but also the overlaying rock can provide additional protection of surface near groundwater ([12] page 333). Moreover, it could protect the effective containment zone (ECZ) against possible glacial effects in the future. These might cause additional erosion, especially in northern Europe and also northern Germany, which must be taken into account with regard to the long-term safety of a repository [19].

Since 2014 the scientific subsidies for host rock research in Germany have been divided into one third each for salt rock, argillaceous rock, and crystalline/general host rock studies. This has been probably done to avoid the appearance of any predetermination for one specific host rock ([12] page 372). However, Chapman et al. gives a good overview of the strengths and weaknesses of the investigated host rocks for HLW disposal worldwide [15]. Nevertheless, he

also stated that there is no ‘best rock’, ‘best environment’, or ‘best site’ for a repository. The demonstrated properties for volcanic tuffs refer to the unique conditions in the Yucca Mountain site (Nevada, USA) with the repository situated in a hydrogeologically unsaturated environment, due to very deep groundwater.

**Table 3:** Overview on the isolation properties of typical host rock formations as geological barriers [15].

	<b>Hard rock, such as granite</b>	<b>Argillaceous rock</b>	<b>Salt rock (Evaporites)</b>	<b>Volcanic tuffs (Yucca Mountain)</b>
<b>Heat conduction</b>	Good	Variable	Extremely Good	Good
<b>Host rock hydraulic conductivity</b>	Good	Very Good	Extremely Good	Good
<b>Stable near-field hydrochemistry</b>	Variable	Very Good	Extremely Good	Variable
<b>Low-flux geological environment</b>	Variable	Extremely Good	Extremely Good	Good
<b>Intrusion potential</b>	Good	Variable	Poor	Very Good
<b>Construction flexibility</b>	Extremely Good	Variable	Good	Very Good
<b>Gas dispersability</b>	Extremely Good	Variable to Poor	Low Relevance	Extremely Good

In Germany, the “Kommission Lagerung hoch radioaktiver Stoffe” set in its report some requirements for the host rock of a repository, which are among others ([12] page 299 ff):

- a low rock permeability ( $10^{-10}$  m/s)
- a minimum thickness of 100 m of the ECZ
- location between 300–1500 m depth (300–1000 m for clay)
- in a region without relevant seismic or volcanic activity
- the spatial expansion should reach 3 km<sup>2</sup> for salt rock and 10 km<sup>2</sup> for clay or crystalline

Fissuring in crystalline host rock formations can increase permeability extremely. This problem leads directly to an advantage of clay as host rock, which is self-sealing against water ingress and fissures. Another important advantage of clay is the very good sorption behavior concerning radionuclides. In addition, argillaceous rock is almost insoluble in natural waters. However, salt rock also has some advantages, as for example the extremely good thermal conductivity and the hydraulic conductivity. A higher thermal conductivity makes shorter interim storage times for the heat-generating HLW possible and reduces the above-mentioned spatial requirements for a repository. In salt rock the surface of the HLW container must not exceed maximum temperatures of 200 °C, which is far more than 100 °C in argillaceous rock.

Many countries are investigating argillaceous rock as a host rock for a repository. Currently, Switzerland is focusing its studies on an argillaceous rock called Opalinus Clay (OPA) and Belgium (Boom Clay) and France (Callovian-Oxfordian) are also carrying out investigations for a repository in clay rock [20-22]. In Figure 3 all argillaceous rock formations fulfilling the minimum requirements in Germany are marked green. Blue areas indicate suitable salt domes. One can see that the OPA formation from the “Zürcher Weinland” in Switzerland reaches even into southern Germany. Besides this OPA formation in southern Germany most of the suitable clay rock formations are located in the North. Besides this OPA formation in southern Germany most of the suitable clay rock formations are located in the North.

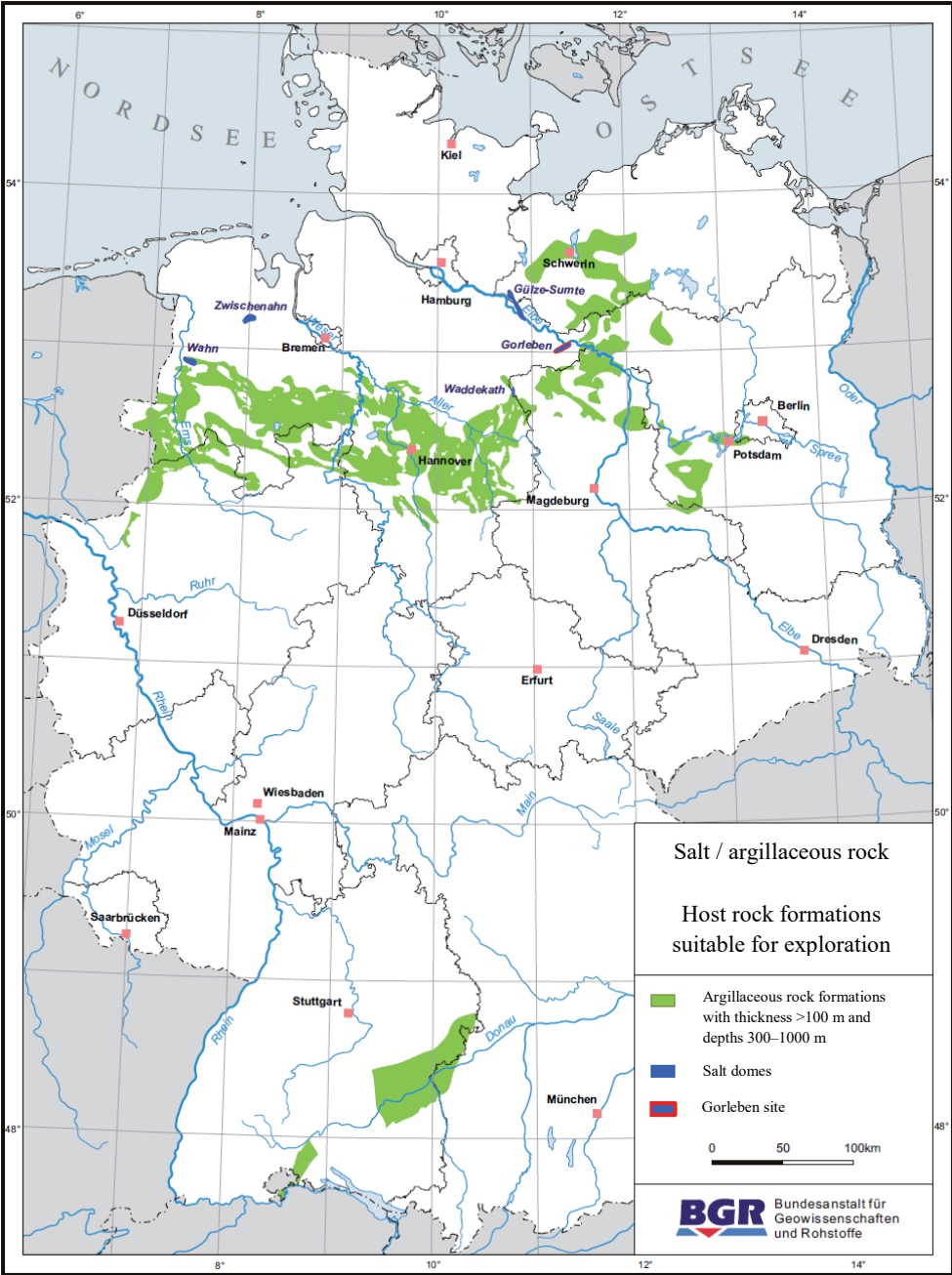


Figure 3: Overview of the salt and argillaceous rock formations suitable for a repository in Germany [23].

The geological hydrochemistry differs between northern and southern Germany with regard to the salinity of the deep groundwaters, respectively pore waters of the host rocks. The OPA pore water (OPA PW) has an ionic strength of about 0.4 M. The pore waters in northern Germany in contrast are estimated to reach into the range of saline solutions. However, specific data about the pore waters or the geochemical composition of the argillaceous rock is very limited. The composition of the OPA PW and mine water of “Pit Konrad” can be compared in Table 4 [24, 25]. “Pit Konrad” is located about 60 km south-east of Hannover and can thus be taken as a reference for the pore water conditions in the argillaceous rock formations in northern Germany in Figure 3. Both are a Na-Ca-Mg-Cl type water, but OPA PW contains far less amount of salt.

**Table 4:** Composition of OPA PW [24] compared to the mine water at pit Konrad [25].

<b>Opalinus Clay</b>				<b>Pit Konrad</b>			
cations	mol/L	anions	mol/L	cations	mol/L	anions	mol/L
Na <sup>+</sup>	0.2404	Cl <sup>-</sup>	0.2998	Na <sup>+</sup>	3.3807	Cl <sup>-</sup>	3.8239
Ca <sup>2+</sup>	0.0258	SO <sub>4</sub> <sup>2-</sup>	0.0141	Ca <sup>2+</sup>	0.223	SO <sub>4</sub> <sup>2-</sup>	0.0087
Mg <sup>2+</sup>	0.0169	HCO <sub>3</sub> <sup>-</sup>	0.0005	Mg <sup>2+</sup>	0.1136	Br <sup>-</sup>	0.0103
K <sup>+</sup>	0.0016			K <sup>+</sup>	0.0054	I <sup>-</sup>	0.0002
Sr <sup>2+</sup>	0.0005			Sr <sup>2+</sup>	0.0043	BO <sub>3</sub> <sup>3-</sup>	0.0014
				Li <sup>+</sup>	0.0001		

With regard to the safety assessment of a deep geological repository in northern Germany and the long half-life of some radionuclides like <sup>237</sup>Np, the main objective of the present work was to study the influence of high saline background electrolytes on the sorption and diffusion of Np(V) in natural argillaceous rock. As HLW causes elevated temperatures in and around the repository, an additional aspect of this work was to determine the temperature dependency of Np(V) sorption on OPA and the impact on its diffusion in OPA. Furthermore, due to the redox-sensitivity of Np its speciation was investigated along its diffusion pathway in OPA. To increase the understanding of the specific Np(V) sorption on OPA, the single clay minerals illite du Puy and kaolinite KGa-1b were used for batch sorption studies. Illite and kaolinite both are important clay minerals for OPA. To obtain pure clay mineral phases of illite and kaolinite both natural minerals passed a purification process and were used afterwards for sorption investigations.

# Fundamentals

## Radionuclide diffusion in argillaceous rock

The common transport processes for radionuclides in host rocks are considered to depend on diffusion, advection, and in some cases on gas dispersion. Advection involves a superordinate, not negligible groundwater flow, which is excluded from the predetermined repository requirement of low hydraulic conductivity [12, 20]. This means that leakage from the steel containments and the subsequent dissolution of the waste matrix is followed by the diffusion of radionuclides in the pore water of the host rock. As can be seen in Figure 4, the pore water differs depending on the nanometer or micrometer scaling. Horseman et al. defines the total matrix porosity of a clay as “the sum of the porosity associated with each of the size classes: micropores (< 2 nm), mesopores (2–50 nm) and macropores (> 50 nm)” [26], as illustrated in Figure 4. The different pore water types are connected with different diffusion mechanisms such as interlayer diffusion, surface diffusion, and the self-diffusion in the mobile pore water [26-29]. However, the importance of these diffusion mechanisms differs. According to experiments by Oscarson et al. the cationic diffusion in compacted clays can be sufficiently described by the standard pore diffusion model, disregarding surface diffusion and other mechanisms [28]. However, different aspects of the pore water shall be explained in more detail in the following paragraphs.

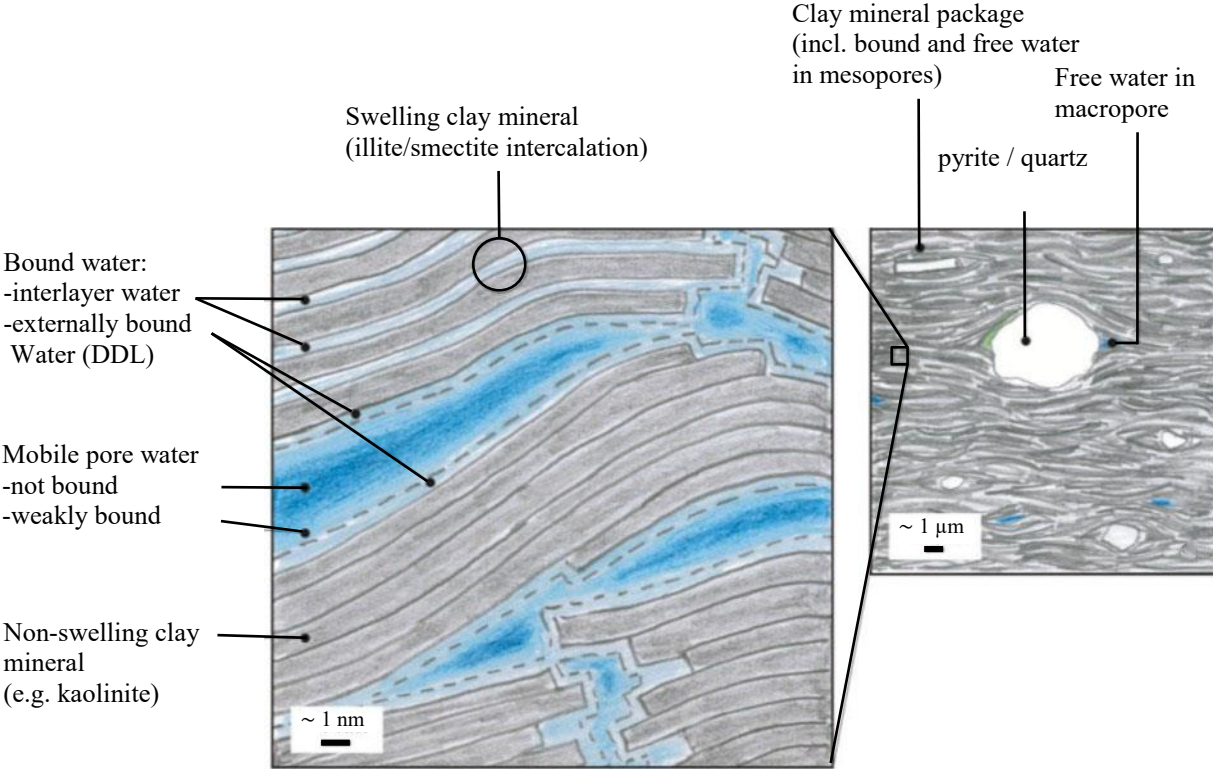


**Figure 4:** Schematic view of different types of pore water in Opalinus Clay, modified from [20].

Figure 4 demonstrates that the microscale pore waters differ. There is, for example, the mobile pore water in the interparticle pore space between clay particles or the bound pore water located next to the diffuse double-layer (DDL) on the surface of the clay minerals. The DDL arises from electrostatic attraction between the charge on the surface of particles and ions with opposite charge with relation to the surface and consists of additional water molecules. Its size and composition changes with the specific medium. It decreases with increasing ionic strength, due to the increasing polarity of the medium [30]. Furthermore, this increases the available pore space for the mobile pore water, which can influence the diffusion of some ions as shown on the left of Figure 5 [31].

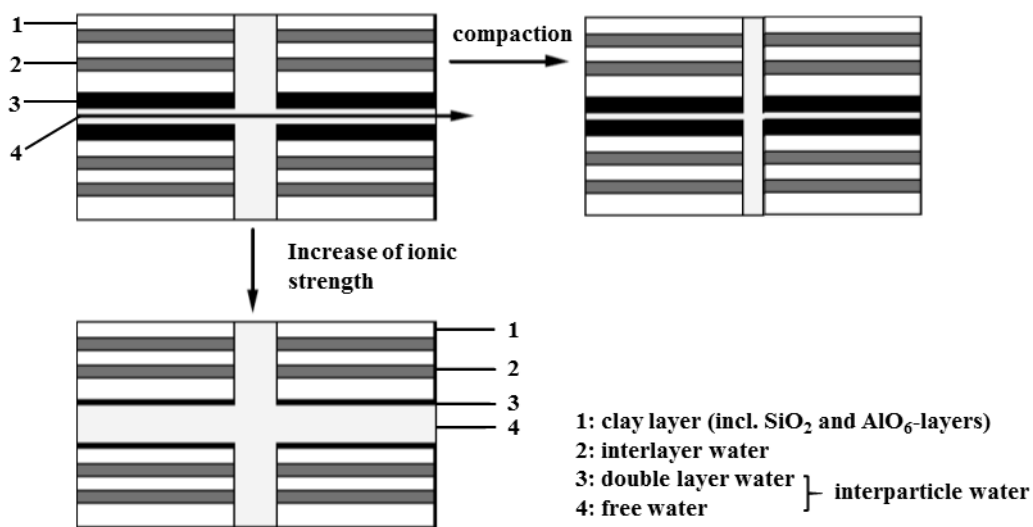


**Figure 5:** Schematic picture of the pore space of compacted bentonite and the effect of mechanical compaction and changes of ionic strength on the pore space. The total pore space equals the interlayer and the interparticle pore space. The interparticle pore space equals the double layer pore space (3) and the free pore space (4). Anion diffusion takes place in the free water pore space [31].

Depending on the pH, the silanol ( $\equiv\text{Si-OH}$ ) and aluminol ( $\equiv\text{Al-OH}$ ) groups on the clay mineral surface can become deprotonated or protonated. This leads to a changing surface charge with a tremendous effect on the diffusing ions in the pore water. The conditions for deprotonation are not identical for the silanol and aluminol groups. The silanol groups already form  $\equiv\text{Si-O}^-$  around pH 5.5, while the aluminol groups are, in general, more amphoteric with a deprotonation at a slightly higher pH [32]. The point of pH with a zero net proton charge on the mineral surface is defined as  $\text{pH}_{\text{pznpc}}$ . Above the  $\text{pH}_{\text{pznpc}}$ , the surface is negatively charged, due to deprotonation. Below the  $\text{pH}_{\text{pznpc}}$ , the surface is positively charged, due to protonation. This leads to an attraction of cations to the surface above the  $\text{pH}_{\text{pznpc}}$  and to an attraction of anions below it. The literature describes the  $\text{pH}_{\text{pznpc}}$  for the clay mineral kaolinite between 4.5 and 5.5 [33-35]. In comparison, montmorillonite shows a more basic behavior with a  $\text{pH}_{\text{pznpc}}$  in the range of 6.1–

8.5 [36-38]. The specific  $\text{pH}_{\text{pznpc}}$  for the different minerals derives from their structures. Kaolinite and montmorillonite are both sheet silicates, but montmorillonite is a 2:1 clay mineral and kaolinite a 1:1. The 2:1, or three-layer clay minerals like illite, smectite, and chlorite consist of  $\text{AlO}_6$  octahedron layers sandwiched between two  $\text{SiO}_2$  tetrahedron layers. From this alternating layer stack derives the further name TOT-layer. In contrast, there is no second  $\text{SiO}_2$  tetrahedron layer in the structure of kaolinite.

The possibility of the 2:1 clays to absorb water in the interlayer makes them swelling clays. These interlayers, shown in Figure 4 and Figure 5, are only accessible for water and cations. This derives from the above-described structure of the 2:1 clays and an exchange of some  $\text{Al}^{3+}$  ions from the  $\text{AlO}_6$  layer with cations of the charge +2. This causes a remaining negative charge in the interlayer between the 2:1 layers. This makes anion diffusion in the interlayer between the TOT-layers impossible and is called anion-exclusion effect [31].

For OPA diffusion in the interlayers might also be relevant, as OPA represents a highly compacted argillaceous rock and contains a high degree of swelling-clays [27]. Van Loon et al. studied the diffusion of  $\text{Cl}^-$ ,  $\text{Na}^+$ , and HTO in OPA and explained the decreased effective diffusion coefficient  $D_e$  of  $\text{Cl}^-$  compared to HTO by the anion-exclusion effect. [39]. This is comprehensive as the interlayer diffusion for anions is excluded. The remaining free interparticle pore space or mobile pore water is only a part of the total diffusion accessible porosity  $\epsilon$  for cations in OPA, whose size differs with compaction of the clay. Moreover, parts of the “mobile” pore water can become confined due to compaction, which can cause further changes to its properties [40].

Along with the clay particles in OPA and radionuclide diffusion, another aspect is important. The pressure of overburden forces the sheet silicates from sedimentation in random orientation into parallel layers, as shown in Figure 6. The diffusion path of ions parallel to the bedding of the clay can be more direct than the perpendicular path. This can increase the resulting effective diffusion coefficient of cations for the diffusion parallel to the bedding by a factor of about three, as shown for HTO in OPA [39].

A further complication of the modeling of the diffusion of ions in OPA derives from minerals impassable for ion diffusion, as shown in Figure 7. Grolimund et al. show a strong correlation of the  $\text{Cs}^+$  diffusion profile with clay phases, determined by  $\mu\text{-XRF}$  and  $\mu\text{-XRD}$  measurements, while the reactive transport pattern of Cs after in-diffusion was achieved by absorption-edge contrast tomography [41]. Due to the low porosity of the calcite phases,  $\text{Cs}^+$  cannot penetrate



them. In contrast, the diffusion accessible pore space in the clay phases is sufficient for  $\text{Cs}^+$  diffusion. The displayed heterogeneity of the OPA bore core can be assumed to be comparable to those in the experiments in the present work.

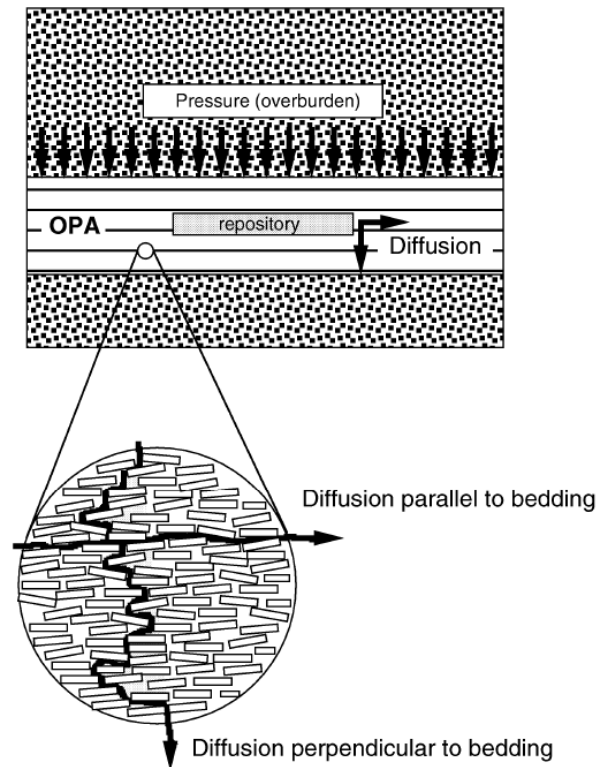


**Figure 6:** Schematic view of the anisotropy of OPA with respect to diffusion [39].

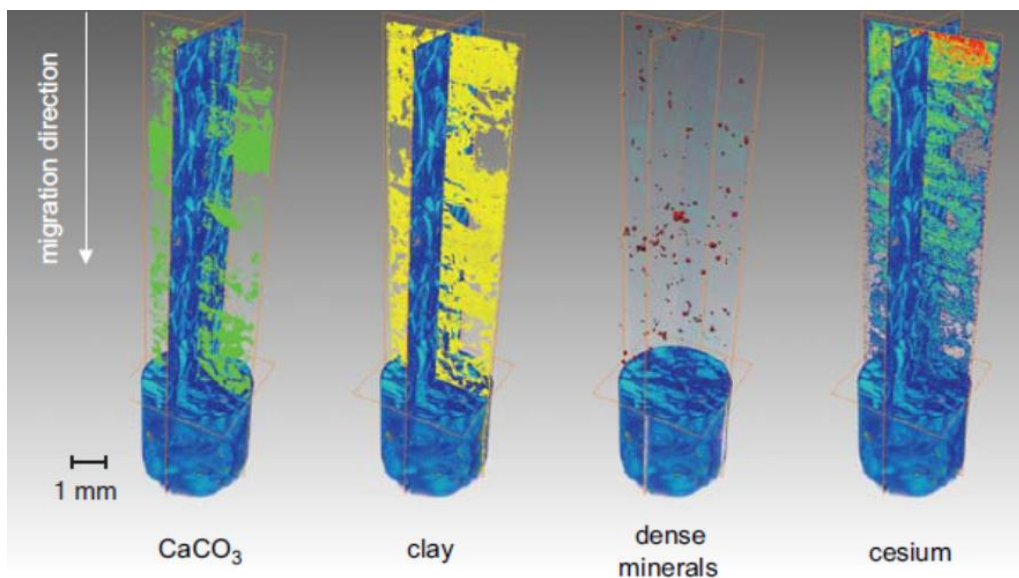


**Figure 7:** “Three-dimensional visualization of undisturbed reactive solute transport pattern and geochemical heterogeneity in an Opalinus Clay rock sample” [41]. The chemical nature of the components was assigned based on combined  $\mu$ -XRF and  $\mu$ -XRD results. The reactive transport pattern of Cs after in-diffusion is achieved by absorption-edge contrast tomography.

## Radionuclide retardation

Important parameters with regard to retardation of radionuclides are, in particular, the radionuclide solubility, the sorption behavior on the clay surfaces represented by the distribution coefficient  $K_d$ , and the aqueous complexation. The speciation is the most important information for assessing radionuclide diffusion and sorption behaviors and varies with the aqueous conditions, represented primarily by the pH and the Eh. An illustrative presentation of this information is given for Np in a Pourbaix diagram shown in Figure 8 for the system Np-O<sub>2</sub>-H<sub>2</sub>O at 25 °C.

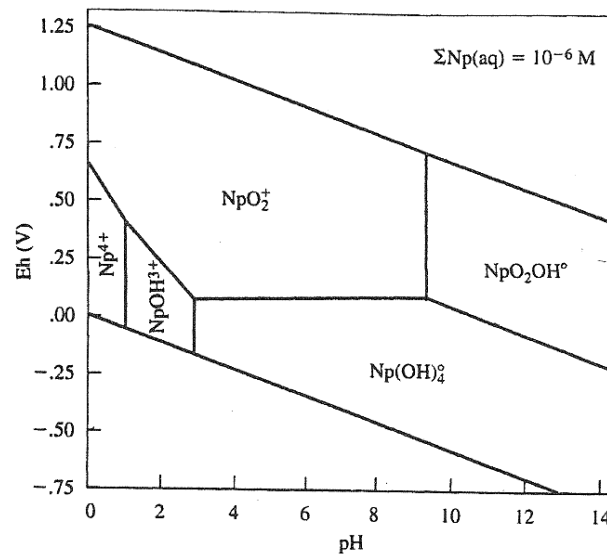
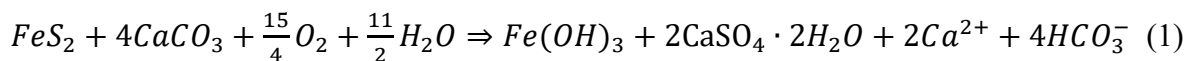


**Figure 8:** Pourbaix diagram for the system Np-O<sub>2</sub>-H<sub>2</sub>O at 25 °C [42].

The most important Np species in the near-neutral pH range are Np(V) as  $\text{NpO}_2^+$  and Np(IV) as  $\text{Np(OH)}_4$  (Figure 8). In the first hundreds of years, oxygen will be present in the backfilled repository [43, 44]. Nevertheless, the initial anaerobic stage will be finally restored as the oxygen is further consumed by reactions with some minerals contained in the host rock, as for example pyrite ( $\text{FeS}_2$ ), or it dissipates by diffusive transport. Eq. 1 shows the reaction of oxygen with pyrite in the host rock. Sulfuric acid is not expected to be formed in the buffered near-neutral pH range according to [20]. Instead,  $\text{CaCO}_3$  is dissolved and  $\text{CaSO}_4$  formed. The resulting gypsum crystals on the surface of the Opalinus clay rock were also observed at a field excursion of the Arbeitskreis Reich to the Mont Terri Felslabor in 2016.



The undisturbed, anaerobic, reducing conditions of the OPA host rock lead to an estimated Eh-value of the pore water between -0.1 and -0.3 V (SHE) as shown by Pearson et al. [45]. Under these conditions Np(IV) is the most stable Np species. These negative redox potentials can be generally expected for deep geological repositories worldwide, due to the hydrogeological saturation of the host rocks, with the exception of the previously mentioned nuclear site at Yucca Mountain, Nevada [15]. A reduction of present Np(V) to Np(IV) would be favorable with regard to the safety assessment of the repository and radionuclide migration. Np(IV) has a very low solubility ( $\sim 10^{-9}$  M at neutral pH) and is strongly sorbing [20, 46]. This makes the reduction of Np(V) to Np(IV) an important factor in the retardation, which needs to be studied further as the specific processes taking place are not fully understood. However, it is known that Fe(II) minerals contained in OPA, like pyrite and siderite can provide the pore water with  $\text{Fe}^{2+}$  cations. Due to the lower dissolution rate of siderite, pyrite is the strongest candidate for such redox reactions [44]. Furthermore,  $\text{Fe}^{2+}$  can be formed by the dissolution of the HLW steel canisters, as shown in Figure 9. A further corrosion product of the steel canisters is green rust. It consists of Fe(III) and Fe(II) cations in crystalline compounds with  $\text{OH}^-$  and anions like  $\text{CO}_3^{2-}$ ,  $\text{Cl}^-$ ,  $\text{SO}_4^{2-}$  or others.

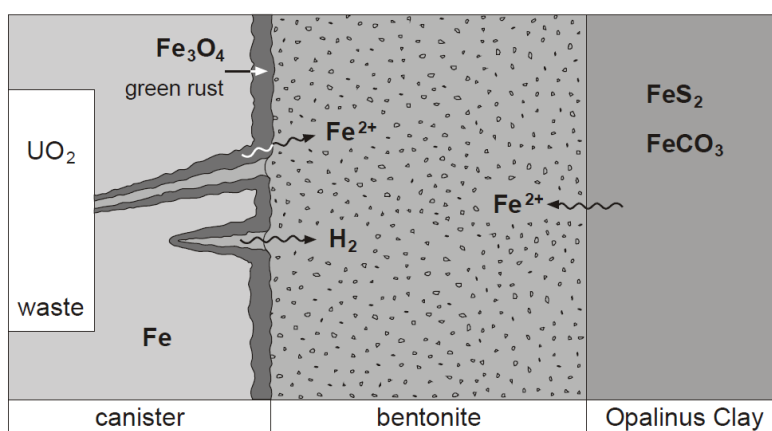


**Figure 9:** Schematic picture of major redox-active phases present in technical barrier and host rock [44].

The steel corrosion also releases the reducing agent  $\text{H}_2$  into the repository. However, with regard to argillaceous rock the relevance of the general formation of gas is somewhat higher due to the poor gas dispersability in argillaceous rock (see Table 3). This might lead to leaks from the effective containment zone because of resulting gas hyperpressure. Recently, investigations have been carried out on microbial hydrogen oxidation (and sulfur reduction) in Opalinus Clay rock and it seems that microorganisms could reduce the gas hyperpressure [47, 48]. Nevertheless, with regard to northern Germany and the high saline ground waters the problem

of steel corrosion could be further increased, as saline water is known to accelerate corrosion processes.

Fröhlich et al. provided a link between the mineral phase pyrite and the reduction of Np(V) to Np(IV) by combining  $\mu$ -XRF,  $\mu$ -XRD, and  $\mu$ -XANES measurements on a thin section sample of OPA, which was in contact with a Np(V) solution. Figure 10 shows the results of a high resolution  $\mu$ -XRF scan with a step size of 5  $\mu$ m on a pyrite particle with the related normalized Np L<sub>III</sub>-edge  $\mu$ -XANES spectra. These show an almost complete reduction of Np(V) with about 85% Np(IV) from iteration transformation factor analysis (ITFA).

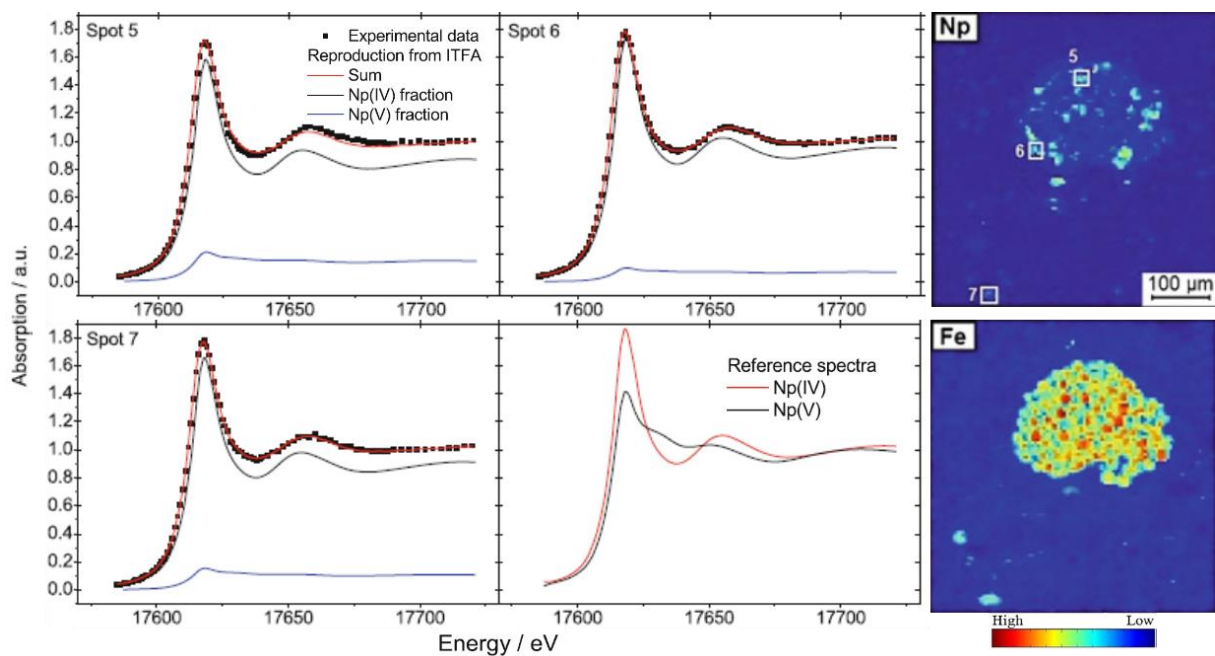


**Figure 10:** The left side shows normalized Np L<sub>III</sub>-edge  $\mu$ -XANES spectra of the marked spots on the  $\mu$ -XRF scan on the right side ( $500 \times 500 \mu\text{m}$ , step size of 5  $\mu\text{m}$ ;  $E = 17,700 \text{ eV}$ ) performed on an OPA thin section sample contacted with Np(V) [49].

Similar synchrotron-based studies were performed for different elements on hardened cement paste (HCP), which is a relevant solid waste form for ILW and LLW [50-52]. With regard to the Np speciation, Denecke et al. performed spatially resolved  $\mu$ -X-ray absorption and fluorescence investigations on a fractured granite bore core from the Äspö Hard Rock Laboratory contacted with Np(V) [53]. This study demonstrated the important role of fractures and fissures for Np migration in crystalline host rock and confirmed by  $\mu$ -XANES investigations the presence of Np(IV) particles. The measured Np(IV) hot spots correlated with

occurrences of Zn and, partially, with Fe. The size of the Np particles was estimated to be  $>10\ \mu\text{m}$ . Smaller fissures showed more Np(IV) hot spots than larger fissures, which was assumed to correlate with the local residence time.

The formation of Np(IV) particles can have a retarding effect on the one side, but it might also increase the Np(IV) mobility on the other, as those particles can have a relevant diffusion and transport behavior. Whether the retardation or mobilization is enhanced depends on the size of the particles and the available pore space of the host rock. The possible problem of a Np(IV) particle or colloid diffusion is comparable to the complexation of actinides with dissolved organic matter (DOM) in groundwater, which can increase the mobility of actinides. This relation with DOM has been shown by Zhao et al. who determined increased mobilities for U(VI), and especially for Am (III) and Pu(IV) in groundwater at the Nevada Test Site in the USA. At this location underground nuclear tests were performed until 1992 [54]. In contrast Joseph et al. found no significant effect of humic acid (HA) on the  $K_d$  and  $D_e$  at  $25\ ^\circ\text{C}$  determined by in-diffusion experiments with U(VI) and intact OPA bore cores, due to the limited pore space and the size of the HA colloids [55]. Fröhlich found et al. similar results for the diffusion of Np(V) in OPA in the absence and in the presence of HA [56]. The general possibility of the formation of Np(IV) colloids in groundwater has been shown by Husar et al., who investigated the formation of Np(IV)-silica colloids [57]. Since silicic acid might be present at concentrations in the range of  $10^{-5}$ – $10^{-3}$  M in groundwater, the formation of such colloids cannot be completely ruled out in a clay-containing environment [58].

### ***Neptunium sorption and the 2 SPNE SC/CE Model***

The uptake of radioactive elements of disposed radioactive wastes in a deep geological repository by components of the technical or geological barrier is most important for the safety assessment of such repositories and related studies.

A simple model to describe the sorption mechanism of actinides on surfaces is the two-site protolysis non-electrostatic surface complexation and cation exchange (2SPNE SC/CE) sorption model [36]. This model takes the available site types, their capacities, protolysis constants, and surface complexation constants for strong and weak sites into consideration and aims for thermodynamic sorption databases (TD-SDBs). Compared to the  $K_d$  based SDB approach the TD-SDBs make the application of results on deviating experimental conditions much easier.

The 2SPNE SC/CE sorption model has proven to be able to reproduce the sorption behavior of different metals with respect to the sorption edges and isotherms in numerous studies for the clay minerals montmorillonite and illite [36, 59-69]. With respect to natural argillaceous host rocks the 2SPNE SC/CE sorption model has shown to be capable of a “bottom-up” approach for the sorption isotherms of Ni(II), Co(II), Eu(III), Th(IV), and U(VI) on Opalinus Clay [60].

Sorption studies contained in this work have been modelled using the program Minteq [70] on basis of the 2SPNE SC/CE sorption model.

### The diffusion experiment

The general design of the diffusion experiments performed in this work is shown in Figure 11.

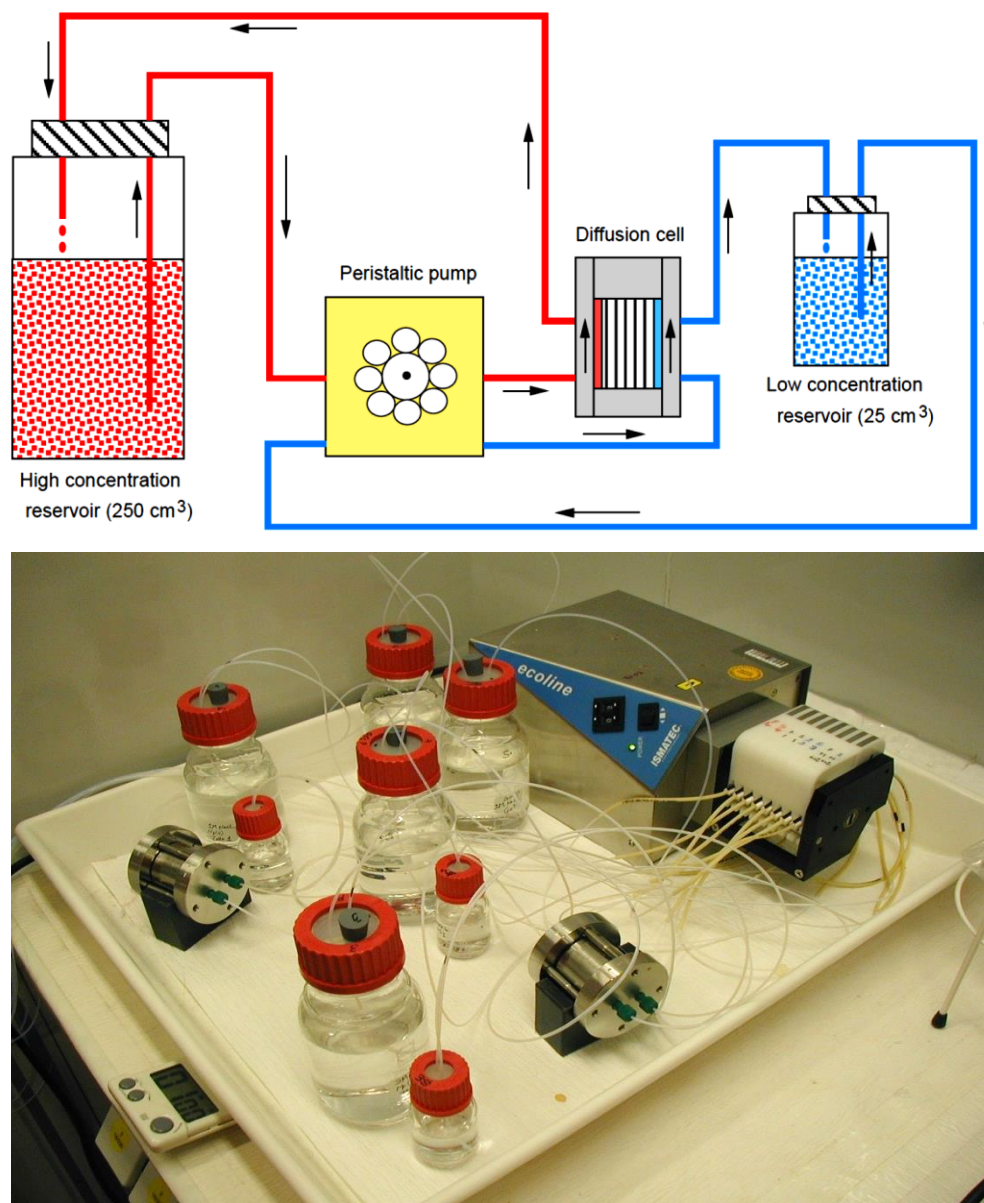


**Figure 11:** Schematic representation of the experimental set-up of a through-diffusion experiment (top) [39] and the corresponding experimental realization in the laboratory.

The cylindrical bore core is placed in a stainless steel diffusion cell allowing the respective background electrolyte solutions to circulate along both sides of the bore core. The diffusion direction can be parallel or perpendicular to the bedding of the clay. In both cases the same set-up is used, except for the different orientation of the bore cores. Further, both endings of the bore core are covered with stainless steel filter plates and end plates, which press on the bore core with defined force [39]. This is achieved by tightening the attached diffusion cell screws with a screwdriver connected with a torque indicator with a torque of 0.9 Nm. A peristaltic pump ensures the circulation of the solutions of the high- and low-concentration reservoirs along the bore core sides, which represent the solid/liquid interfaces between the bore core and the background electrolyte. The respective aliquot of radionuclide concentration for the diffusion study is added to the high concentration reservoir to achieve the needed concentration gradient.

This set-up is used for both in-diffusion and through-diffusion experiments. In through-diffusion experiments the increase of the tracer concentration was measured in the low concentration reservoirs. Therefore, the low-concentration reservoir was changed daily to determine the accumulated activity. The resulting flux  $J$  ( $\text{Bq}\cdot\text{cm}^{-2}\cdot\text{d}^{-1}$ ) was calculated by dividing the accumulated activity per day by the interface area of the bore core. Figure 12 shows the HTO accumulation in the low concentration reservoir per time unit of an HTO diffusion experiment with about  $10^{-9}$  mol/l HTO in the high-concentration reservoir. Such experiments were performed to characterize the OPA bore cores used for in-diffusion experiments with Np.

Figure 12 shows that the steady state of the flux is not achieved directly from the outset. The regression line in the right figure does not meet zero and the displayed flux on the left side increases in the first two days. From the slope  $m$  of the straight line the effective diffusion coefficient with the bore core solid/liquid interface area  $S$  ( $\text{m}^2$ ), the initial concentration  $C_0$  ( $\text{Bq}/\text{m}^3$ ), and the length of the bore core  $L$  (m) can be calculated.

$$D_e = \frac{m \cdot L}{S \cdot C_0}. \quad (2)$$

Furthermore, the rock capacity factor  $\alpha$  (–) can be calculated from the y-axis intersection point  $b$ . For the non-sorbing HTO the product of the distribution coefficient  $K_d$  ( $\text{m}^3 \cdot \text{kg}^{-1}$ ) and the density  $\rho$  ( $\text{kg} \cdot \text{m}^{-3}$ ) in Eq. 4 equals zero, so that  $\alpha$  equals the diffusion accessible porosity  $\varepsilon$  (–).

$$\alpha = \frac{-b \cdot 6}{S \cdot L \cdot C_0}. \quad (3)$$

$$\alpha = \varepsilon + \rho \cdot K_d. \quad (4)$$

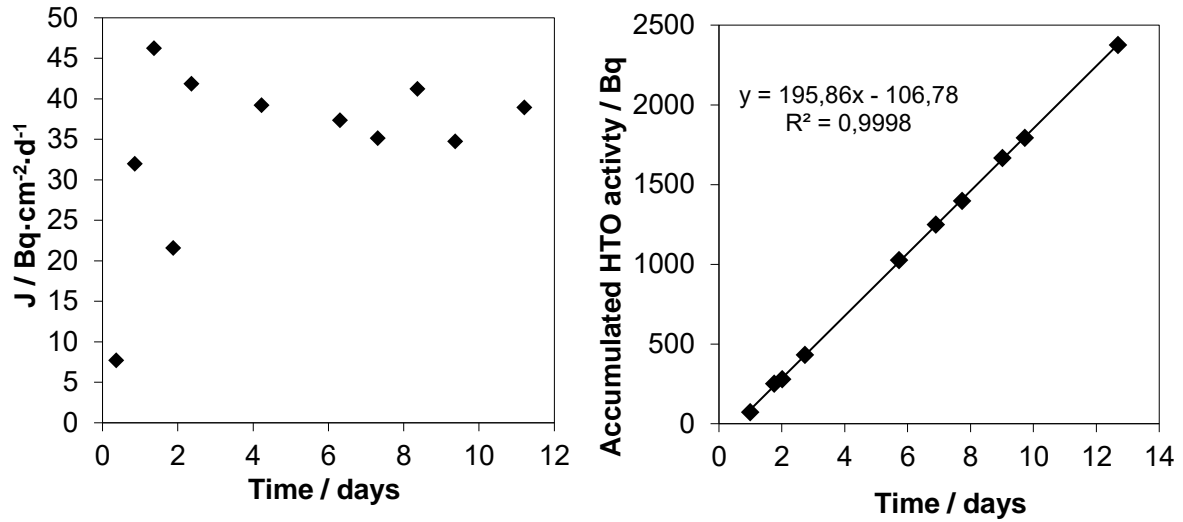


**Figure 12:** Sample results of an HTO through-diffusion experiment. Flux J and accumulated activity of HTO in the low concentration reservoir plotted against the time in days.

The resulting  $D_e$  of this specific bore core investigation with  $5 \cdot 10^{-11} \text{ m}^2/\text{s}$  would be consistent with literature values for the HTO diffusion in OPA parallel to the bedding [71]. This is about three times faster than the diffusion perpendicular to the OPA bedding with a  $D_e$  of about  $1.5 \cdot 10^{-11} \text{ m}^2/\text{s}$  [72]. For the diffusion of HTO,  $\text{Na}^+$ , and  $\text{Cl}^-$  in OPA from Mont Terri Van Loon et al. showed an increase of the  $D_e$  by a factor of four for the diffusion parallel to the bedding [73] (see also Figure 6). In contrast,  $\varepsilon$  does not depend on the bedding of the clay and has an average value of about 0.15 [72, 73], which can differ according to the heterogeneity and slightly varying amounts of mineral phases such as calcite and pyrite as shown in Figure 7.

## Methods of investigation

### Analytical techniques

Liquid-scintillation counting (LSC) and  $\gamma$ -ray spectroscopy were used for the determination of the  $^{237}\text{Np}$  and  $^{239}\text{Np}$  quantities in the diffusion or batch sorption experiment samples.

### $\gamma$ -ray spectroscopy

A coaxial semiconductor  $\gamma$ -ray detector of high-purity germanium (HPGe GMX-12180-S ORTEC, USA) was used for  $\gamma$ -ray spectroscopy, which was combined with a Canberra Inspector 2000 (model IN2K, Canberra Industries, Inc., USA). For further data processing the computer program Genie 2000 gamma acquisition and analysis software (V.3.0, Apr 05, 2004; Canberra Industries, Inc., USA) was used. The detector was frequently calibrated using a multi-element standard reference solution (QCY48, No.: R6/50/38, Amersham plc, UK).



The activity of  $^{237}\text{Np}$  in the sample was calculated from the average of the  $\gamma$ -lines at 29.4 and 86.5 keV and the  $^{239}\text{Np}$  activity from the average of the  $\gamma$ -lines at 103.4 and 106.1 keV. Each sample was measured until the net peak areas of those lines contained at least 10,000 counts.

### ***Liquid scintillation counting (LSC)***

HTO,  $^{22}\text{Na}^+$ , and  $^{237}\text{Np}$  were measured with a Hidex 300 SL LSC with alpha/beta separation by putting about 1 mL of sample solution in a 20 mL vial containing 10 mL LSC cocktail (Ultima Gold™ XR, Perkin Elmer LAS GmbH, Germany). The time of the measurements was adjusted for each sample to achieve a  $2\sigma$  error  $\leq 2\%$ .

### ***pH and Eh measurements***

A pH electrode (blue line 16 pH, Schott, Germany) connected with a pH meter (Cond pH 720, WTW GmbH, Germany) and a temperature sensor were used for pH measurements after calibration with certified buffer solutions (Schott, Germany).

The pH measurements in saline solutions acquired additional precautions, as the normal operational range with the above-mentioned electrodes is restricted to diluted solutions with ionic strengths ( $I$ ) of  $< 0.1$  M. With further increasing  $I$  the deviation between the measured pH and the actual pH in terms of the  $-\log[\text{H}^+]$  increases. Therefore, according to Fanghänel et al. the pH has to be adjusted by Eq. 5 [74]:

$$pH = pH_{exp} + A. \quad (5)$$

The pH of the solution is the sum of the measured  $pH_{exp}$  and the correction parameter  $A$ . This discrepancy is induced by different liquid junction potentials at the diaphragm of the pH electrode in saline solutions and is specific for each background electrolyte and concentration. Furthermore, the correction parameter can vary between different types of electrodes. For this reason  $A$  had to be determined specifically for each experiment and pH electrode.

### ***Diffusion experiments***

The standard in-house procedure to investigate in-diffusion experiments is the abrasive peeling method. After the diffusion experiment thin layers of the bore core are hereby stepwise removed using fine sandpaper. In each step the mass and the volume of the removed sections are measured. After that the concentration profile can be calculated by taking the measured Np activity (in Bq/g) and the related diffusion depth into account.

The obtained concentration profile can be modelled to obtain the diffusion parameters  $D_e$  and  $K_d$ . This was done using Eq. 6, which was published by Wu et al. and Yaroshchuk et al.

implementing a correction for the diffusion for the stainless steel cell filters used [72, 75]. The Np activity  $A_r$  (Bq/g) within the rock can be calculated with Eq. 6,

$$A_r = \frac{V_{pw} + m \cdot K_d}{m} \cdot C_0 \cdot C(\xi, \tau), \quad (6)$$

where  $V_{pw}$  is the volume of the specific pore water in  $m^3$ ,  $m$  the mass of the bore core in kg, and  $C(\xi, \tau)$  the inverse Fourier transformation of the concentration profile defined by Eq. 7,

$$C(\xi, \tau) = \frac{\exp(-\frac{\xi^2}{4\tau})}{\sqrt{1-4\kappa}} \left\{ \begin{array}{l} \operatorname{eerfc} \left[ \frac{\xi}{2\sqrt{\tau}} + (1 - \sqrt{1-4\kappa}) \cdot \frac{\sqrt{\tau}}{2} \right] - \\ \operatorname{eerfc} \left[ \frac{\xi}{2\sqrt{\tau}} + (1 + \sqrt{1-4\kappa}) \cdot \frac{\sqrt{\tau}}{2} \right] \end{array} \right\}, \quad (7)$$

with  $\operatorname{eerfc}(z) \equiv \exp(z^2) \cdot \operatorname{erfc}(z)$  and the following dimensionless parameters defined as  $\tau = \frac{t}{t_{ch}}$ ,  $\xi = \frac{x}{l_f}$ ,  $\kappa = t_{ch} \cdot S \cdot \frac{P_f}{V_{pw}}$ ,  $t_{ch} = \alpha \cdot \frac{D_e}{P_f^2}$ , and  $P_f = \frac{D_{fe}}{l_f}$ , with  $l_f$  (m) as the filter thickness,  $x$  (m) the diffusion distance, and  $P_f$  (m/s) the diffusion permeability of the radionuclide in the filter, the diffusion time  $t$  (s), the surface of the solid/liquid interface  $S$  ( $m^2$ ). The retarding effect of the filter is included in  $D_{fe}$  ( $m^2/s$ ), which is the diffusion coefficient of Np(V) in the stainless steel filter, as determined by Wu et al. [72].

### ***X-rays absorption and fluorescence investigations using synchrotron radiation***

The approval of beam time at the microXAS beamline (green highlighted in Figure 13) at the Swiss Light Source (SLS, PSI, Switzerland) made it possible to investigate samples of diffusion experiments using synchrotron radiation. Spatially resolved synchrotron radiation techniques were used on the surface of in-situ diffusion samples for a profound investigation. Fast micro-positioning of the sample makes it possible to scan the highly focused incident synchrotron beam with a size of a few  $\mu m$  across the sample surface. With the application of micro X-ray fluorescence ( $\mu$ -XRF) 2D diffusion profiles can be obtained. In contrast, the abrasive peeling method provides solely 1D profiles under exclusion of further spatially resolved analytical techniques. Besides  $\mu$ -XRF measurements micro X-ray absorption near-edge spectroscopy ( $\mu$ -XANES) was performed to obtain the oxidation state of the radionuclide after the diffusion experiment and micro X-ray diffraction ( $\mu$ -XRD) for the determination of mineral phases.

### ***Principle of a synchrotron facility***

A synchrotron facility is a storage ring of accelerated electrons. The electrons generate synchrotron radiation of high flux and brilliance as they pass a set of bending magnets, or undulators (Figure 13 bottom right). In total, the SLS has 20 beamlines operating, each one customized for a scientific issue, as can be seen on the left side in Figure 13. The microXAS

beamline is marked green in this figure. The standard experimental setup for  $\mu$ -XAS measurements is shown on the left side of Figure 14 and was taken from the Advanced Light Source (ALS) in Berkeley [76].

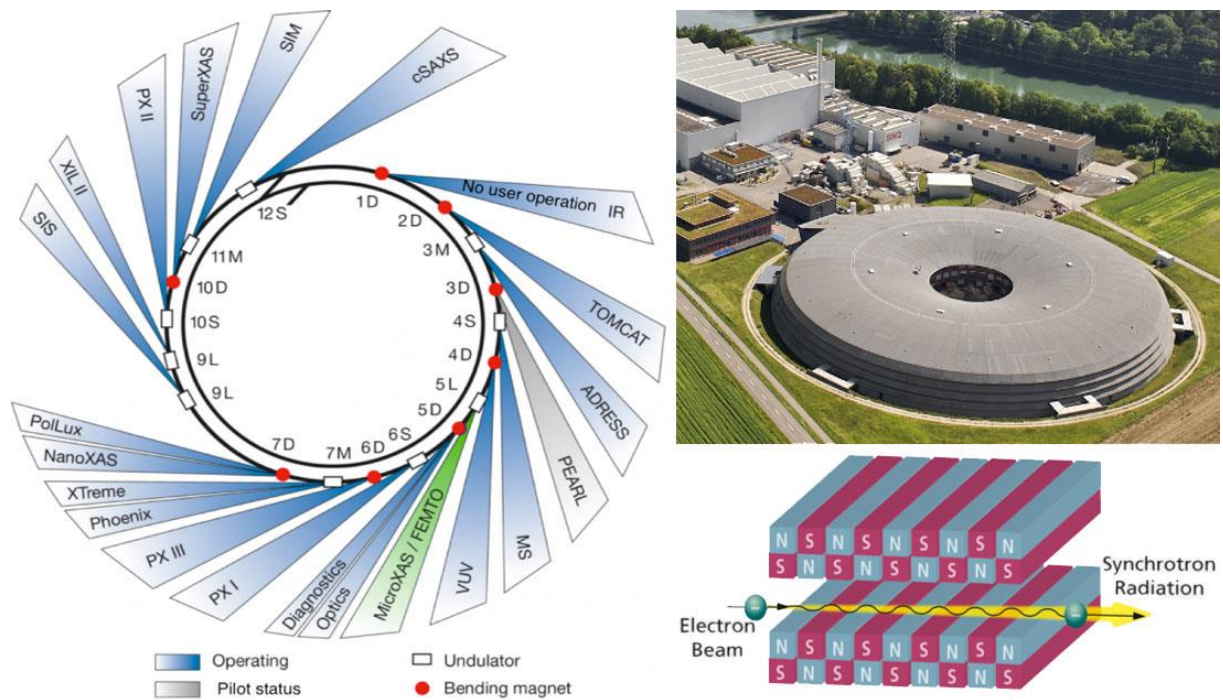


**Figure 13:** Overview of the SLS beamlines (left), aerial view of the SLS (top right) and the schematic depiction of the synchrotron radiation emitted by undulators (bottom right) [77].

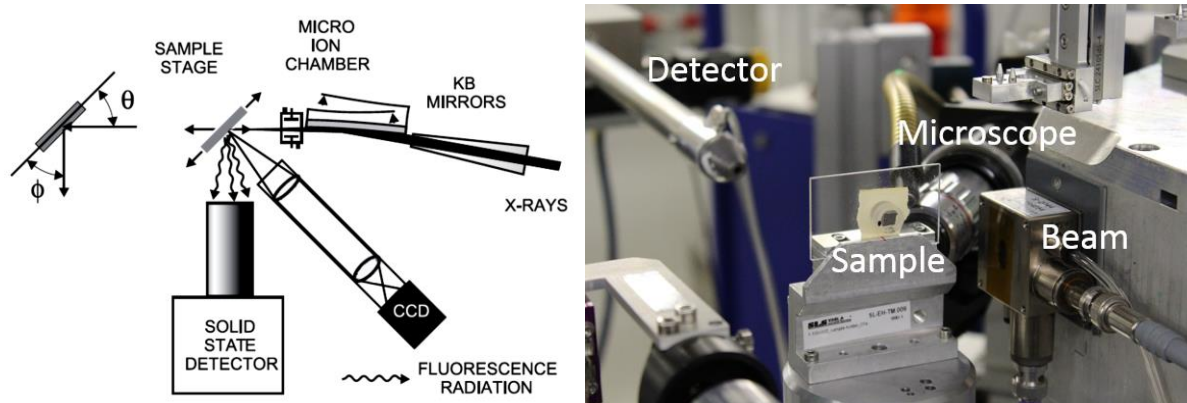


**Figure 14:** Standard  $\mu$ -XAS experimental setup in the experimental safety hutch of a beamline in a synchrotron facility (left) [76] and at the SLS, before the final sample adjustment (right).

As shown in Figure 14, the incoming X-ray beam is focused with a pair of K-B mirrors. These mirrors are named after the inventors Kirkpatrick and Baez and can focus the beam to a size of a few  $\mu\text{m}$ . The beam enters afterwards the micro ion chamber, which is used to measure the intensity. In the standard setup, the detector is orientated perpendicular to the incident beam. This annihilates the polarized background of the Compton scattering. The final positioning of the sample into the beam is executed by remote control, as the radiation exposure is too high

during the experiment. Therefore, entering the safety hutch is not permitted, which is why the photo on the right side of Figure 14 was done before the final sample arrangement.

### *Principle of X-ray fluorescence*

The simplified principle of XRF is shown in Figure 15, with electrons in shells according to their energies. If the energy of the incident X-ray beam is higher than the binding energy  $E_i$  of an electron, it can be ejected as a photoelectron. The electron shell then remains a hole, which is refilled with an electron of a higher shell with the energy  $E_j$ . This process releases the energy  $E_x = E_j - E_i$ , which is emitted by fluorescence or transferred to another electron of the atom, so that an Auger electron can be ejected.

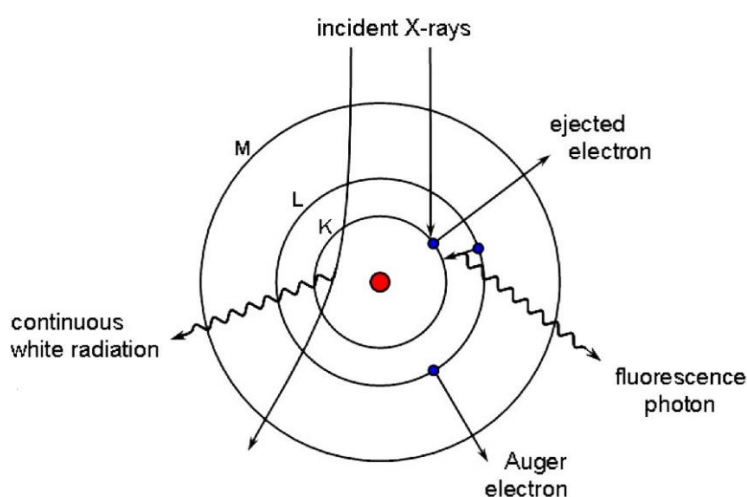


**Figure 15:** Interaction of X-rays with the electron shell of an atom [78].

### *Principle of X-ray absorption spectroscopy*

X-ray absorption spectroscopy (XAS) is used to investigate the X-ray spectroscopic signature of single or solute molecules, as only crystal structures can be investigated by XRD (X-ray diffraction). XAS provides element-specific information about the valence, bonding, and local structure. A special requirement for the application is a tunable energy of the X-ray beam. Similar to the described principle of XRF, electrons of the atoms are ejected by X-rays. For Np this is usually an electron of the  $L_{III}$  shell at about 17610 eV, followed by the characteristic emission of fluorescence. However, in an XAS experiment, the X-ray energy is tuned around this specific resonant atomic  $L_{III}$  absorption edge, at which the electron of this shell is ejected. The energy range within 40 eV of the absorption edge is called XANES (X-ray Absorption Near Edge Structure). Above this range the EXAFS (Extended X-ray Absorption Fine

Structure) range, which goes about 1 keV further, begins. The X-ray energy in the EXAFS experiment is set to a value of  $E = E_0 + \Delta E$ , above the absorption edge  $E_0$ . The energy surplus  $\Delta E$  is consumed by the kinetic energy of the emitted photoelectron, which moves, in first approximation, in a spherical photoelectron wave away from the absorbing atom with the de Broglie wavelength  $\lambda_e = h/\sqrt{2m_e\Delta E}$ . The possibility of the investigation of the atomic surrounding by EXAFS derives from the reflexion of this spherical wave on the nearest neighbour atoms, inducing constructive and destructive interferences on the absorbing atom. As one can see on the right side in Figure 16, these interferences are also visible in the small high-energy range above the absorption edge in the XANES spectra. Whether there is a constructive or destructive interference depends on the wavelength  $\lambda_e$  and the distance  $r$  between the absorbing atom and the neighboring, reflecting atoms. Both parameters are contained in Eq. 8, which describes the phase shift  $\Delta\varphi$ :

$$\Delta\varphi = 4\pi r/\lambda_e. \quad (8)$$

$\Delta\varphi$  is constructive when it is an integral multiple of  $2\pi$ . For the further calculation of the distance  $r$  a Fourier transformation is needed. However, the X-ray absorption spectroscopy in this work is restricted to XANES. Even though a small part of the EXAFS region is contained in the measured XANES, these measurements were optimized for the investigation of the Np oxidation state.

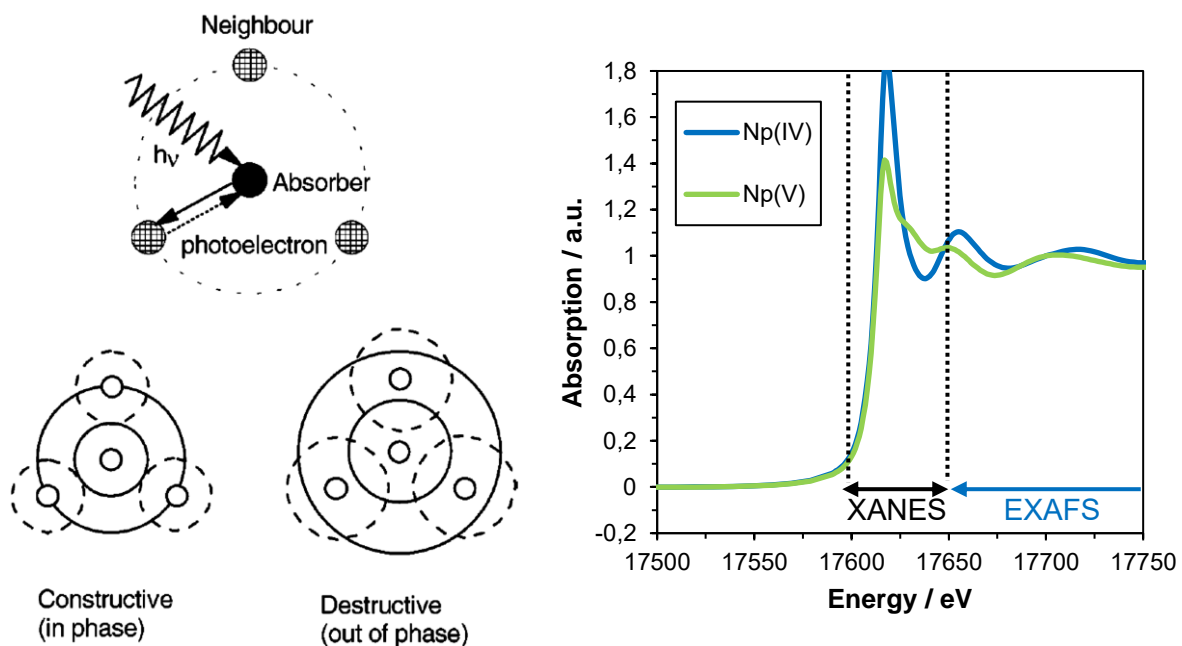


**Figure 16:** Constructive and destructive interferences in dependency of the wavelength of the photoelectron (left) [79]. XANES spectra of the  $L_{III}$ -absorption edge of aquatic Np(IV) and Np(V) species were measured by Reich et al. and used as reference spectra (right) [80].

### **Imaging plates**

The imaging plate (IP) system was originally developed by Fuji Film Co. Ltd for diagnostic radiography, which was also the manufacturer of the system used in this work. The sensitivity of an IP is a factor of  $10^3$  higher than that of conventional X-ray films and the resolution can reach  $25 \mu\text{m} \times 25 \mu\text{m}$  [81, 82]. Imaging plates are a very powerful tool for detecting radioactivity and can even detect and image the natural radioactivity in vegetables, as shown in Figure 17, even though it took 192 h [81].

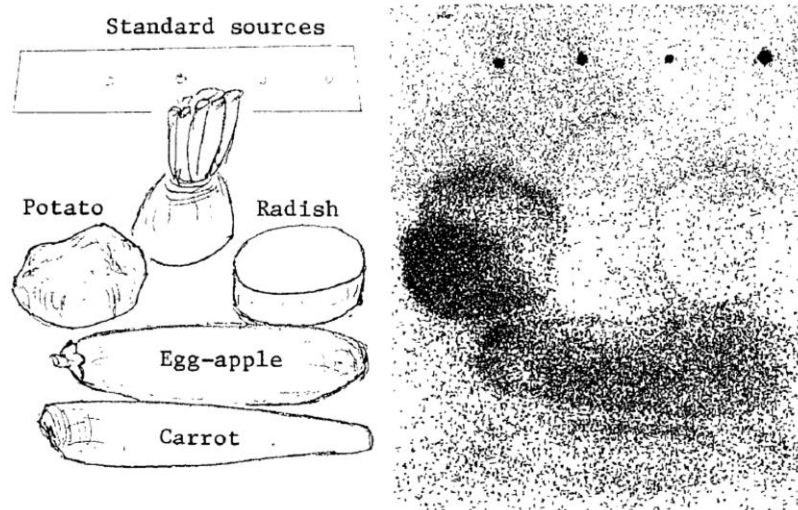


**Figure 17:** Drawing of the measuring arrangement of vegetables for IP exposure for 192 h [81].

The imaging plate consists of a flexible plastic plate coated with fine photostimulable phosphor crystals ( $\text{BaFBr:Eu}^{2+}$ ) which are combined with organic binder. A fraction of the incident energy from irradiation with X-rays, electrons or protons is stored in the phosphor crystals. This is achieved by ionization of the  $\text{Eu}^{2+}$  ions to  $\text{Eu}^{3+}$  by the incoming radiation, which provides electrons to the conduction band of the phosphor crystals. Those electrons are further “stored” in bromine vacancies from manufacturing. The IPs can be reused after exposure to visible light. This reoxidizes bromide and reduces the  $\text{Eu}^{3+}$  to  $\text{Eu}^{2+}$ , so that the initial state is restored.

## OBJECTIVES AND OUTLINE

Only a deep geological repository can guarantee the highest safety requirements, which are needed with regard to the hazardous, radioactive inventory of HLW and restrict the access for a time span of a million years. Furthermore, installing technical and geological barriers can provide further protection in case of expected leakage of radioactive waste containment. However, the work on finding a final deep geological repository for the disposal of spent nuclear fuel and other HLW in Germany has just begun.

One important concept for a repository in Germany is retrievability. Even though a retrieval of wastes would demand strong efforts, no one knows the future technical possibilities or can guarantee the safety of the repository for such a long time with respect to worst case scenarios. However, in view of the half-life of some nuclides contained in the radioactive inventory their escape from the containment seems likely and must be investigated in detail. In this regard, Np, because of its long half-life of about 2.1 million years and its very mobile species Np(V), is very relevant for such investigations. Therefore, this work focuses on the migration of Np(V) in argillaceous host rock.

Choosing argillaceous rock as host rock for a repository would have certain advantages as, for example, the radionuclide retardation on the clay surface by sorption, the self-sealing property of swelling clays in case of water intrusion and a redox environment, which might help to immobilize redox-sensitive and long-lived radionuclides like Np and Pu. However, the final decision for argillaceous rock, salt, or crystalline as host rock for a repository has not been made yet. However, concerning the radionuclide migration in the effective containment zone, the collection of robust data and reliable information is essential to make a decision on this point.

This work was funded by the Federal Ministry of Economic Affairs and Energy (BMWi) as part of a joint research project. This project focused on “retention of long-lived radionuclides in natural argillaceous host rock and saline systems” and is the continuation of a joint research project with experiments performed in diluted solutions as background electrolytes. These conditions were more similar to the common ground water conditions in Southern Germany and the natural OPA PW. The following work investigates different aspects concerning the migration of Np in OPA in accordance with the objectives of the joint research project of the BMWi.

The first manuscript investigates the effects of salinity and temperature on the sorption and diffusion of Np(V) in OPA. The influence of salinity on Np(V) sorption was investigated over a wide range of pH. The pH has a strong influence on the amount of sorption sites and the exact final local ground water conditions are yet unknown and could vary. Elevated temperatures are assumed to affect the migration of radionuclides in the host rock to a high degree so that this influence was investigated by batch sorption and diffusion experiments. The sorption of Np(V) on clay minerals is partly assumed to be an endothermic process [83, 84].

The aim of the second and third manuscripts was to understand redox and molecular-level processes of Np(V) with regard to sorption and diffusion in OPA. The identification of redox relevant mineral phases and the determination of their extent is very important for the safety assessment of a high-level nuclear waste repository. The necessary ensuing microscale speciation investigations were performed at the SLS at the Paul Scherrer Institute, by combining  $\mu$ -XANES,  $\mu$ -XRF, and  $\mu$ -XRD measurements.

In the third manuscript the spatially resolved  $\mu$ -XANES,  $\mu$ -XRF, and  $\mu$ -XRD information were obtained from  $^{237}\text{Np}$  diffusion profiles with different diffusion times and different background electrolytes. The high-saline condition experiments are of fundamental relevance regarding the argillaceous rock formations in Northern Germany. Furthermore, the  $D_e$  and  $K_d$  parameters were determined by analysis of the  $\mu$ -XRF images of the diffusion profiles.

Besides the work described in these manuscripts, batch experiments have been performed with the pure clay minerals illite (illite du Puy) and kaolinite (KGa-1b). These minerals are the most relevant 2:1 and 1:1 clay minerals contained in OPA. The understanding of sorption processes on pure clay minerals is most important to further predict the uptake of radionuclides in complex mineral and groundwater systems in a “bottom-up” approach [60].

Another approach for the analysis of Np diffusion profiles is presented in this work. IPs were used for the investigation of the same Np diffusion experiments, which were investigated by  $\mu$ -XRF at the SLS. Similar to these measurements were obtained  $D_e$  and  $K_d$  parameters from Np diffusion modelling. The results from IP were validated by comparing them with those from  $\mu$ -XRF, showing a clear value beyond measurements of the Np distribution on the contact surfaces of the bore core with the Np solution.



## MANUSCRIPTS

- (I) P. J. B. Börner, S. Amayri, R. Scholze, T. Reich  
Temperature and salinity dependencies of Np(V) sorption and diffusion in Opalinus Clay
  
- (II) T. Reich, S. Amayri, P. J. B. Börner, J. Drebert, D. R. Fröhlich, D. Grolimund,  
Speciation of neptunium during sorption and diffusion in natural clay
  
- (III) P. J. B. Börner, S. Amayri, R. Scholze, D. Grolimund, T. Reich  
Speciation study of Np diffusion in Opalinus Clay.



## **Temperature and salinity dependencies of the Np(V) sorption and diffusion in Opalinus Clay**

### **Statement about the contribution to the manuscript of the authors named:**

Responsible for the batch experiments, further data evaluation of the diffusion experiments, and final conclusions with regard to the influence of salinity or the temperature is P. J. B. Börner. The experimental work of the described diffusion experiments was performed by Dr. S. Amayri, who also performed the diffusion profile modeling. R. Scholze and Prof. Dr. T. Reich were involved in conceptual tasks and the scientific discussion.

# Temperature and salinity dependencies of Np(V) sorption and diffusion in Opalinus Clay

Prashánta J. B. Börner, Samer Amayri, Raphael Scholze, Tobias Reich

## **Abstract**

The influence of salinity and temperature on the sorption and diffusion of  $^{237}\text{Np(V)}$  was investigated by batch and diffusion experiments using the reference mineral Opalinus Clay (OPA) from Mont Terri, Switzerland. The diffusion of  $\text{NpO}_2^+$  in OPA was strongly affected by temperature and salinity. Activation energies for the diffusion of  $\text{NpO}_2^+$  (21 kJ/mol in 1 M NaCl and 18 kJ/mol in OPA pore water), HTO, and  $\text{Na}^+$  were obtained based on the effective diffusion coefficients  $D_e$  at 24 °C and 60 °C. A change of the background electrolyte solution from 1 to 3 M NaCl led to a decrease of the  $D_e$  of Np(V) by one third from  $6.9 \times 10^{-12}$  to  $2.4 \times 10^{-12}$  m<sup>2</sup>/s. Regarding the Np(V) sorption no evidence was found for temperature or salinity dependencies in diluted or saline NaCl solutions (< 3 M) by batch and diffusion experiments. In batch experiments the log  $K_d$  ( $K_d$  in L/Kg) equals 2.2 at 80 °C and 2.0 at 24 °C and in the diffusion experiments 2.5 at 24 and 60 °C.

Keywords: Neptunium, sorption, diffusion, temperature, high salinity, Opalinus Clay

## **Introduction**

The safety assessment of a deep geologic repository makes it necessary to investigate the migration of numerous hazardous radionuclides from such a containment into the environment.  $^{237}\text{Np}$ , which belongs to the long-lived transuranium elements contained in spent nuclear fuel, has a half-life time of  $2.1 \times 10^6$  years and is therefore of special concern [1, 2]. The sorption and migration behavior of Np is under investigation for different natural argillaceous host rocks in Europe, such as Boom Clay (Belgium), Callovo-Oxfordian Clay (France), and Opalinus Clay (Switzerland), but also for pure clay minerals and engineered barrier materials [1]. Due to the favorable low hydraulic conductivity ( $10^{-14}$  to  $10^{-13}$  m/s for example for OPA [3]) of argillaceous rocks, the transport of radionuclides released from a repository will be dominated by diffusion processes.

Np exists under environmentally relevant conditions in the oxidation states +IV and +V, whereby the Np(V) species ( $\text{NpO}_2^+$ ) is the more mobile and thus hazardous one. However, the tetravalent Np(IV) should be the dominant species according to the reducing conditions in the OPA host rock. Np(IV) has a very low solubility ( $\sim 10^{-9}$  M in a diluted solution at neutral pH) and is strongly sorbing [4-6]. However, oxygen might be present for at least 500 years after

closure, due to the exploration of the repository, so that the Np(V) migration still must be considered in a worst case scenario [7].

Crystalline (granite), salt, and argillaceous rocks are under discussion as possible host rocks for a deep geologic repository in Germany. Referring to argillaceous rocks, the geochemical conditions can vary widely [8]. This is reflected, for example, in the different salinities of the pore waters in Southern Germany (low salinity) and Northern Germany (high salinity) [9, 10]. Sorption experiments under high saline conditions have been recently performed for Np(V) on illite, shale, and MX-80 bentonite using different Na/Ca ratios ( $\leq 4.6$  M) [11], which is of relevance as illite is the main clay mineral contained in OPA. The authors found decreasing  $K_d$  values with increasing  $\text{Ca}^{2+}$  concentration, but no ionic strength dependency in different diluted Na-Ca-Cl brine solutions ( $1 \text{ M} < I < 4.0 \text{ M}$ , Na/Ca ratio = 2.7). Engineered barrier materials, such as MX-80 bentonite, are important components of the multi barrier disposal concept, which contains the natural host rock as last barrier for the actinide retention. Concerning OPA, the influence of different background electrolytes on the Np(V) uptake has been investigated in diluted solutions of  $\text{NaClO}_4$ , NaCl,  $\text{CaCl}_2$ , and  $\text{MgCl}_2$  at pH 7.6, showing a strong sorption reducing influence of the concentration of divalent cations [12], comparable to results of Mironenko et al. for the Np(V) sorption on montmorillonite in diluted  $\text{MgCl}_2$  and  $\text{CaCl}_2$  solutions [13].

Besides the pore water properties, the temperature is an important aspect for the Np migration. The heat dissipation of the high-level nuclear waste will increase the temperature within the repository significantly. It is planned, that the temperature of the surrounding argillaceous host rock will be kept under the temperature of its lithogenesis of about  $100 \text{ }^\circ\text{C}$ , so that any further transformations, due to elevated temperatures, can be excluded [14]. Nevertheless, according to the Stokes-Einstein equation the diffusion coefficient depends on the temperature. Several studies already investigated the influence of the temperature on the Np uptake on clay minerals in batch experiments, but the non-compliant results show the need for further investigations [12, 15, 16]. For example, Li et al. found no temperature dependence of the sorption of Np(V) on bentonite in NaCl solution [15], whereas Runde et al. found an increased sorption of Np(V) on montmorillonite, hematite, and silicate, as did Fröhlich et al. for the Np(V) sorption on OPA [12, 16].

Even though batch experiments at elevated temperatures are challenging, they are very important for a realistic prediction of the radionuclide migration. With regard to diffusion experiments with Np in argillaceous rock no results related to elevated temperatures have been

published. Wu et al. [17] determined the distribution coefficient  $K_d$  and effective diffusion coefficient  $D_e$  for Np(V) in OPA with synthetic OPA pore water as background electrolyte at 25 °C. Concerning OPA, Joseph et al. studied the influence of humic acid (HA) on the diffusion of U(VI) at 25 and 60 °C [18]. In absence of HA the diffusion of the aqueous U(VI) species was fitted with a log  $K_d$  value increased by 18% for 60 °C compared to 25 °C. The  $D_e$  increased from  $1.9 \times 10^{-12} \text{ m}^2 \text{ s}^{-1}$  at 25 °C to  $3.0 \times 10^{-12} \text{ m}^2 \text{ s}^{-1}$  at 60 °C, which resulted in a relatively low activation energy  $E_a$  of 10 kJ/mol for the U(VI) diffusion in OPA. With regard to the different interaction of both actinides with OPA, they compared the apparent diffusion coefficients  $D_a$  for U(VI) at 25 °C with a value of  $3.1 \pm 0.3 \times 10^{-14} \text{ m}^2 \text{ s}^{-1}$  with that of Np(V) in [17] with  $2.8 \pm 0.4 \times 10^{-14} \text{ m}^2 \text{ s}^{-1}$  and proclaimed from this result a similar migration for both actinides in OPA. This assumption was further supported by similar  $K_d$  values of Np(V) and U(VI) on OPA in related batch experiments with synthetic OPA pore water [17-19]. Nevertheless, the  $D_e$  for  $\text{NpO}_2^+$  in OPA in [17] is still slightly higher than that for  $\text{UO}_2^{2+}$  in [18]. This corresponds to the calculated diffusion coefficients of actinyl ions in pure water, which can be explained by the higher effective charge number of the  $\text{UO}_2^{2+}$  [20].

The present work investigates the influence of background electrolytes (NaCl,  $\text{MgCl}_2$ ) and salinity on the sorption and diffusion of Np(V) on and in OPA. Furthermore, the influence of temperature on the Np uptake on OPA and its migration was studied in different NaCl solutions by diffusion and batch experiments. The obtained results from batch and diffusion experiments are valuable parameters for transport modeling of Np in OPA, as there is only little Np(V) diffusion data available.

## ***Experiments***

### **Materials**

**Opalinus Clay (OPA):** The Opalinus Clay in this work originates from the Mont Terri Rock Laboratory, Switzerland. OPA is a heterogeneous argillaceous rock, which consists of several different minerals. We used the so-called sandy OPA fraction, which contains besides several clay minerals ( $22 \pm 2\%$  kaolinite,  $23 \pm 2\%$  illite,  $11 \pm 2\%$  illite/smectite and  $10 \pm 2\%$  chlorite),  $14 \pm 4\%$  quartz,  $13 \pm 8\%$  calcite,  $4 \pm 2\%$  Fe(II)-bearing minerals (pyrite und siderite), small amounts of albite ( $1 \pm 1\%$ ), K-feldspars ( $1 \pm 2\%$ ), and organic carbon ( $1 \pm 1\%$ ) [5]. The trace element concentration was measured by X-ray fluorescence analysis and published in [21]. More detailed information about the main physicochemical characteristics of the Mont Terri Opalinus Clay can be found in the NAGRA technical report 02-03 [5].

The argillaceous rock cylinders for the diffusion studies were prepared out of intact OPA bore cores (BLT 14). The OPA powder used in the batch experiments was prepared from crushed and grinded bore cores and stored either under aerobic (BHE 24/1, depth 3.30–3.56 m) or anaerobic (BHE 24/2, depth 3.56–3.89 m) conditions.

The cation exchange capacity (CEC) of the aerobic powder (BHE 24/1) equals to  $10 \pm 4$  meq/kg and the specific surface area (SSA) determined using the N<sub>2</sub>-BET method equals to  $41.3 \pm 0.5$  m<sup>2</sup>/g [19].

All sample solutions were prepared using Millipore water (18 MΩ, Synergy™ Millipore water system, Millipore GmbH, Schwalbach, Germany) and p.a. chemicals. The composition of the synthetic OPA pore water is shown in Table 1 with an ionic strength of approximately 0.4 M and pH 7.6 [10]. To prevent any bacterial growth during the diffusion experiments, we added  $1 \cdot 10^{-3}$  M NaN<sub>3</sub> to the reservoirs.

**Table 1:** Composition of synthetic OPA pore water [10].

Salt	Concentration in g/L
NaCl	12.38
KCl	0.12
MgCl <sub>2</sub> × 6H <sub>2</sub> O	3.48
CaCl <sub>2</sub> × 2H <sub>2</sub> O	3.79
SrCl <sub>2</sub> × 6H <sub>2</sub> O	0.14
Na <sub>2</sub> SO <sub>4</sub>	2.00
NaHCO <sub>3</sub>	0.04

**Neptunium stock solution:** Stock solutions of <sup>237</sup>Np(V) and <sup>239</sup>Np(V) were prepared by the same procedure as described in detail elsewhere [22]. The oxidation state of the <sup>237</sup>Np stock solution was verified by UV-Vis absorption spectroscopy with the characteristic absorption band of Np(V) at 980.4 nm. The concentrations of <sup>237</sup>Np and <sup>239</sup>Np were determined by γ-ray spectroscopy using the γ lines at 29.37 keV and 86.48 keV for <sup>237</sup>Np and 103.37 keV and 106.12 keV for <sup>239</sup>Np, respectively. The resulting stock solutions had a pH of about 1.5 and a concentration of  $8 \times 10^{-3}$  M <sup>237</sup>Np(V) and  $8 \times 10^{-9}$  M <sup>239</sup>Np(V). The pH of the Np stock solutions was adjusted to ~4 using 5 M NaOH before adding aliquots to the samples.

### Batch sorption studies

In experiments with a high Np concentration, <sup>237</sup>Np was spiked with <sup>239</sup>Np ( $t_{1/2} = 2.36$  d) for higher count rates. Experiments at low Np concentration ( $\leq 10^{-10}$  M) used exclusively <sup>239</sup>Np.

Batch sorption experiments under anaerobic conditions were performed in an argon glove-box ( $\text{Ar} \geq 99.99\%$ ,  $c_{\text{O}_2} < 0.1$  ppm) to exclude oxidation processes by  $\text{O}_2$  and to eliminate carbonate complexation by dissolved  $\text{CO}_2$ . Aerobic batch experiments were carried out under ambient air conditions, with addition of  $\text{NaHCO}_3/\text{Na}_2\text{CO}_3$  solutions for  $\text{pH} > 7$  for a faster equilibration of the suspensions with atmospheric  $\text{CO}_2$  ( $p_{\text{CO}_2} = 10^{-3.5}$  atm). The concentration of  $\text{CO}_3^{2-}$  in solution was calculated with the speciation software Visual Minteq V. 3.0 [23]. The suspensions were left for preconditioning on an end-over-end rotator (SB 3, Stuart Scientific, UK) for 72 h.

In pH measurements in high saline solutions one has to take into account deviating measured pH values, due to different liquid junction potentials at the pH electrode at higher electrolyte concentrations, which has been described in detail in [24]. Beyond the concentration range of the Debye-Hückel theory, each measured pH value was corrected by an empirical value, which has been determined by the pH electrode used in each saline solution before the start of the experiment.

The general experimental procedure of the batch experiments was analogous as described in [12], except that the suspensions of the batch experiment at  $80^\circ\text{C}$  were prepared in 50 mL centrifuge tubes (Beckman Coulter, USA), equipped with an appropriate magnetic stirrer and placed in a massive aluminum block with separate boreholes for the samples. This aluminum block was placed on a heatable multipoint magnetic stirrer (RT 10 power IKAMAG, IKA, Germany) and calibrated for the desired temperature  $\pm 3^\circ\text{C}$ . All used buffers and solutions were pre-tempered at  $80^\circ\text{C}$  to avoid temperature fluctuations and the samples were steadily weighed in to check the evaporation during the pH adjustments. Any evaporated water was immediately replaced with Millipore water to prevent any precipitations.

The percentage sorption derives from eq 1 and the distribution coefficient from eq 2.

$$\text{Sorption\%} = \left(1 - \frac{[\text{An}]_{\text{eq}}}{[\text{An}]_0}\right) \cdot 100\%. \quad (1)$$

$$K_d = \frac{V}{m} \cdot \left(\frac{[\text{An}]_0 - [\text{An}]_{\text{eq}}}{[\text{An}]_{\text{eq}}}\right), \quad (2)$$

where  $[\text{An}]_{\text{eq}}$  (mol/L) is the radionuclide concentration in equilibrium (concentration in the supernatant),  $[\text{An}]_0$  (mol/L) is the initial concentration of the radionuclide,  $V$  ( $\text{m}^3$ ) is the sample volume and  $m$  (kg) is the mass of sorbent.



## Diffusion experiments

### *General procedure of diffusion experiments*

The diffusion experiments used OPA cylinders of about 25 mm diameter and 11 mm thickness, prepared from the aerobic OPA bore core (BLT 14), sandwiched between two stainless steel filter plates and mounted in a stainless steel diffusion cell. The direction of transport was perpendicular to the bedding of the clay. The average dry density of the intact OPA was about 2400 kg/m<sup>3</sup>.

OPA pore water, 1 M NaCl, and 3 M NaCl solutions were used as mobile phases. All diffusion experiments were carried out under ambient air (aerobic conditions) and the temperature was either  $24 \pm 2$  °C (room temperature) or  $60 \pm 2$  °C. The experimental setup followed the procedure of the through-diffusion experiments by Van Loon et al. [25]. Detailed information about our diffusion setup can also be found in [17]. To achieve an equilibrium between the OPA sample and the mobile phase, the sample was contacted from both sides with the respective solution for at least 5 weeks.

To determine the porosity of the used OPA bore core samples and to ensure for their proper inner conditions through-diffusion experiments with HTO and <sup>22</sup>Na<sup>+</sup> were conducted. The initial activity in the high concentration reservoir was  $1 \times 10^9$  Bq/m<sup>3</sup> each and the accumulated activity in the low concentration reservoir measured by LSC. These measurements were followed by an out-diffusion of those radionuclides. This was done by replacing both reservoirs with fresh vials containing the respective mobile phase without any radiotracer. The vials were changed daily until no activity was detectable in the reservoirs. The out-diffused amount of HTO/<sup>22</sup>Na<sup>+</sup> was also measured by LSC. Once the out-diffusion was finished, we spiked the primary reservoir with <sup>237</sup>Np(V) to obtain a concentration of  $8 \times 10^{-6}$  M and started the in-diffusion experiment for 40 to 76 days. Samples of 0.5 mL were taken on regularly time basis from the primary reservoir to measure the decrease in activity, which indicates the amount of Np that diffused into the OPA sample. Close to the end of the Np diffusion experiment, the high-concentration reservoir was exchanged by a smaller vial (20 mL) containing the same concentration of Np(V), and in addition <sup>22</sup>Na<sup>+</sup>. Around 20 hours after exchanging the high-concentration reservoir, the diffusion was terminated.

For the analysis of the in-diffusion experiments each OPA bore core was removed from the diffusion cell and attached to a sample holder for abrasive peeling with P220 abrasive paper as described elsewhere [17, 26]. The peeled OPA layers were measured by  $\gamma$ -ray spectroscopy to determine the <sup>237</sup>Np (at 29.37 keV and 86.48 keV) and <sup>22</sup>Na<sup>+</sup> (at 1274.5 keV) concentrations.

The diffusion experiments at  $60 \text{ }^\circ\text{C} \pm 2 \text{ }^\circ\text{C}$  were carried out in an incubator (INE-200 heating incubator, Memmert GmbH, Germany).

The data analysis for through-, out-, and in-diffusion experiments was done with an in-house developed computer code as described in detail elsewhere [3, 17]. An overview of the different diffusion experiments is given in Table 2.

The obtained effective diffusion coefficient ( $D_e$ ), accessible porosity of the clay ( $\varepsilon$ ), and the rock capacity factor ( $\alpha$ ) were calculated using the equation given by Van Loon et al. [27]. The distribution coefficient ( $K_d$ ) of  $^{22}\text{Na}^+$  was calculated from the rock capacity factor under the assumption that the diffusion-accessible porosity of  $^{22}\text{Na}^+$  is the same as for HTO. The rock capacity factor  $\alpha$  is described by eq 3, with the diffusion-accessible porosity  $\varepsilon$ , the bulk dry density  $\rho$  in  $\text{kg}/\text{m}^3$  and the distribution coefficient  $K_d$  in  $\text{m}^3/\text{kg}$ .

$$\alpha = \varepsilon + \rho \cdot K_d. \quad (3)$$

The diffusion parameters ( $D_e$ ,  $\varepsilon$ ,  $\alpha$ ) were obtained by fitting the results of the experimental data of the transient and steady state phases to an analytical solution of the accumulated activity. The quality of the derived  $D_e$  and  $\alpha$  values was tested by using them as input parameters to calculate the flux (eq 4).

$$J(L, t) = \frac{1}{S} \cdot \frac{\partial A}{\partial t}, \quad (4)$$

where  $J(L, t)$  is the flux at the low-concentration boundary ( $x = L$ ) at diffusion time  $t$ ,  $A$  ( $\text{Bq}/\text{m}^3$ ) the radionuclide activity in solution,  $t$  (s) the diffusion time and  $S$  ( $\text{m}^2$ ) the cross section area of the sample. If the diffusion parameters for HTO and  $^{22}\text{Na}^+$  were in good agreement with known values from the literature [25], the integrity of the OPA sample was assumed. A general description of the diffusive flux is given by eq 5, Fick's first law:

$$J = -D_e \cdot \frac{\partial c}{\partial x}, \quad (5)$$

where the effective diffusion coefficient  $D_e$  is multiplied with the concentration gradient from the high to the low concentration reservoir. The rock capacity factor  $\alpha$  connects the effective diffusion coefficient  $D_e$  with the apparent diffusion coefficient  $D_a$ .

$$D_a = \frac{D_e}{\alpha}. \quad (6)$$

**Table 2:** Experimental details of the prepared diffusion cells under ambient air at pH 7.6.

Cell	Temp. / °C	Mobile phase	Diffusion time /d	ø / mm	l / mm	ρ / kg/m <sup>3</sup>
1	24	1 M NaCl	63	25.48	11.00	2346
2	24	3 M NaCl	67	25.42	10.90	2363
3	60	1 M NaCl	40	25.40	11.00	2377
4	60	OPA PW	67	25.45	11.00	2353

### *Influence of the background electrolyte and temperature*

To study the influence of the background electrolyte NaCl and its ionic strength on the diffusion of Np(V) in OPA, two diffusion cells using 1 M and 3 M NaCl as mobile phase were prepared and characterized as described in 0. The obtained results were compared with previous diffusion studies using OPA pore water as background electrolyte [17]. Different background electrolytes and concentrations can influence the diffusion of an ion or particle on the basis of a changed viscosity or a different complexation and interaction with the solvent. The Stokes-Einstein equation connects the force of friction known from Stokes' law with the diffusion coefficient  $D$  and the temperature  $T$ :

$$D = \frac{k_B \cdot T}{6 \cdot \pi \cdot \mu \cdot r}, \quad (7)$$

where  $D$  is the diffusion coefficient (m<sup>2</sup>/s),  $\mu$  is the dynamic viscosity,  $r$  the Stokes radius or hydrodynamic radius of the spherical particle,  $k_B$  is the Boltzmann-constant (1.3807·10<sup>-23</sup> J/K), and  $T$  the absolute temperature (K). One can see that the diffusion is proportional to the temperature and anti-proportional to the viscosity of the solvent. To investigate the influence of elevated temperatures on the diffusion of Np(V) in OPA two diffusion cells equipped with cylinders of intact OPA were prepared at 60 °C. One cell used 1 M NaCl and the other synthetic OPA PW as mobile phase, both at pH 7.6. The relation of the diffusion and the activation energy of the diffusion  $E_a$  (kJ/mol) is given by the Arrhenius eq [28]:

$$D = A \cdot e^{\frac{-E_a}{R \cdot T}}, \quad (8)$$

where  $A$  (m<sup>2</sup>/s) is the Arrhenius parameter and  $R$  (8.314 J/mol·K) the gas constant. The activation energy for the diffusion can be estimated by plotting  $\ln D_e$  versus  $1/T$  in a so-called Arrhenius plot.

## Results and discussion

### Sorption experiments

#### *Effect of salinity on Np(V) sorption*

Figure 1 shows the  $\log K_d$  values for the Np(V) sorption on OPA (15 g/L) at pH 7.6 for varying NaCl concentrations (0.1–2.8 M) and Np(V) start concentrations  $c_{\text{tot}}$  in the range of  $10^{-14}$ – $10^{-5}$  M under aerobic conditions, without leaving the range of solubility. The  $\log K_d$  values of Np(V) are constant in the low concentration range up to  $10^{-9}$  M, which demonstrates ideal sorption behavior, according to Freundlich [29]. This furthermore accounts for the abundance of strong sites in relation to Np(V), so that the sorption solely depends on the degree of complexation of Np(V) in solution. As the Np(V) concentration rises, the strong site capacities of the clay minerals get gradually exhausted and the  $\log K_d$  value decreases. Nevertheless, most relevant for environmental aspects is probably the low concentration range with ideal sorption behavior and a  $\log K_d$  of about 2.7 ( $K_d$  in L/Kg). Furthermore, no significant influence of the NaCl ionic strength on the sorption of Np(V) on OPA was found.

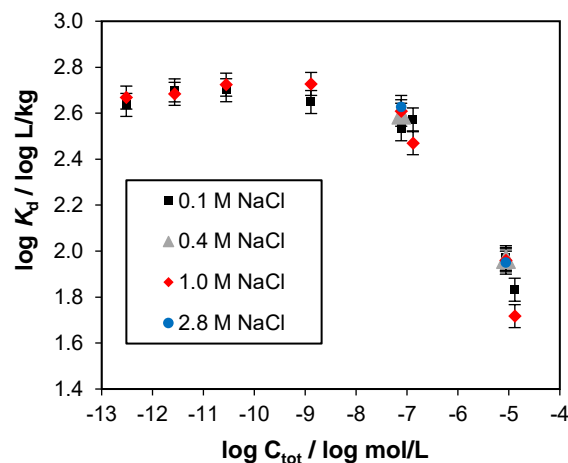


**Figure 1:**  $\log K_d$  for the sorption of Np(V) on OPA (15 g/L OPA) as a functions of the total Np(V) concentration  $C_{\text{tot}}$  at pH 7.6 under aerobic conditions for 0.1–2.8 M NaCl solutions.

The clay pore waters of Northern Germany contain besides high NaCl concentrations elevated concentrations of divalent cations such as  $\text{Ca}^{2+}$  and  $\text{Mg}^{2+}$  [9]. For the investigation of the effect of divalent cations on the sorption of Np(V) on OPA in high saline solutions, batch experiments were performed under aerobic and anaerobic conditions with Np(V) concentrations of  $8 \times 10^{-6}$  M in solutions of ionic strengths  $I$  of 0.1 and 3.0 M  $\text{MgCl}_2$  ( $c = 0.033$  and 1.0 M, respectively) over a pH range of 3.5–8.5. The maximum pH is limited by the precipitation of  $\text{Mg}(\text{OH})_2$  in the alkaline region.

The presented results in Figure 2 show a significant influence of the concentration of the divalent cation  $\text{Mg}^{2+}$ . The sorption on OPA starts to rise for both ionic strengths above pH 5.5

and increases to 80% in 0.1 M MgCl<sub>2</sub> solution, but shows in 3.0 M MgCl<sub>2</sub> significantly less sorption with only 50%. The sorption results for 0.1 M MgCl<sub>2</sub> can be furthermore validated by those in [12], as both experiments show matching log  $K_d$  values at similar conditions. These account in [12] for a log  $K_d$  of  $1.8 \pm 0.1$  ( $K_d$  in L/Kg) at pH 7.8 and in this study for  $1.7 \pm 0.1$  ( $K_d$  in L/Kg) at pH 7.7.

Figure 3 compares the results of the Np(V) sorption experiments in NaCl and MgCl<sub>2</sub> solutions at pH 7.6 with the results of Np(V) sorption in synthetic OPA pore water [12] (ionic strength of 0.4 M and pH 7.6) under ambient air conditions.

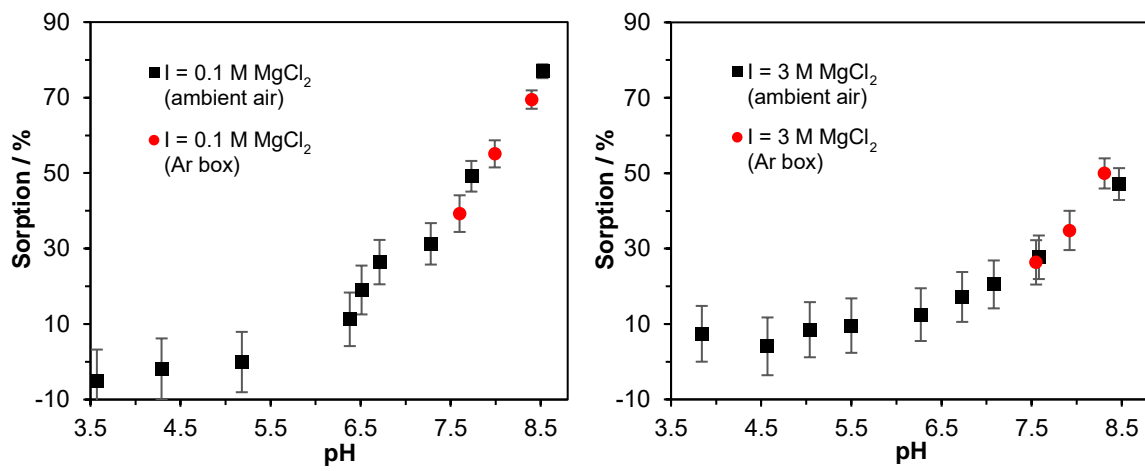


**Figure 2:** Left figure: Sorption of  $8 \times 10^{-6}$  M Np(V) on 20 g/L OPA in  $I = 0.1$  M MgCl<sub>2</sub> solution. Right figure: Sorption of  $8 \times 10^{-6}$  M Np(V) on 20 g/L OPA in  $I = 3.0$  M MgCl<sub>2</sub> solution.

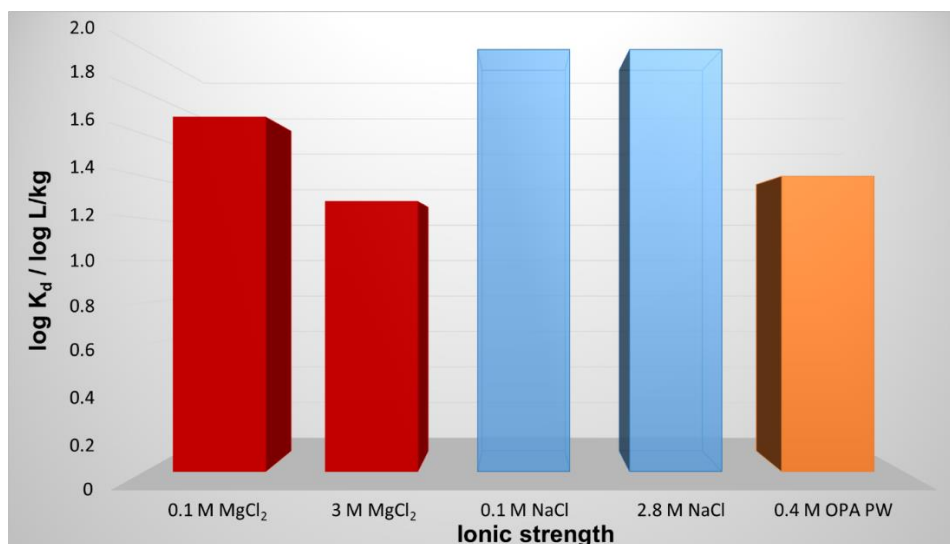


**Figure 3:** Influence of the background electrolyte and its ionic strength on the sorption of  $8 \times 10^{-6}$  M Np(V) on OPA (15 g/l) at pH 7.6 under aerobic conditions.

As mentioned above, one can see the decrease of the Np(V) sorption in high saline MgCl<sub>2</sub> solutions, while the sorption in 0.1 and 2.8 M NaCl solutions is higher and remains constant. For OPA PW as background electrolyte, the sorption values are lying in between. This means they are slightly higher as in 3 M MgCl<sub>2</sub>, but lower than in 0.1 M MgCl<sub>2</sub>. The competitive effect of divalent cations in the background electrolyte on the Np(V) sorption has already been reported in the literature to be much more pronounced than for the monovalent cations [12]. In the case of MgCl<sub>2</sub> as background electrolyte, Mg<sup>2+</sup> blocks strong surface binding sites so that these are not available for the Np uptake. This mechanism is concentration depending and therefore the Np sorption decreases with increasing Mg<sup>2+</sup> concentration. In OPA PW Mg<sup>2+</sup> as well as Ca<sup>2+</sup> ions are present with a combined ionic strength of  $I = 0.12 \text{ M}$  ( $c = 0.04 \text{ M}$ ). This explains the medium sorption value of Np(V) with OPA PW as background electrolyte. However, the surface complexation of Na<sup>+</sup> on OPA is very weak, and thus does not interfere with the Np(V) sorption.

#### *Effect of increased temperatures on the Np(V) sorption*

The sorption experiment at 80 °C shows compared to 25 °C only a slightly increased sorption of Np(V). The averaged log  $K_d$  at 80 °C is with  $2.15 \pm 0.04$  ( $K_d$  in L/kg) close to the log  $K_d$  at room temperature with  $2.00 \pm 0.04$  ( $K_d$  in L/kg). At both temperatures no influence of the NaCl concentration was detectable, so that the average values were calculated from the whole temperature series. These results support the study of Li et al., who found no influence of the temperature on the sorption of Np(V) ( $4 \times 10^{-7} \text{ M}$ ) on Na-bentonite (10 g/L) in 0.1 M NaCl solution in the range between 15 and 80 °C [15].

The mentioned contradiction to studies of Runde et al. [16] and Fröhlich et al. [12], could derive from their complex background electrolytes. Due to the presence of Ca<sup>2+</sup> and Mg<sup>2+</sup>, besides dissolved carbonate in the Yucca mountain on-site well water [16] as well as in OPA PW [12], precipitations of MgCO<sub>3</sub> and CaCO<sub>3</sub>, which have exothermic enthalpies of solution [30], might be responsible for the observed temperature effect in combination with a possible Np(V) coprecipitation or incorporation [31-33].

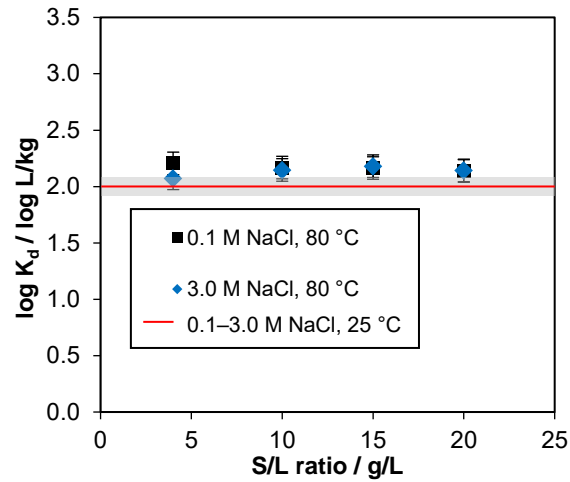


**Figure 4:** The sorption of  $8 \times 10^{-6}$  M Np(V) on OPA in dependency of the S/L ratio (4–20 g/L) in 0.1 and 3.0 M NaCl solution at 80 °C (pH 7.6). The red line represents the average  $\log K_d$  value at 25 °C (0.1–3.0 M NaCl).

## Diffusion experiments

### *Diffusion experiments with HTO and Na<sup>+</sup>*

The obtained diffusion parameters ( $D_e$ ,  $\varepsilon$ , and  $\alpha$ ) for HTO and  $^{22}\text{Na}^+$  of the cells described in Table 2 are presented in Table 3.

**Table 3:** Diffusion parameters ( $D_e$ ,  $\varepsilon$ ) for HTO and ( $D_e$ ,  $\alpha$ , and  $K_d$ ) for  $^{22}\text{Na}^+$  in OPA obtained by through-diffusion experiments at 24 and 60 °C in 1 M and 3 M NaCl, and OPA PW as background electrolyte at pH 7.6 under ambient air.

	HTO		$\alpha$	$^{22}\text{Na}^+$	
	$\varepsilon$	$D_e$ / $10^{-11}$ m <sup>2</sup> /s		$D_e$ / $10^{-11}$ m <sup>2</sup> /s	$K_d$ / L/kg
<b>3 M NaCl, 24 °C</b>	$0.18 \pm 0.01$	$1.6 \pm 0.1$	$0.20 \pm 0.01$	$0.9 \pm 0.1$	$0.01 \pm 0.01$
<b>1 M NaCl, 24 °C</b>	$0.18 \pm 0.01$	$1.9 \pm 0.1$	$0.35 \pm 0.02$	$1.6 \pm 0.1$	$0.10 \pm 0.01$
<b>1 M NaCl, 60 °C</b>	$0.21 \pm 0.01$	$4.1 \pm 0.2$	$0.37 \pm 0.01$	$4.4 \pm 0.1$	$0.07 \pm 0.01$
<b>OPA PW, 60 °C</b>	$0.16 \pm 0.01$	$3.4 \pm 0.2$	$0.42 \pm 0.01$	$3.0 \pm 0.1$	$0.11 \pm 0.01$
<b>OPA PW, 24 °C [34]</b>	$0.15 \pm 0.01$	$1.5 \pm 0.1$	$0.50 \pm 0.02$	$1.8 \pm 0.1$	$0.15 \pm 0.03$

The porosities  $\varepsilon$  of the investigated OPA bore cores (Table 3) agree well with the known values of Mont Terri OPA [5]. No ionic strength effect was observed for the diffusion of HTO in OPA, as it is apparent from the obtained  $D_e$  values for 1 M and 3 M NaCl solutions. In the case of  $^{22}\text{Na}^+$  the  $D_e$  value decreases with increasing salt concentration from  $1.6 \pm 0.1 \times 10^{-11}$  m<sup>2</sup>/s in 1 M NaCl to  $0.9 \pm 0.1 \times 10^{-11}$  m<sup>2</sup>/s in 3 M NaCl solution. This is in agreement with published

data by Glaus et al., who found a decreasing  $D_e$  of  $\text{Na}^+$  with increasing salt concentration in the range between 0.01–1.0 M  $\text{NaClO}_4$  in compacted Na-illite and Na-montmorillonite ( $1900 \text{ kg/m}^3$ ) [35, 36].

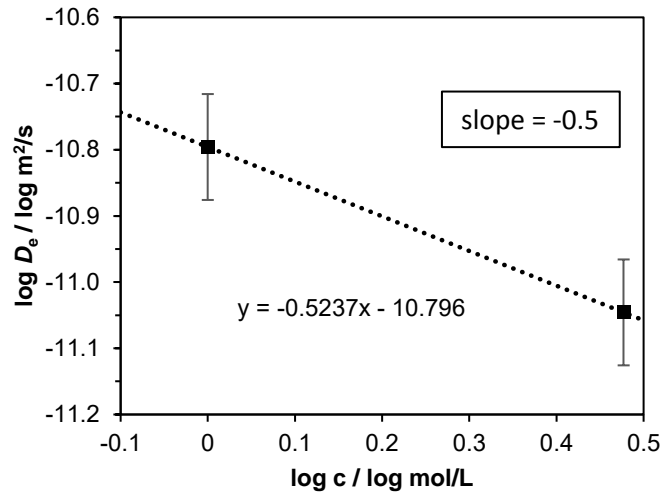


**Figure 5:** Logarithmic presentation of the  $D_e$  of  $\text{Na}^+$  as a function of the NaCl concentration.

The ionic strength effect on the diffusion of cations or anions was explained by the decreased spatial extension of the diffuse double layer (DDL) at the inter-particle surfaces in saline solution, so that only the restrained diffusion at the aqueous phase dominates [36]. This leads to a negative slope for the  $\log D_e$  of  $^{22}\text{Na}^+$  plotted against the logarithmic background electrolyte concentration, as can be seen in Figure 5. Glaus et al. determined a slope of about -0.5 for the diffusion of  $\text{Na}^+$  in compacted Na-illite. This result can be confirmed by our diffusion study, which shows the same dependency. The good agreement between the slope of Na-illite (of Glaus et al.) and OPA (Figure 5) is not surprising, as illite is considered to be the uptake dominating phase in OPA [37].

According to the influence of the temperature on the diffusion described by eq 8, the  $D_e$  values increase with increasing temperature. For HTO and  $^{22}\text{Na}^+$  the  $D_e$  increases in 1 M NaCl solution by a factor of 2.2 and 2.8, respectively between 24 and 60 °C. The values of  $\varepsilon$  and  $\alpha$  remain similar for both radiotracers, as well as the calculated  $K_d$  values of  $^{22}\text{Na}^+$ , within the experimental errors. For OPA PW the obtained  $D_e$  value for HTO and  $^{22}\text{Na}^+$  increase by a factor of 2.3 and 1.6, respectively when rising the temperature from 24 to 60 °C. The determined activation energy for the diffusion of HTO in OPA PW is with  $19 \pm 3 \text{ kJ/mol}$  just below the determined value of Van Loon et al. with  $20 \pm 1 \text{ kJ/mol}$  (for Mont Terri OPA), but also above the value for the diffusion in bulk water with  $18 \text{ kJ/mol}$  [3]. This is in accordance with the assumption of Van Loon et al. of a slightly different structure of the confined water in OPA,



compared to the bulk liquid water. The activation energies for the diffusion of HTO and  $\text{Na}^+$  in OPA PW and 1 M NaCl are given in Table 6 together with the results for Np(V) in this regard.

### *Diffusion experiments with Np*

#### *Influence of salinity*

After the complete out-diffusion of HTO and  $^{22}\text{Na}^+$ , in-diffusion experiments with  $8 \mu\text{M}$  Np(V) were started. To assess the reliability of the diffusion technique and the determination of the diffusion parameters of Np in intact OPA, in-diffusion experiments with  $^{22}\text{Na}^+$  were also performed. Compared to the results obtained by the through-diffusion studies, the derived diffusion parameters are in good agreement, indicating stable conditions of the bore cores during the experiment (Table 3 and Table 7 in the SI).

Np was given a period of 63 and 67 d to diffuse into the clay for cells 1 and 2, respectively. About 50 thin layers from the primary side of the clay were removed by the abrasive peeling method. The  $^{237}\text{Np}$  and  $^{22}\text{Na}^+$  activities in each layer were measured via  $\gamma$ -ray spectroscopy.

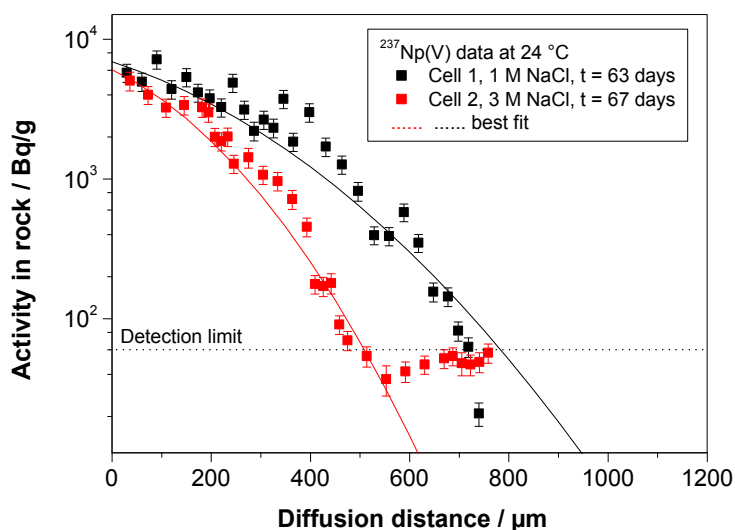


**Figure 6:** Diffusion profiles of  $8 \times 10^{-6} \text{ M}$   $^{237}\text{Np}(\text{V})$  in OPA of cells 1 and 2 in NaCl solutions (1 M and 3 M) at pH 7.6 under ambient air at  $24 \text{ }^\circ\text{C}$  together with the fit curves.

Figure 6 shows the diffusion profiles of Np(V) in OPA of cells 1 and 2 in 1 M and 3 M NaCl solutions at pH 7.6 under ambient air at  $24 \text{ }^\circ\text{C}$  together with the fit curves. The obtained diffusion profiles were evaluated using the equations given in [34], which are based on the model of Yaroshchuk et al., including a correction for the retardation effect of Np by the stainless steel filters [38].

The penetration depth of Np in 1 M NaCl solution was  $740 \mu\text{m}$  and thus significantly further than in 3 M NaCl solution with  $550 \mu\text{m}$ . Despite the decrease of the penetration depth, no

differences in either shape of the curves or quality of the fit were observed. The  $D_e$  and  $\alpha$  fitting results are summarized with the  $\log K_d$  in Table 4. As expected from the shown related batch experiments, the  $\log K_d$  values for both cells are in good agreement within the errors.

**Table 4:** Diffusion parameters ( $D_e$ ,  $\alpha$ ) and  $K_d$  for  $^{237}\text{Np}$  in OPA determined by in-diffusion experiments of cells 1 and 2 in 1 and 3 M NaCl solutions at pH 7.6 under ambient air at 24 °C.

	$\alpha$	$D_e$ / $10^{-12} \text{ m}^2/\text{s}$	$\log K_d$ ( $K_d$ in L/kg)
<b>1 M NaCl</b>	$742 \pm 9$	$6.9 \pm 1.2$	$2.5 \pm 0.1$
<b>3 M NaCl</b>	$455 \pm 7$	$2.4 \pm 1.0$	$2.3 \pm 0.1$

As can be seen in Table 4, the  $D_e$  values of Np(V) decrease from  $6.9 \pm 1.2 \times 10^{-12}$  to  $2.4 \pm 1.0 \times 10^{-12} \text{ m}^2/\text{s}$  with increasing ionic strength from 1 to 3 M NaCl. The reason of this ionic strength effect is probably the same as in the case of  $\text{Na}^+$ . The slope of the linear relation of the  $\log D_e$  and the log of the concentration of the electrolyte yields -1, which is compared to  $\text{Na}^+$  by a factor of 2 lower. This corresponds to the valency of the specific cation, as described by Glaus et al., who also found a factor of 2 difference between the slopes of the mentioned presentations for  $\text{Na}^+$  and  $\text{Sr}^{2+}$ . As Np(V) has as  $\text{NpO}_2^+$  an effective charge of +2.35 [20], the line in Figure 7 yields a similar value as found by Glaus et al. for  $\text{Sr}^{2+}$ . Therefore, the dependency on the effective charge of the diffusing cation can be confirmed.

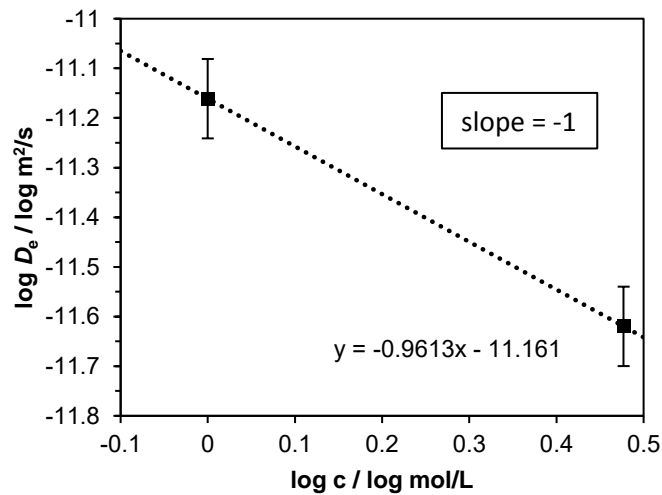


**Figure 7:** Logarithmic presentation of the  $D_e$  of  $\text{NpO}_2^+$  as a function of the NaCl concentration.

### Influence of temperature

The diffusion profiles of Np(V) in OPA at room temperature and at 60 °C are shown in Figure 8 for 1 M NaCl solution and in Figure 9 for OPA PW as background electrolyte together with the best fit curves.

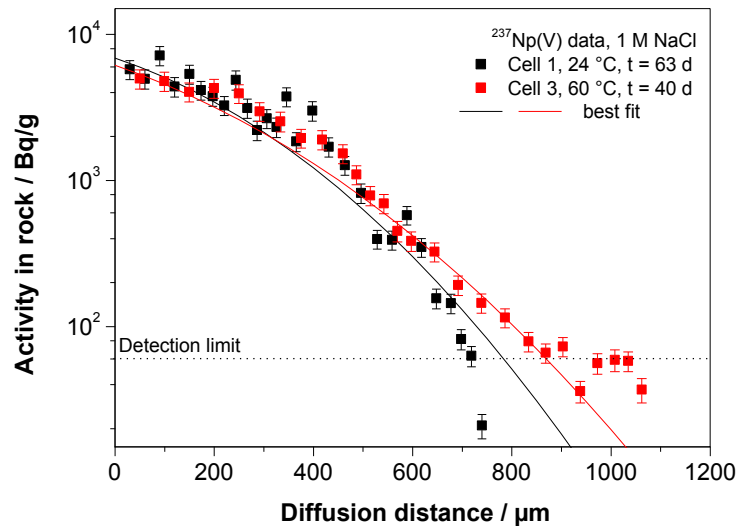


**Figure 8:** Diffusion profiles of  $8 \times 10^{-6}$  M  $^{237}\text{Np(V)}$  in OPA (cells 1 and 3) at 24 and 60 °C in 1 M NaCl at pH 7.6 under aerobic conditions together with the fit curves.

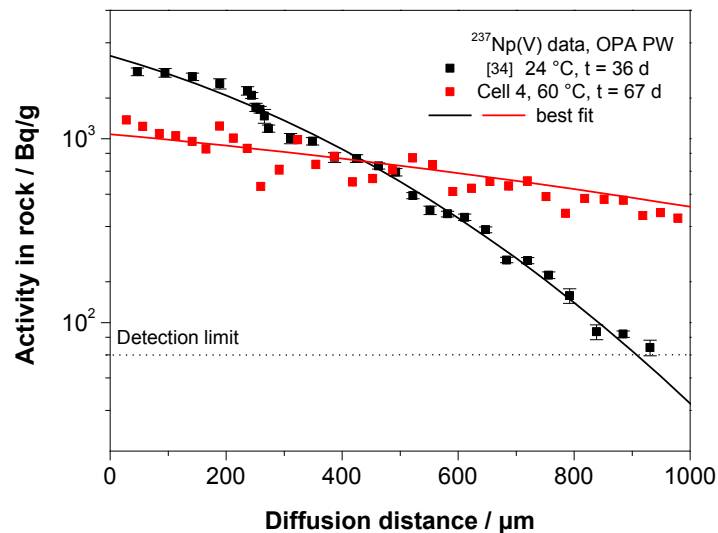


**Figure 9:** Diffusion profiles of  $8 \times 10^{-6}$  M  $^{237}\text{Np(V)}$  in OPA at 24 °C [34] and 60 °C in OPA PW at pH 7.6 (cell 4) under aerobic conditions together with the fit curves.

Despite the shorter runtime of cell 3 at 60 °C in Figure 8 the Np penetration depth exceeds that of cell 1 at 24 °C. This corresponds to an increased  $D_e$  by a factor of 2–3, which can also be

seen in Table 5 together with the other fit parameters. The same increase of  $D_e$  is visible in Figure 9 for cell 4 using OPA PW compared to the results of Wu et al. at 24 °C [34].

Besides the strong influence of the temperature on the effective diffusion, there is no influence of the temperature on the Np(V) sorption visible. The difference of the Np activity between the cells with OPA PW in Figure 9 must be attributed to the OPA heterogeneity, as the Np concentration in the primary reservoir was similar. The  $K_d$  value in Table 5 for the diffusion at 24 °C is compared to 60 °C consequential slightly increased. However, the comparable batch experiment of Wu et al. is in good agreement with the  $K_d$  of cell 4 [34] and verifies the results. Based on both the temperature depending diffusion and batch experiments it can be stated, that the Np(V) sorption on OPA was not affected by an increased temperature.

The higher Np activity at the interface of the diffusion experiments in 1 M NaCl solution compared with that of OPA PW is in line with the results shown in section 0 for the related sorption experiments and can be explained by the influence of divalent cations.

Overall, the  $K_d$  determined by diffusion experiments seems to be higher than by batch experiments. This is not really surprising, as Np(V) can be partially reduced in OPA to Np(IV), which is far less mobile [39]. As mentioned in section 0, OPA contains redox active Fe(II) minerals and the redox potential inside the bores is probably more reducing, than in the suspensions of the batch experiments using OPA powder, which was grinded under ambient air conditions. Furthermore, the Np(V) concentration of  $8 \times 10^{-6}$  M commonly used in the batch experiments is according to Figure 1 in the non-ideal sorption range. A decreasing Np(V) concentration as occurring in the diffusion profiles can lead in this way to increasing  $K_d$  values.

**Table 5:** Diffusion parameters ( $D_e$ ,  $\alpha$ , and  $K_d$ ) for  $^{237}\text{Np}$  in OPA obtained by in-diffusion experiments at 60 °C and 24 °C in 1 M NaCl and OPA PW at pH 7.6 under ambient air, compared to other results [34].

	<b>T / °C</b>	<b><math>\alpha</math></b>	<b><math>D_e</math> / <math>10^{-12} \text{ m}^2/\text{s}</math></b>	<b>log <math>K_d</math> / L/kg</b>
<b>Cell 3, 1 M NaCl</b>	60	$834 \pm 8$	$17.5 \pm 1.8$	$2.5 \pm 0.1$ ( $2.2 \pm 0.1$ at 80 °C)
<b>Cell 1, 1 M NaCl</b>	24	$742 \pm 9$	$6.9 \pm 1.2$	$2.5 \pm 0.1$ ( $2.0 \pm 0.1$ )
<b>Cell 4, OPA PW</b>	60	$66 \pm 2$	$15.0 \pm 1.6$	$1.5 \pm 0.1$
<b>OPA PW [34]</b>	24	$243 \pm 4$	$6.9 \pm 1.1$	$2.0 \pm 0.1$ ( $1.4 \pm 0.1$ ) [34]

values in brackets are from the related batch experiments

The activation energies  $E_a$  for the diffusion of  $\text{NpO}_2^+$  in OPA were calculated for both electrolytes and are shown in Table 6, together with the results from section 0 and results from literature [3, 40]. The  $E_a$  for the diffusion of  $\text{NpO}_2^+$  in OPA resulted in  $21.3 \pm 2.4$  kJ/mol for 1 M NaCl and  $17.7 \pm 2.0$  kJ/mol for OPA PW. These values are in the same range as those determined for HTO and  $^{22}\text{Na}^+$  in section 0 and do also match those from literature [3, 40]. According to similar findings for cations and anions, Van Loon et al. proposed to use an  $E_a$  of  $20 \pm 1$  kJ/mol for all radionuclides. These overall similar values for  $E_a$  indicate that no qualitative interpretation can be given with respect to the different diffusion mechanisms of these ions in OPA. However, the derived activation energies in this work were calculated from two point Arrhenius plots resulting in larger uncertainties. This might concern in particular the  $E_a$  value of  $^{22}\text{Na}^+$  in OPA PW, which is with  $11.7 \pm 2.0$  kJ/mol compared to  $21.0 \pm 1.6$  in [3] unexpectedly low.

**Table 6:** Activation energies  $E_a$  for the diffusion of HTO,  $^{22}\text{Na}^+$ ,  $^{237}\text{Np}$  in OPA using 1 M NaCl and OPA PW as background electrolyte determined from through-diffusion experiments.

	Medium	$E_a$ / kJ/mol	Lit. / kJ/mol
<b>HTO</b>	1 M NaCl	$17.6 \pm 2.3$	-
	OPA PW	$18.7 \pm 2.8$	$20.0 \pm 1.0$ [3]
<b><math>\text{Na}^+</math></b>	1 M NaCl	$23.1 \pm 2.0$	-
	OPA PW	$11.7 \pm 2.0$	$21.0 \pm 1.6$ [3]
<b><math>\text{NpO}_2^+</math></b>	1 M NaCl	$21.3 \pm 2.4$	-
	OPA PW	$17.7 \pm 2.0$	-
<b><math>\text{Cl}^-</math></b>	OPA PW	-	$19.4 \pm 1.5$ [40]

### Conclusions

Batch experiments with Np(V) on OPA in NaCl solutions of pH 7.6 showed neither an influence of the background electrolyte concentration in the range of 0.1 to 3.0 M, nor a temperature dependence between 24 and 80 °C over a wide range of Np(V) and OPA concentrations. However, changing the background electrolyte to  $\text{MgCl}_2$  resulted in a significant decrease of the Np(V) sorption on OPA between pH 3.5–8.5. This effect was more pronounced with increasing  $\text{MgCl}_2$  concentration.

Diffusion experiments in NaCl solutions as mobile phase showed a decrease in  $D_e$  for  $\text{Na}^+$  and  $\text{NpO}_2^+$  with increasing ionic strength, which can be explained by a reduced DDL diffusion as suggested by Glaus et al. [36]. In accordance with our batch experiments, no temperature dependency of the Np sorption was found in diffusion experiments, as no changes in the  $K_d$  values were observed. The temperature dependency of the  $D_e$  of HTO,  $^{22}\text{Na}^+$ , and  $\text{NpO}_2^+$  showed an Arrhenius behavior. The derived activation energies  $E_a$  for the Np diffusion in OPA

in 1 M NaCl and OPA PW accounted for  $21.3 \pm 2.4$  kJ/mol and  $17.7 \pm 2.0$  kJ/mol, respectively, and are similar to the values of other ions in the literature [3, 40].

### **Acknowledgment**

We thank the Karlsruhe Institute of Technology – Institute for Nuclear Waste Disposal (KIT-INE) for providing the OPA powders and bore cores.

### **References**

1. Fröhlich, D.R., *Sorption of neptunium on clays and clay minerals - a review*. Clays and Clay Minerals, 2015. **63**(3-4): p. 262-276.
2. Gompper, K., *Zur Abtrennung langlebiger Radionuklide*. Radioaktivität und Kernenergie. 2001, Karlsruhe: Forschungszentrum Karlsruhe.
3. Van Loon, L.R. and J.M. Soler, *Diffusion of HTO,  $^{36}\text{Cl}$ ,  $^{125}\text{I}$  and  $^{22}\text{Na}^+$  in Opalinus Clay: Effect of confining pressure, sample orientation, sample depth and temperature*. PSI Bericht Nr. 04-03, 2004.
4. Neck, V. and J.I. Kim, *Solubility and hydrolysis of tetravalent actinides*. Radiochimica Acta, 2001. **89**(1): p. 1-16.
5. Nagra, *Projekt Opalinuston - Synthese der geowissenschaftlichen Untersuchungsergebnisse*. Technical Report 02-03, 2002, Wettingen, Switzerland: Nagra.
6. Lieser, K.H. and U. Muhlenweg, *Neptunium in the Hydrosphere and in the Geosphere .1. Chemistry of Neptunium in the Hydrosphere and Sorption of Neptunium from Groundwaters on Sediments under Aerobic and Anaerobic Conditions*. Radiochimica Acta, 1988. **43**(1): p. 27-35.
7. F. J. Pearson, D.A., A. Bath, J.-Y. Boisson, A. M. Fernández, H.-E. Gäbler, E. Gaucher, A. Gautschi, L. Griffault, P. Hernán, H. N. Waber, *Mont Terri Project – geochemistry of water in the Opalinus Clay formation at the Mont Terri Rock Laboratory*. Reports of the Federal Office for Water and Geology (FOWG), Geology Series 2003(No. 5.).
8. Brauer, V. and P. Hoth, *Argillaceous rock as host rock for final storage of radioactive waste in Germany*. Atw-International Journal for Nuclear Power, 2007. **52**(5): p. 325.
9. Brewitz, W., *Eignungsprüfung der Schachtanlage Konrad für die Endlagerung radioaktiver Abfälle: Abschlussbericht (GSF - T 136)*. 1982: GSF.
10. Pearson, F.J., *Opalinus Clay experimental water: A1 type*. PSI technical report TM-44-98-07, 1998, Villigen, Switzerland: Paul Scherrer Institut.

11. Nagasaki, S., T. Saito, and T.T. Yang, *Sorption behavior of Np(V) on illite, shale and MX-80 in high ionic strength solutions*. Journal of Radioanalytical and Nuclear Chemistry, 2016. **308**(1): p. 143-153.
12. Fröhlich, D.R., S. Amayri, J. Drebert, and T. Reich, *Influence of temperature and background electrolyte on the sorption of neptunium(V) on Opalinus Clay*. Applied Clay Science, 2012. **69**: p. 43-49.
13. Mironenko, M.V., D.A. Malikov, Y.M. Kulyako, and B.F. Myasoedov, *Sorption of Np(V) on montmorillonite from solutions of MgCl<sub>2</sub> and CaCl<sub>2</sub>*. Radiochemistry, 2006. **48**(1): p. 69-74.
14. Brassler, T., J. Droste, I. Müller-Lyda, J. Neles, M. Sailer, G. Schmidt, and M. Steinhoff, *Endlagerung wärmeentwickelnder radioaktiver Abfälle in Deutschland*. GRS-247,, 2008.
15. Li, P., Z. Liu, F. Ma, Q. Shi, Z. Guo, and W. Wu, *Effects of pH, ionic strength and humic acid on the sorption of neptunium(V) to Na-bentonite*. Journal of Molecular Liquids, 2015. **206**: p. 285-292.
16. Runde, W., S.D. Conradson, D.W. Efurud, N.P. Lu, C.E. VanPelt, and C.D. Tait, *Solubility and sorption of redox-sensitive radionuclides (Np, Pu) in J-13 water from the Yucca Mountain site: comparison between experiment and theory*. Applied Geochemistry, 2002. **17**(6): p. 837-853.
17. Wu, T., S. Amayri, J. Drebert, L.R. Van Loon, and T. Reich, *Neptunium(V) sorption and diffusion in Opalinus Clay*. Environmental Science & Technology, 2009. **43**(17): p. 6567-6571.
18. Joseph, C., L.R. Van Loon, A. Jakob, R. Steudtner, K. Schmeide, S. Sachs, and G. Bernhard, *Diffusion of U(VI) in Opalinus Clay: Influence of temperature and humic acid*. Geochimica et Cosmochimica Acta, 2013. **109**: p. 74-89.
19. Joseph, C., K. Schmeide, S. Sachs, V. Brendler, G. Geipel, and G. Bernhard, *Sorption of uranium(VI) onto Opalinus Clay in the absence and presence of humic acid in Opalinus Clay pore water*. Chemical Geology, 2011. **284**(3-4): p. 240-250.
20. Mauerhofer, E., K. Zhernosekov, and F. Rosch, *Limiting transport properties and hydration numbers of actinyl ions in pure water*. Radiochimica Acta, 2004. **92**(1): p. 5-10.
21. Fröhlich, D.R., S. Amayri, J. Drebert, and T. Reich, *Sorption of neptunium(V) on Opalinus Clay under aerobic/anaerobic conditions*. Radiochimica Acta, 2011. **99**(2): p. 71-77.
22. Amayri, S., A. Jermolajev, and T. Reich, *Neptunium(V) sorption on kaolinite*. Radiochimica Acta, 2011. **99**(6): p. 349-357.

23. Gustafsson, J.P., *Visual MINTEQ v 3.0*. 2004, Stockholm, Sweden: Swedish Royal Institute of Technology (KTH).
24. Fanghänel, T., V. Neck, and J.I. Kim, *The ion product of H<sub>2</sub>O, dissociation constants of H<sub>2</sub>CO<sub>3</sub> and Pitzer parameters in the system Na<sup>+</sup>/H<sup>+</sup>/OH<sup>-</sup>/HCO<sub>3</sub><sup>-</sup>/CO<sub>3</sub><sup>2-</sup>/ClO<sub>4</sub><sup>-</sup>/H<sub>2</sub>O at 25°C*. Journal of Solution Chemistry, 1996. **25**(4): p. 327-343.
25. Van Loon, L.R., J.M. Soler, and M.H. Bradbury, *Diffusion of HTO, <sup>36</sup>Cl<sup>-</sup> and <sup>125</sup>I<sup>-</sup> in Opalinus Clay samples from Mont Terri: Effect of confining pressure*. Journal of Contaminant Hydrology, 2003. **61**(1-4): p. 73-83.
26. Van Loon, L.R. and J. Eikenberg, *A high-resolution abrasive method for determining diffusion profiles of sorbing radionuclides in dense argillaceous rocks*. Applied Radiation and Isotopes, 2005. **63**(1): p. 11-21.
27. Van Loon, L.R., J.M. Soler, A. Jakob, and M.H. Bradbury, *Effect of confining pressure on the diffusion of HTO, <sup>36</sup>Cl<sup>-</sup> and <sup>125</sup>I<sup>-</sup> in a layered argillaceous rock (Opalinus Clay): diffusion perpendicular to the fabric*. Applied Geochemistry, 2003. **18**: p. 1653-1662.
28. Eisenberg, D., Kauzmann, W., *The structure and properties of water*. Oxford University Press, Ely house. 1969, London.
29. Freundlich, H. Kapillarchemie. 1909, Leipzig, Germany: Akademische Verlagsgesellschaft.
30. Plummer, L.N. and E. Busenberg, *The solubilities of calcite, aragonite and vaterite in CO<sub>2</sub>-H<sub>2</sub>O solutions between 0 and 90 °C, and an evaluation of the aqueous model for the system CaCO<sub>3</sub>-CO<sub>2</sub>-H<sub>2</sub>O*. Geochimica et Cosmochimica Acta, 1982. **46**(6): p. 1011-1040.
31. Walker, S.M. and U. Becker, *Uranyl (VI) and neptunyl (V) incorporation in carbonate and sulfate minerals: Insight from first-principles*. Geochimica et Cosmochimica Acta, 2015. **161**: p. 19-35.
32. Balboni, E., J.M. Morrison, Z.M. Wang, M.H. Engelhard, and P.C. Burns, *Incorporation of Np(V) and U(VI) in carbonate and sulfate minerals crystallized from aqueous solution*. Geochimica et Cosmochimica Acta, 2015. **151**: p. 133-149.
33. Heberling, F., M.A. Denecke, and D. Bosbach, *Neptunium(V) coprecipitation with calcite*. Environmental Science & Technology, 2008. **42**(2): p. 471-476.
34. Wu, T., S. Amayri, J. Drebert, L.R. Van Loon, and T. Reich, *Neptunium(V) sorption and diffusion in Opalinus Clay*. Environmental Science & Technology, 2009. **43**: p. 6567-6571.
35. Glaus, M.A., B. Baeyens, M.H. Bradbury, A. Jakob, L.R. Van Loon, and A. Yaroshchuk, *Diffusion of <sup>22</sup>Na and <sup>85</sup>Sr in Montmorillonite: Evidence of interlayer diffusion being*



*the dominant pathway at high compaction.* Environmental Science & Technology, 2007. **41**: p. 478-485.

36. Glaus, M.A., S. Frick, R. Rossé, and L.R.V. Loon, *Comparative study of tracer diffusion of HTO,  $^{22}\text{Na}^+$  and  $^{36}\text{Cl}^-$  in compacted kaolinite, illite and montmorillonite.* Geochimica et Cosmochimica Acta, 2010. **74**(7): p. 1999-2010.
37. Bradbury, M.H. and B. Baeyens, *Predictive sorption modelling of Ni(II), Co(II), Eu(III), Th(IV) and U(VI) on MX-80 bentonite and Opalinus Clay: A "bottom-up" approach.* Applied Clay Science, 2011. **52**(1-2): p. 27-33.
38. Yaroshchuk, A.E. and L.R. Van Loon, *Improved interpretation of in-diffusion measurements with confined swelling clays.* Journal of Contaminant Hydrology, 2008. **97**(1-2): p. 67-74.
39. Fröhlich, D.R., S. Amayri, J. Drebert, D. Grolimund, J. Huth, U. Kaplan, J. Krause, and T. Reich, *Speciation of Np(V) uptake by Opalinus Clay using synchrotron microbeam techniques.* Analytical and Bioanalytical Chemistry, 2012. **404**(8): p. 2151-62.
40. Van Loon, L.R., W. Müller, and K. Iijima, *Activation energies of the self-diffusion of HTO,  $^{22}\text{Na}^+$  and  $^{36}\text{Cl}^-$  in a highly compacted argillaceous rock (Opalinus Clay).* Applied Geochemistry, 2005. **20**(5): p. 961-972.

### **List of Figures**

- Figure 1:  $\log K_d$  for the sorption of Np(V) on OPA (15 g/L OPA) as a functions of the total Np(V) concentration  $C_{\text{tot}}$  at pH 7.6 under aerobic conditions for 0.1–2.8 M NaCl solutions..... i
- Figure 2: Left figure: Sorption of  $8 \times 10^{-6}$  M Np(V) on 20 g/L OPA in I = 0.1 M  $\text{MgCl}_2$  solution. Right figure: Sorption of  $8 \times 10^{-6}$  M Np(V) on 20 g/L OPA in I = 3.0 M  $\text{MgCl}_2$  solution. .... j
- Figure 3: Influence of the background electrolyte and its ionic strength on the sorption of  $8 \times 10^{-6}$  M Np(V) on OPA (15 g/l) at pH 7.6 under aerobic conditions..... j
- Figure 4: The sorption of  $8 \times 10^{-6}$  M Np(V) on OPA in dependency of the S/L ratio (4–20 g/L) in 0.1 and 3.0 M NaCl solution at 80 °C (pH 7.6). The red line represents the average  $\log K_d$  value at 25 °C (0.1–3.0 M NaCl). .... l
- Figure 5: Logarithmic presentation of the  $D_e$  of  $\text{Na}^+$  as a function of the NaCl concentration. .... m
- Figure 6: Diffusion profiles of  $8 \times 10^{-6}$  M  $^{237}\text{Np(V)}$  in OPA of cells 1 and 2 in NaCl solutions (1 M and 3 M) at pH 7.6 under ambient air at 24 °C together with the fit curves. .... n
- Figure 7: Logarithmic presentation of the  $D_e$  of  $\text{NpO}_2^+$  as a function of the NaCl concentration..... o
- Figure 8: Diffusion profiles of  $8 \times 10^{-6}$  M  $^{237}\text{Np(V)}$  in OPA (cells 1 and 3) at 24 and 60 °C in 1 M NaCl at pH 7.6 under aerobic conditions together with the fit curves. .... p

Figure 9: Diffusion profiles of  $8 \times 10^{-6} \text{ M } ^{237}\text{Np(V)}$  in OPA at 24 °C [34] and 60 °C in OPA PW at pH 7.6 (cell 4) under aerobic conditions together with the fit curves. .... p

### List of Tables

Table 1: Composition of synthetic OPA pore water [10]. .... d

Table 2: Experimental details of the prepared diffusion cells under ambient air at pH 7.6. .... h

Table 3: Diffusion parameters ( $D_e$ ,  $\epsilon$ ) for HTO and ( $D_e$ ,  $\alpha$ , and  $K_d$ ) for  $^{22}\text{Na}^+$  in OPA obtained by through-diffusion experiments at 24 and 60 °C in 1 M and 3 M NaCl, and OPA PW as background electrolyte at pH 7.6 under ambient air. .... l

Table 4: Diffusion parameters ( $D_e$ ,  $\alpha$ ) and  $K_d$  for  $^{237}\text{Np}$  in OPA determined by in-diffusion experiments of cells 1 and 2 in 1 and 3 M NaCl solutions at pH 7.6 under ambient air at 24 °C. .... o

Table 5: Diffusion parameters ( $D_e$ ,  $\alpha$ , and  $K_d$ ) for  $^{237}\text{Np}$  in OPA obtained by in-diffusion experiments at 60 °C and 24 °C in 1 M NaCl and OPA PW at pH 7.6 under ambient air, compared to other results [34]. .... q

Table 6: Activation energies  $E_a$  for the diffusion of HTO,  $^{22}\text{Na}^+$ ,  $^{237}\text{Np}$  in OPA using 1 M NaCl and OPA PW as background electrolyte determined from through-diffusion experiments. .... r

Table 7: Diffusion parameters ( $D_e$ ,  $\alpha$ , and  $K_d$ ) for  $^{22}\text{Na}$  in OPA determined by in-diffusion experiments. .... w

### Supplementary Information

**Table 7:** Diffusion parameters ( $D_e$ ,  $\alpha$ , and  $K_d$ ) for  $^{22}\text{Na}$  in OPA determined by in-diffusion experiments.

Cell	conditions	$\alpha$	$D_e$ / $10^{-11} \text{ m}^2/\text{s}$	$K_d$ / L/kg
1	1 M NaCl, 24 °C	$0.46 \pm 0.01$	$1.6 \pm 0.1$	$0.12 \pm 0.01$
2	3 M NaCl, 24°C	$0.19 \pm 0.002$	$1.0 \pm 0.1$	-
3	1 M NaCl, 60 °C	$0.43 \pm 0.004$	$1.8 \pm 0.2$	$0.10 \pm 0.01$
4	OPA PW, 60 °C	$0.39 \pm 0.004$	$3.1 \pm 0.3$	$0.09 \pm 0.07$





## **Speciation of neptunium during sorption and diffusion in natural clay**

### **Statement about the contribution to the manuscript of the authors named:**

The main author and participant in all X-ray absorption and fluorescence measurements was Prof. Dr. T. Reich. The person responsible for the sorption sample experiments and investigations was Dr. D. R. Fröhlich, as was P. J. B. Börner for the diffusion experiments and the related investigations with respect to the diffusion profiles calculation and the related XANES spectra analysis. The samples were prepared under guidance of J. Drebert. All synchrotron measurements were performed under assistance of Dr. D. Grolimund, the local contact and group leader of the microXAS beamline at the SLS (Villigen, PSI, Switzerland), and assisted by Dr. S. Amayri and Dr. U. Kaplan.

# Speciation of neptunium during sorption and diffusion in natural clay

T Reich<sup>1,3</sup>, S Amayri<sup>1</sup>, P J B Börner<sup>1</sup>, J Drebert<sup>1</sup>, D R Fröhlich<sup>1,4</sup>, D Grolimund<sup>2</sup> and U Kaplan<sup>1,5</sup>

<sup>1</sup> Institute of Nuclear Chemistry, Johannes Gutenberg University Mainz, 55099 Mainz, Germany

<sup>2</sup> Swiss Light Source, Paul Scherrer Institute, 5232 Villigen PSI, Switzerland

E-mail: tobias.reich@uni-mainz.de

**Abstract.** In argillaceous rocks, which are considered as a potential host rock for nuclear waste repositories, sorption and diffusion processes govern the migration behaviour of actinides like neptunium. For the safety analysis of such a repository, a molecular-level understanding of the transport and retardation phenomena of radioactive contaminants in the host rock is mandatory. The speciation of Np during sorption and diffusion in Opalinus Clay was studied at near neutral pH using a combination of spatially resolved synchrotron radiation techniques. During the sorption and diffusion experiments, the interaction of 8  $\mu\text{M}$  Np(V) solutions with the clay lead to the formation of spots at the clay-water interface with increased Np concentrations as determined by  $\mu\text{-XRF}$ . Several of these spots are correlated with areas of increased Fe concentration. Np L<sub>3</sub>-edge  $\mu\text{-XANES}$  spectra revealed that up to 85% of the initial Np(V) was reduced to Np(IV). Pyrite could be identified by  $\mu\text{-XRD}$  as a redox-active mineral phase responsible for the formation of Np(IV). The analysis of the diffusion profile within the clay matrix after an in-diffusion experiment for two months showed that Np(V) is progressively reduced with diffusion distance, i.e. Np(IV) amounted to  $\approx 12\%$  and  $\approx 26\%$  at 30  $\mu\text{m}$  and 525  $\mu\text{m}$ , respectively.

## 1. Introduction

Argillaceous rock formations are under consideration as a potential host rock for the construction of high-level nuclear waste repositories. Np(IV) and Np(V) are the most stable oxidation states of  $^{237}\text{Np}$  ( $t_{1/2} = 2.1 \times 10^6$  a) under environmental conditions. We have investigated the sorption and diffusion of the more mobile Np(V) in Opalinus Clay (OPA), a natural clay from the Mont Terri rock laboratory in Switzerland [1-3]. OPA, which is present also in Southern Germany, possesses a micro-scale heterogeneity and is composed of several types of clay minerals, but also of calcite, quartz and Fe(II)-bearing minerals. In our previous diffusion [1] and anaerobic sorption experiments [2], we observed higher distribution coefficients,  $K_d$ , than expected from batch experiments performed in air, suggesting that a partial reduction of Np(V) to Np(IV) had occurred. To verify this hypothesis, different sorption

---

<sup>3</sup> Author to whom any correspondence should be addressed.

<sup>4</sup> Present address: Institute of Physical Chemistry, Universität Heidelberg, 69120 Heidelberg, Germany

<sup>5</sup> Present address: Institute for Nuclear Waste Disposal, Karlsruher Institut für Technologie, 67021 Karlsruhe, Germany

and diffusion samples with Np(V) were prepared at near neutral pH for spatially resolved, molecular-level investigations at the microXAS beamline of the Swiss Light Source (SLS).

## 2. Experimental

The sorption sample was prepared by contacting a 20-30  $\mu\text{m}$  thick thin section of OPA with 8  $\mu\text{M}$   $^{237}\text{Np(V)}$  solution (Millipore water,  $\text{pH} \approx 7$ ) under anaerobic conditions in an argon glove box. After a contact time of five days, the aqueous phase was removed [4].

For the preparation of the diffusion sample, an intact OPA cylinder (diameter 25.4 mm, thickness 11 mm) was mounted into a diffusion cell as described in [1]. The clay cylinder was oriented so that the bedding was parallel to the direction of transport (diffusion). The high-concentration reservoir of the diffusion setup contained 8  $\mu\text{M}$   $^{237}\text{Np(V)}$  solution (artificial OPA pore water,  $\text{pH} = 7.6$  [5]). The low-concentration reservoir contained only artificial OPA pore water without Np. The diffusion experiment was performed at 25 °C under ambient-air conditions and lasted for 61 days. During this time the  $E_h$  in the high-concentration reservoir was approximately equal to 480 mV (SHE). After two months, the diffusion cell was opened and the clay cylinder was cleaved parallel to the bedding. Smaller segments of the clay cylinder were mounted into the sample holder.

Both samples were measured at the microXAS beamline at the SLS using the Kirkpatrick-Baez mirror microfocusing system and the Si(111) double-crystal monochromator. X-ray fluorescence maps of several elements including Si, S, K, Ca, Ti, Fe, Sr and Np were recorded using a single-element Si detector (KETEK GmbH, Germany). The excitation energy was 17.62 or 17.70 keV, which is above the Np  $L_3$ -edge. The size of the focused X-ray beam was approximately  $2 \times 4 \mu\text{m}$  (height  $\times$  width). X-ray diffraction patterns of the OPA thin section on high-purity quartz glass (Heraeus Holding GmbH, Germany) were recorded with a 100k Pilatus detector (DECTRIS Ltd., Switzerland). Np  $L_3$ -edge XANES spectra were recorded in fluorescence mode at spots where  $\mu$ -XRF maps had shown areas with higher Np concentrations. A Zr foil ( $E_0 = 17.998 \text{ keV}$ ) was used for energy calibration.  $\mu$ -XRD mappings ( $20 \times 20 \mu\text{m}$ , 1  $\mu\text{m}$  step size) were collected for the sorption sample (thin section) at 17.70 keV. The angle between the incoming X-ray beam and the fluorescence detector was 45° or 20° (by simultaneous use of XRD detector) for the sorption sample and equal to 30° for the diffusion sample, respectively. The analysis of the  $\mu$ -XRF,  $\mu$ -XANES and  $\mu$ -XRD data using several software packages is described in [4].

## 3. Results and discussion

### 3.1. Sorption sample

The  $\mu$ -XRF mappings of elements contained in OPA (e.g. Si, S, K, Ca, Fe) reflect the mineralogical heterogeneity of the natural clay. For example, the  $2 \times 2 \text{ mm}$   $\mu$ -XRF map of Fe in figure 1 (a) shows a large area of increased Fe concentration. As can be seen from the corresponding Np XRF map in figure 1 (a), several spots of increased Np concentration are clearly correlated with the Fe concentration. In the region marked with a white cross (figure 1 (a)), the measured Np  $L_3$ -edge XANES spectrum is composed of  $85 \pm 5\%$  Np(IV) and  $15 \pm 5\%$  Np(V) (figure 1 (b)), indicating that the initial Np(V) has been significantly reduced to Np(IV).  $\mu$ -XRD measurements in this area (figure 1 (c)) showed that Np was accumulated on pyrite ( $\text{FeS}_2$ ). Therefore, pyrite is at least one of the redox-active mineral phases of OPA responsible for the reduction of Np(V). It should be noted that Np spots with considerable fractions of tetravalent Np could be found also in other OPA sorption samples, even when the experiments were performed under ambient-air conditions [4].

### 3.2. Diffusion sample

In the long-term diffusion experiment using 8  $\mu\text{M}$  Np(V) in OPA pore water ( $\text{pH} 7.6$ ), we were able to derive the Np diffusion profile along a 3 mm long diffusion path parallel to the bedding of the clay using  $\mu$ -XRF maps. As can be seen from figure 2 (a), the amount of Np decreases steadily with diffusion distance and reaches the background level after approximately 2.5 mm. Several Np  $L_3$ -edge  $\mu$ -XANES

spectra were recorded along this diffusion path. The linear combination fit of these spectra using those of Np(IV) and Np(V) aquo ions as references showed that at a distance of ca. 30  $\mu\text{m}$  from the OPA-water interface  $12 \pm 5\%$  of the initial Np(V) has been reduced to Np(IV) (figure 2 (b)). The degree of Np reduction increases with distance and reaches  $26 \pm 5\%$  at 525  $\mu\text{m}$  (figure 2 (c)). An even higher degree of Np reduction of approximately  $80 \pm 5\%$  was observed near a spot with increased Fe concentration at a diffusion distance of 450  $\mu\text{m}$  in a similar long-term diffusion experiment (sample not shown here). This further corroborates the role of the Fe(II)-bearing minerals as described in section 3.1.

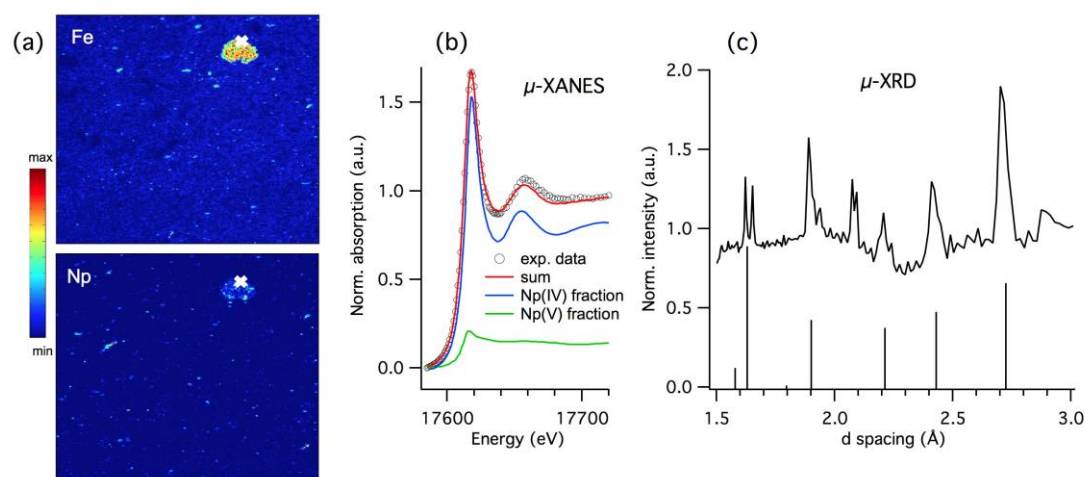


**Figure 1.** (a)  $\mu$ -XRF elemental distribution maps of Fe and Np ( $2 \times 2$  mm, step size 10  $\mu\text{m}$ ). (b) Normalized Np  $L_3$ -edge  $\mu$ -XANES spectrum measured on the spot marked with a white cross in the XRF map together with the fractions of Np(IV) and Np(V) reference spectra. (c) Intensity vs. d-spacing plot obtained by  $\mu$ -XRD mapping of the same spot ( $20 \times 20$   $\mu\text{m}$ , step size 1  $\mu\text{m}$ ). The vertical bars are calculated reflections of pyrite (ICSD database, collection code 43716).

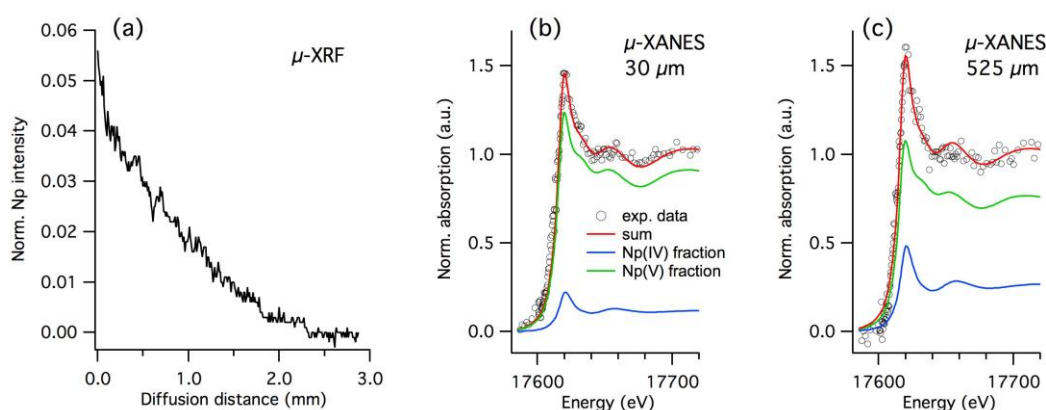


**Figure 2.** (a) Normalized neptunium intensity vs. diffusion distance derived from  $\mu$ -XRF ( $3.0 \times 1.0$  mm, step size 10  $\mu\text{m}$ ). (b) and (c) Normalized Np  $L_3$ -edge  $\mu$ -XANES spectra measured at distances of 30  $\mu\text{m}$  and 525  $\mu\text{m}$  together with the fractions of Np(IV) and Np(V) reference spectra.



#### 4. Conclusions

Although wet-chemistry experiments are important for the determination of parameters quantifying the sorption and diffusion of Np in natural clay, these experiments cannot provide the molecular-level understanding that is needed to support the safety analysis of future high-level nuclear waste repositories. The combination of spatially resolved X-ray microprobe methods (e.g.  $\mu$ -XRF,  $\mu$ -XANES,  $\mu$ -XRD) is a powerful tool for determining the distribution and speciation of actinides in heterogeneous systems like natural clays.

After sorption of 8  $\mu$ M Np(V) on Opalinus Clay at pH 7 under anaerobic conditions,  $\mu$ m-size spots were detected where tetravalent Np is the dominating species. The Fe(II)-bearing mineral pyrite acts as an important redox-active mineral phase. In the long-term diffusion experiment with 8  $\mu$ M Np(V) and Opalinus Clay pore water (pH 7.6) as mobile phase, the speciation of Np could be mapped along the diffusion path parallel to the bedding of the clay. These Np  $L_3$ -edge  $\mu$ -XANES measurements showed that mobile Np(V) is immobilized in Opalinus Clay as Np(IV) by progressive reduction along its diffusion path, further consolidating the suitability of argillaceous rocks with regard to the long-term storage of Np-containing nuclear waste.

#### Acknowledgement

This work was financed by the Federal Ministry for Economic Affairs and Energy (contract no. 02E10166, 02E10981) and TALISMAN (contract no. TALI-C01-15, TALI-C03-09). D. R. Fröhlich was supported by a fellowship of DFG-GRK 826. We are grateful to C. Borka and V. A. Samson for their support of the synchrotron measurements at the microXAS beamline at the Swiss Light Source, Paul Scherrer Institut, Switzerland. We thank Ch. Marquardt (Institute for Nuclear Waste Disposal, Karlsruher Institut für Technologie) for providing OPA bore core samples.

#### References

- [1] Wu T, Amayri S, Drebert J, Van Loon L R and Reich T 2009 Neptunium(V) sorption and diffusion in Opalinus Clay *Environ. Sci. Technol.* **43** 6567–71
- [2] Fröhlich D R, Amayri S, Drebert J and Reich T 2011 Sorption of neptunium(V) on Opalinus Clay under aerobic/anaerobic conditions *Radiochim. Acta* **99** 71–7
- [3] Fröhlich D R, Amayri S, Drebert J and Reich T 2012 Influence of temperature and background electrolyte on the sorption of neptunium(V) on Opalinus Clay *Appl. Clay Sci.* **69** 43–9
- [4] Fröhlich D R, Amayri S, Drebert J, Grolimund D, Huth J, Kaplan U, Krause J and Reich T 2012 Speciation of Np(V) uptake by Opalinus Clay using synchrotron microbeam techniques *Anal. Bioanal. Chem.* **404** 2151–62
- [5] Van Loon L R, Soler J M and Bradbury M H 2003 Diffusion of HTO,  $^{36}\text{Cl}^-$  and  $^{125}\text{I}^-$  in Opalinus Clay samples from Mont Terri – Effect of confining pressure *J. Contam. Hydrol.* **61** 73–83



## **Speciation study of Np diffusion in Opalinus Clay**

### **Statement about the contribution to the manuscript of the authors named:**

Dr. S. Amayri and Prof. Dr. T. Reich assisted the measurements at the SLS in Villigen, Switzerland. R. Scholze supported the modeling of the diffusion profiles. The measurements were performed under assistance of Dr. D. Grolimund, the group leader of the microXAS beamline (SLS, PSI, Villigen, Switzerland). P. J. B. Börner was responsible for the diffusion and sorption experiments and took the main part in the data evaluation, including the calculation of the diffusion profiles and analysis of the XANES data.

# Speciation study of Np diffusion in Opalinus Clay

Prashánta J. B. Börner, Samer Amayri, Raphael Scholze, Daniel Grolimund, Tobias Reich

## **Abstract**

This study focuses on the understanding of the migration of the hazardous long-lived Np from a radioactive waste repository in argillaceous rock into the environment by using multiple synchrotron-based microscopic methods. The unique combination of  $\mu$ -XANES,  $\mu$ -XRD, and  $\mu$ -XRF proved the reducing capabilities of pyrite towards Np(V) during its diffusion in OPA. Measured  $\mu$ -XANES spectra at randomly chosen spots yielded an average Np(IV) fraction of  $36 \pm 13\%$ , while measurements at Np “hot-spots” showed high Np(IV) fractions up to 100%. Deviations in the  $\mu$ -XANES spectra of randomly chosen spots with aquatic reference spectra were attributed to a sorbed Np(V) species. The investigation of the Np(V) diffusion in a high saline background electrolyte (1 M NaCl) in OPA showed a stronger retardation than the experiments with OPA pore water, due to an elevated pH and less contained sorption competing bivalent cations.

Keywords: Neptunium, diffusion, Opalinus Clay,  $\mu$ -XANES,  $\mu$ -XRD,  $\mu$ -XRF, migration

## **Introduction**

Argillaceous rocks are considered as potential host rock formations and principal components of barrier and backfill materials of a high level nuclear waste repository [1, 2]. In this regard, the migration of the hazardous, long-lived transuranium actinide  $^{237}\text{Np}$  ( $t_{1/2} = 2.1 \times 10^6$  a) from such a repository into the environment has to be studied intensively. The development of a robust and dynamic reactive transport model for the migration of Np must be one of the first aims in the future. The primary intention of the following study was to get the mandatory needed information by combining the synchrotron-based microscopic techniques  $\mu$ -XRF,  $\mu$ -XRD, and  $\mu$ -XANES applied on a time series (61 d, 83 d) of Np diffusion profiles in Opalinus Clay (OPA, from Mont Terri, Switzerland) at various chemical conditions, revealing the nexus between the Np diffusion pattern and the local Np speciation in a chemical image. The determination of the Np speciation was done by numerous  $\mu$ -XANES measurements along its diffusion path, whereas the local  $\mu$ -scale mineral surrounding was extracted from  $\mu$ -XRF and  $\mu$ -XRD images. All synchrotron-based measurements were performed at the  $\mu$ XAS beamline at the SLS (PSI, Villigen, Switzerland).

In previous studies the migration and sorption behaviour of Np(V) on different clay minerals such as kaolinite, montmorillonite, illite, and OPA was investigated intensively under aerobic and anaerobic conditions using clay powders, thin sections, and bore cores showing the

importance of experimental conditions like pH, redox potential, Np concentration, and ionic strength [3-12]. Also the Np(V) migration behaviour has been investigated by diffusion experiments with clay and clay minerals, but much less data is available for that [10, 13-15]. However, diffusion studies in natural host rock are most important for the verification of the specific assumed radionuclide migration behaviour, as they are closer to natural conditions.

As Np is a redox-active radionuclide it can occur as Np(V) and Np(IV) under natural conditions. Np(V) is the more hazardous species, as it is more mobile in contrast to the less soluble and strongly sorbing Np(IV) species, so that in this work the focus for experiments related to deep geological repositories for high radioactive waste lies on Np(V). The diffusion of Np(IV) is, due to the strong retardation difficult to study, but was realized by investigating the diffusion of  $\text{Np}^{\text{IV}}(\text{CO}_3)_2(\text{OH})_2^{2-}$  (with 0.3 mol/L  $\text{NaHCO}_3$ ) under anaerobic conditions in compacted sand-bentonite [16]. However, very little is known about possible reduction processes of Np(V) during the diffusion in natural argillaceous rock. Even though the uptake of Np(V) on OPA thin sections has been studied with spatially resolved synchrotron techniques, showing Np(IV) agglomerations on the sample surface and increased Np(IV) ratios at a mineral phase of pyrite [5], these techniques have not yet successfully applied on diffusion samples.

Nevertheless, the redox sensitivity of Np and the complexity of the heterogeneous OPA require the combination of both, a diffusion and a speciation investigation. Therefore, the objectives of the present study were the determination of the Np speciation after diffusion and the determination of the Np(V) diffusion parameters in dependency of diffusion time and background electrolyte.

## ***Materials and methods***

### **Opalinus Clay**

In the present work OPA was used as reference material for a natural argillaceous rock. Its geological formations reach geographically from Northern Switzerland to Southern Germany. The experiments used aerobic OPA bore cores (BLT-14) provided from the Felslabor Mont Terri, Switzerland. The mineral composition and the content of trace elements of the used OPA measured by XRF analyses are given elsewhere [5]. In general, OPA from Mont Terri consists of several clay minerals ( $22 \pm 2\%$  kaolinite,  $23 \pm 2\%$  illite,  $11 \pm 2\%$  illite/smectite mixed layers and  $10 \pm 2\%$  chlorite),  $14 \pm 4\%$  quartz,  $13 \pm 8\%$  calcite and  $4 \pm 2\%$  Fe(II)-bearing minerals (pyrite und siderite). Additionally, it contains small amounts of albite ( $1 \pm 1\%$ ), K-feldspars ( $1 \pm 1\%$ ), and organic carbon ( $1 \pm 1\%$ ). The average dry density of the intact OPA bore cores was about  $2400 \text{ kg/m}^3$  [2].

### Background electrolyte solutions

Synthetic OPA pore water was used as mobile phase (background electrolyte) for the diffusion cells Np-0, Np-1, and Np-3. The composition is given in Table 1 and was prepared in contrast to the literature [17] without Sr-cations for better  $\mu$ -XRF measurements of Np. It has a pH of 7.6 and an ionic strength of  $\sim 0.4$  M with an Eh-value of 0.45–0.5 V (SHE). Cell Np-2 was conditioned with 1 M NaCl equilibrated with  $\text{CaCO}_{3(s)}$  at pH 8.1. This approach has been chosen to improve the preconditioning of the bore core in order to prevent any dissolution of calcite contained in OPA. However, according to studies of Kumar is the  $\text{Ca}^{2+}$  concentration from dissolved  $\text{CaCO}_{3(s)}$  is with calculated  $3.7 \cdot 10^{-3}$  M expected to be in a negligible concentration range for this experiment [18].

**Table 1:** Composition of the Sr-free Synthetic OPA pore water.

Components	mol/L
$\text{Na}^+$	0.240
$\text{K}^+$	0.002
$\text{Mg}^{2+}$	0.017
$\text{Ca}^{2+}$	0.026
$\text{Cl}^-$	0.300
$\text{SO}_4^{2-}$	0.014
$\text{CO}_3^{2-}$	0.001

### Radionuclide stock solution and $\gamma$ -ray spectroscopy

The preparation of the  $^{237}\text{Np(V)}$  stock solution followed the procedure described in [4] and was verified by UV-Vis absorption spectroscopy using the characteristic absorption band of Np(V) at 980.4 nm. The  $^{237}\text{Np(V)}$  concentration was determined by  $\gamma$ -ray spectroscopy using the  $^{237}\text{Np}$   $\gamma$ -lines at 29.37 keV and 86.48 keV as it was also done for the activities in the bore cores after the diffusion experiment. The resulting stock solution had a pH value of about 1.5 and a concentration of  $8 \times 10^{-3}$  M  $^{237}\text{Np(V)}$ .

### Diffusion experiments and sample preparation

A short description of the prepared diffusion cells is given in Table 2. The cell Np-0 used a PEEK diffusion cell with a bore core placed in epoxy resin without any attached filters at the interfaces to the reservoirs. All other diffusion experiments (Np-1/2/3) used aerobic OPA bore core cylinders of about 25 mm in diameter and a thickness of 11 mm, placed between two stainless steel filter plates in a stainless steel diffusion cell. This setup is well approved for

diffusion experiments [10, 19]. Therefore, only the results of the stainless steel diffusion cells were taken for the diffusion modeling. The layering of the clay in the bore cores is very relevant for the diffusion, as described in [20]. For all our samples the direction of Np diffusion was parallel to the bedding of the clay. This is needed for an eased cleaving of the OPA bore cores along the diffusion axis and to obtain unaffected sample surfaces.

**Table 2:** Description of the diffusion experiments.

Sample	Np-0	Np-1	Np-2	Np-3
<b>Background electrolyte</b>	OPA PW	OPA PW	1 M NaCl	OPA PW
<b>pH</b>	7.6	7.6	8.1	7.6
<b>Diffusion time /d</b>	28	61	61	83

The bore cores from the cells Np-1/2/3 were characterized by HTO through-diffusion experiments analogously to [10]. The distribution coefficient  $K_d$  for the non-sorbing HTO is 0. This can be calculated for sorption and diffusion experiments with eq 1 and 2, respectively.

$$K_d \left( \frac{m^3}{kg} \right) = \frac{x}{m} \times \frac{1}{[An]_{eq}}, \quad (1)$$

where  $[An]_{eq}$  is the equilibrium concentration of the sorbate in solution,  $x$  is the mol of sorbat and  $m$  the mass of sorbent. The rock capacity factor  $\alpha$  is related to the distribution coefficient by eq 2 with the diffusion-accessible porosity  $\varepsilon$  and the bulk density  $\rho$ .

$$\alpha = \varepsilon + \rho \cdot K_d. \quad (2)$$

This means for HTO, that  $\alpha$  equals the diffusion-accessible porosity  $\varepsilon$ , which follows the approach of [10, 21] and can be read elsewhere.

The results of the HTO characterisations of the bore cores are listed in Table 3. As one can see, the determined  $D_e$  values are with  $\sim 4.7 \cdot 10^{-11} \text{ m}^2/\text{s}$  in good agreement with those for the parallel diffusion of HTO in OPA from field and laboratory experiments with  $4\text{--}5 \cdot 10^{-11} \text{ m}^2/\text{s}$  [20, 22].

**Table 3:** Results of the HTO through-diffusion experiments for  $\varepsilon$  and  $D_e$  in OPA from Mont Terri parallel to the bedding.

	$\varepsilon$	$D_e / 10^{-11}$ $\text{m}^2/\text{s}$
<b>Np-1</b>	$0.11 \pm 0.02$	$4.7 \pm 0.5$
<b>Np-2</b>	$0.13 \pm 0.02$	$4.9 \pm 0.5$
<b>Np-3</b>	$0.14 \pm 0.02$	$4.4 \pm 0.5$
<b>Lit. [20]</b>	$0.15 \pm 0.03$	$5.4 \pm 0.4$
	$0.17 \pm 0.02$	$5.4 \pm 0.4$
<b>Lit. [22]</b>	$0.15 \pm 0.02$	$4 \pm 0.4$

For the measurements at the PSI  $\mu$ XAS beamline only samples with a smooth surface were chosen. In this way intensity distortions in the  $\mu$ -XRF mappings of the diffusion profiles can be prevented. As can be seen in Table 2, the diffusion of Np(V) in OPA was investigated by the cells Np-1/2/3 in dependency of time (61 and 82 days) and background electrolyte (synth. OPA pore water without  $\text{Sr}^{2+}$  and 1 M NaCl solution equilibrated with solid  $\text{CaCO}_3$ ).

The diffusion cell with 1 M NaCl solution as background electrolyte (Np-2) was used as a diffusion study regarding higher saline groundwaters as they are relevant for potential repositories in argillaceous host rock formations in Northern Germany. All diffusion experiments were carried out under ambient air at  $24 \pm 2$  °C. The experimental setup for all samples followed the procedure of the through-diffusion experiments by Van Loon et al. [19], as also used in our studies in [10].

### Synchrotron measurements and data evaluation

Spatially resolved synchrotron radiation measurements ( $\mu$ -XRF,  $\mu$ -XANES, and  $\mu$ -XRD) were performed at the microXAS beamline at the Swiss Light Source, Paul Scherrer Institute (PSI), Switzerland [23] using a Kirkpatrick-Baez mirror micro focusing system and a double-crystal monochromator with three different crystal pairs (Si (111), Si (311), and Ge (111)). In this experiment, a pair of Si(111) crystals was used. The synchrotron ring current was about 400 mA during the measurements.

X-ray fluorescence was measured using a Ketek single-element Si-detector, which was orientated perpendicular to the synchrotron beam for a minimization of scattered radiation. Fast on-the-fly  $\mu$ -XRF scans of elements (Si, S, K, Ca, Ti, Mn, Fe, Zn, Rb, Sr) contained in OPA were collected at an excitation energy above the Np  $L_{III}$ -edge in He counterflow to reduce absorptions by air. Scans in  $\text{mm}^2$  size were taken with a step size of 10  $\mu\text{m}$  and areas of specific interest were scanned with a step size of 5  $\mu\text{m}$  using a beam size of about 5  $\mu\text{m}$ . The inflection



point of the first derivative from the Zr K-edge at 17.998 keV of a Zr foil was used for energy calibration. As Sr has a high abundance in OPA (>200 µg/g OPA), the Np L $\alpha$  fluorescence (E(L $\alpha$ ) = 13.95 keV) is covered by the Sr K $\alpha$  fluorescence (E(K $\alpha$ ) = 14.16 keV). Therefore, the Np  $\mu$ -XRF images were achieved by a subtraction of  $\mu$ -XRF mappings of Sr, with an excitation energy of 17.55 keV, from those using 17.62 keV, which is above the Np L $\text{III}$ -edge of 17.61 keV (edge-contrast method).

The final 2D Np diffusion profile calculation was done with the program MATLAB using the  $\mu$ -XRF images as 3D matrices. From each column of the respective matrix parallel to the solid/liquid interface the average fluorescence intensity was taken. Afterwards the background intensity was determined from areas without Np and subtracted. For further diffusion modeling the obtained diffusion profiles displaying absolute Np intensities of the  $\mu$ -XRF images were transformed into Np activities  $c_n$  within the rock in Bq/g. Therefore, the area  $F_{total}$  (in abs. Np intensity·mm) of the profiles

$$F_{total} = \sum F_n, \quad (3)$$

defined as the sum of all partitions  $F_n$  of the diffusion profile, was equated with the total Np activity  $A_{total}$  (Bq) of the specific bore core, as determined by  $\gamma$ -spectroscopy. The activity  $A_n$  (Bq) of the partitions was calculated from eq 4 as

$$A_n = F_n/F_{total} \cdot A_{total}. \quad (4)$$

The related partition mass  $m_n$  (g) was calculated according to the bore core density and the final Np concentration  $c_n$  (Bq/g) within the partition of the rock

$$c_n = A_n/m_n. \quad (5)$$

This procedure was done on the assumption of a homogenous distribution of the Np activity according to the respective diffusion profile.

Furthermore, MATLAB was used to fit the diffusion parameters  $K_d$  and  $D_e$  according to the Np concentration within the rock  $A_r$  (Bq/g) using equations 6 and 7 for the in-diffusion and filter correction from Wu et al. and Yaroshchuk et al. [10, 21],

$$A_r = \frac{V_{pw} + m \cdot K_d}{m} \cdot C_0 \cdot C(\xi, \tau), \quad (6)$$

with  $V_{pw}$  as the volume of the specific pore water in m<sup>3</sup>,  $m$  the mass of the bore core in kg, and  $C(\xi, \tau)$  for the inverse Fourier transforms of the concentration profile defined as by eq 4,

$$C(\xi, \tau) = \frac{\exp(-\frac{\xi^2}{4\tau})}{\sqrt{1-4\kappa}} \left\{ \begin{array}{l} \text{erfc} \left[ \frac{\xi}{2\sqrt{\tau}} + (1 - \sqrt{1-4\kappa}) \cdot \frac{\sqrt{\tau}}{2} \right] - \\ \text{erfc} \left[ \frac{\xi}{2\sqrt{\tau}} + (1 + \sqrt{1-4\kappa}) \cdot \frac{\sqrt{\tau}}{2} \right] \end{array} \right\} \quad (7)$$

where  $\text{erfc}(z) \equiv \exp(z^2) \cdot \text{erfc}(z)$  and the following dimensionless variables and parameters, which are defined as  $\tau \equiv \frac{t}{t_{ch}}$ ,  $\xi \equiv \frac{x}{l_f}$ ,  $\kappa \equiv t_{ch} \cdot S \cdot \frac{P_f}{V}$ ,  $t_{ch} \equiv \alpha \cdot \frac{D_e}{P_f^2}$ , and  $P_f \equiv \frac{D_{fe}}{l_f}$ , with  $l_f$  (m) as the filter thickness,  $x$  (m) the diffusion distance, and  $P_f$  (m/s) the diffusion permeability of the radionuclide in the filter, the diffusion time  $t$ , the surface of the solid/liquid interface  $S$ , and  $V = V_{pw}$ . The retarding effect of the used stainless steel filter is included in  $D_{fe}$  (m<sup>2</sup>/s), the diffusion coefficient of Np(V) in the filter, as determined by Wu et al..

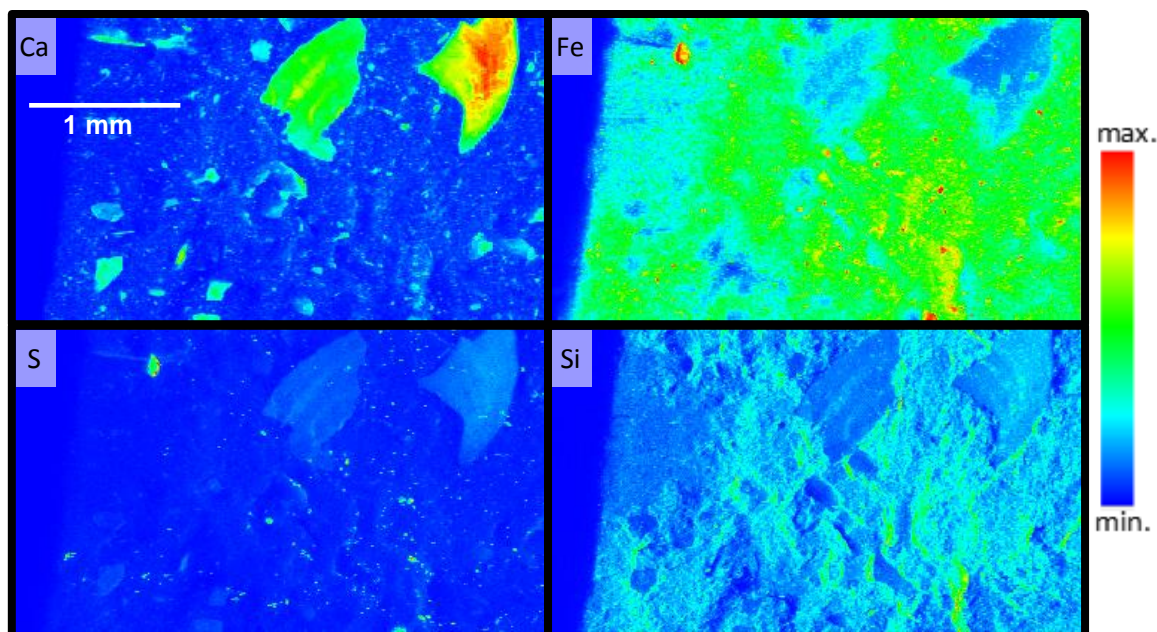
Np L<sub>III</sub>-edge  $\mu$ -XANES were measured in fluorescence mode. Dead time corrections were performed using an in-house java applet code. Background removal and energy correction, as well as normalisation of the collected XANES spectra was done with the program ATHENA [24]. This program contains a linear combination fit routine (LCF) which was used for the determination of the Np(IV)/Np(V) ratios. The required reference spectra were taken from [25] with a fixed energy position of the inflection point of the first derivative of the Np(V) spectra which was 2.4 eV lower relative to Np(IV) and with a 2.0 eV lower white line position according to [26, 27].

A Pilatus 100K detector was used for the  $\mu$ -XRD measurements and calibrated with Al<sub>2</sub>O<sub>3</sub>. The measured diffraction patterns of the clay samples were further analysed with the program XRDUA [28].

## **Results and discussion**

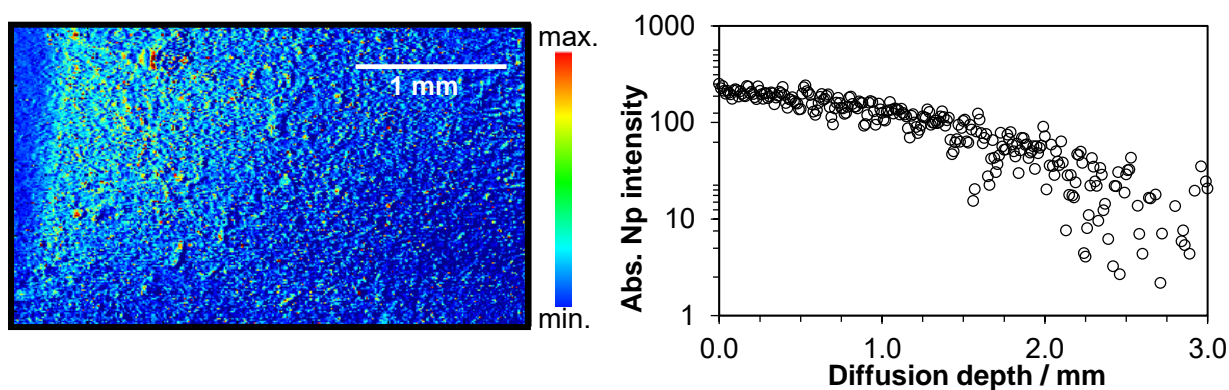
### **Diffusion**

Figure 1 shows the results of a  $\mu$ -XRF scan of sample Np-3 for the most representative elements displaying the OPA heterogeneity, which are Ca, Fe, S, and Si. The scan has a size of 3.5 × 2.0 mm<sup>2</sup> and was performed with a step size of 10  $\mu$ m at an energy of 17620 eV. One can see a correlation between the elements Fe and Si, which are again anti-correlated to Ca. Fe cations are known to be incorporated in the atomic lattice of clay minerals such as illite. Correlations between S and Fe further indicate pyrite phases. However, the S intensity is also slightly increased in some Ca enrichments, which were thought to be mostly CaCO<sub>3</sub>. Anyhow, Gypsum (CaSO<sub>4</sub>) is mineralogical often correlated with phases of calcite [29].



**Figure 1:**  $\mu$ -XRF mappings showing the natural distribution of the elements Ca, Fe, S, and Si in sample Np-3. The investigated area is  $3.5 \times 2.0 \text{ mm}^2$  and was scanned with a step size of  $10 \text{ }\mu\text{m}$  at  $17620 \text{ eV}$ .

The Np distribution of the same area of sample Np-3 is shown in Figure 2 together with the 2D diffusion profile displaying the extracted absolute Np intensities from the XRF image. As mentioned, this was also done for the Np diffusion profiles of sample Np-1 and Np-2 and can be seen in the supplementary information. As the Np concentration was used for diffusion modeling, Figure 3 shows the diffusion profiles of the samples Np-1/2/3 with the Np activity in rock (Bg/g) and the fit curves.



**Figure 2:** Np  $\mu$ -XRF mapping of sample Np-3 (left) from the same area as shown in Figure 1 and the corresponding 2D diffusion profile (right).

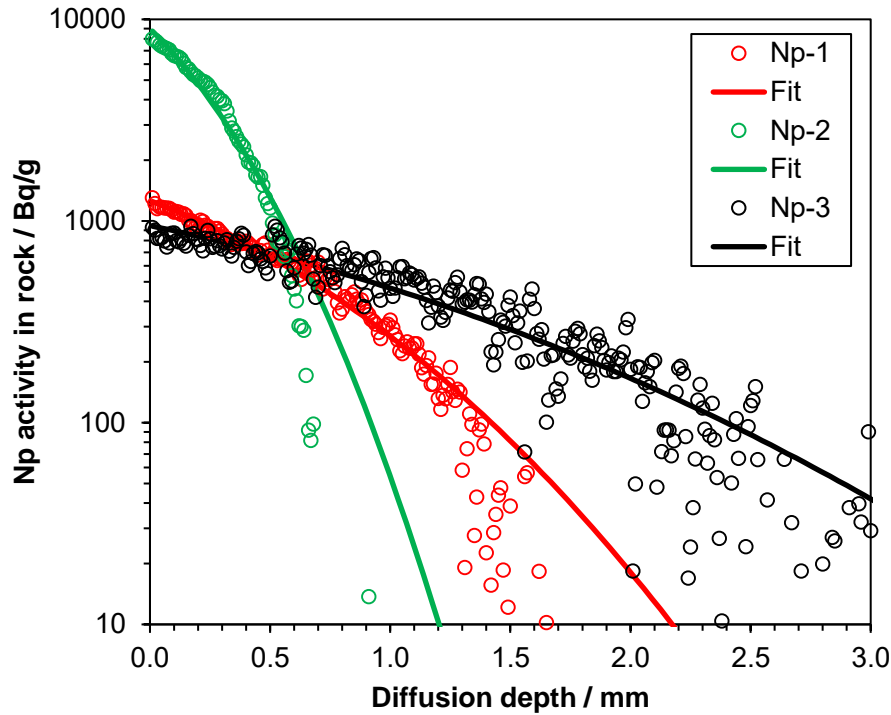


**Figure 3:** Diffusion profiles of the samples Np-1/2/3 with Np activity in Opalinus Clay in Bq/g and the modeled fit curves of the Np diffusion.

The shortest diffusion depth of Np is reached for Np-2 (61 days) with 700  $\mu\text{m}$ , followed by Np-1 (61 days) with 1.5 mm and the widest with about 2.5 mm for Np-3 (83 days). The total Np accumulation on the primary interface differs between the green data series of Np-2 and the other two cells. As the Np concentration in the reservoirs have been the same (8  $\mu\text{M}$ ) this difference can be explained by the strong sorption competing effect of divalent cations on the sorption of Np(V), as described by Fröhlich et al. [30], enhanced by the slightly increased pH of 8.1 compared to 7.6. The mobile phase of Np-2 is equilibrated with  $\text{CaCO}_3$ , but the concentration of divalent cations in OPA pore water (as shown in Table 1) is higher by a factor of 10. Compared to divalent cations the influence of the  $\text{Na}^+$  concentration on the Np(V) sorption is negligible [30, 31]. This also corresponds to the obtained  $\log(K_d)$  values from sorption isotherms of related batch experiments with  $1.4 \pm 0.1$  in OPA PW (pH 7.6, [10]) compared to determined  $2.3 \pm 0.1$  in 1 M NaCl (sat. with  $\text{CaCO}_{3(s)}$ , pH 8.1, as shown in this work) in Table 4. Furthermore, the sorption results from diffusion modeling are in good agreement with those obtained from batch experiments, which are shown in Table 4 together with the results for  $D_e$ ,  $\alpha$ , and  $\varepsilon$ . Both diffusion cells with OPA PW (Np-1 and Np-3) have an average  $D_e$  of  $6.3 \cdot 10^{-12} \text{ m}^2/\text{s}$ , which is comparable to the  $D_e$  of  $6.9 \cdot 10^{-12} \text{ m}^2/\text{s}$  of Wu et al. [10]. It seems that the OPA bedding has no effect on the calculated  $D_e$  values. However, the  $\log(K_d)$  and  $\alpha$  values of Wu et al. appear to be affected by the perpendicular bedding, as these values

are considerably higher than the values from this diffusion experiment and the related batch experiments. However, in contrast to the diffusion profile analysis using the abrasive method, the area of evaluation is in this experiment much smaller and  $\mu\text{m}$ -scale heterogeneities cause stronger deviations. The difference of the  $D_e$  values between Np-1 and Np-3 of a factor of about 2 demonstrates the influence of the heterogeneity of OPA. In this regard the results of Np-2 must be seen with additional caution.

**Table 4:** Fit results of the Np diffusion profiles for the distribution coefficient  $K_d$ , the effective diffusion  $D_e$ , the rock capacity factor  $\alpha$ , the diffusion-accessible porosity  $\varepsilon$  and the accumulated Np activity in the bore Cores.

Diffusion cell	$\log(K_d / \text{L/kg})$	$D_e \times 10^{-12} / \text{m}^2/\text{s}$	$\alpha$	$\varepsilon$	Accumulated total Np activity / Bq	OPA bedding
Np-1	$1.4 \pm 0.1$ ( $1.4^{*[10]}$ )	$4.4 \pm 4.0$	$65 \pm 6$	$0.11 \pm 0.02$	$964 \pm 48$	parallel
Np-2	$2.6 \pm 0.1$ ( $2.3^*$ )	$12.8 \pm 4.0$	$862 \pm 78$	$0.13 \pm 0.02$	$2174 \pm 109$	parallel
Np-3	$1.3 \pm 0.1$ ( $1.4^{*[10]}$ )	$8.3 \pm 4.0$	$49 \pm 4$	$0.14 \pm 0.02$	$1294 \pm 65$	parallel
Wu et al. [10]	$2.0 \pm 0.04$ ( $1.4^*$ )	$6.9 \pm 1.1$	$243 \pm 4$	$0.15 \pm 0.01$	-	perpendicular

\* Value from batch experiment

### Speciation

Figure 4 shows three normalized Np L<sub>III</sub>-edge  $\mu\text{-XANES}$  spectra of spots chosen along the diffusion profile of sample Np-1. 30  $\mu\text{m}$  behind the interface one can see a fraction of 14% Np(IV). The height of the white line increases notably from the first to the next spot at 144  $\mu\text{m}$  resulting in 33% Np(IV). However, this value does not further change in any significant extent, as shown with the last spectra in this figure at 675  $\mu\text{m}$ . A summary of all  $\mu\text{-XANES}$  measurements is presented in Figure 5, where the determined Np(IV) fraction is plotted against the diffusion distance in  $\mu\text{m}$  (see SI for the detailed table).

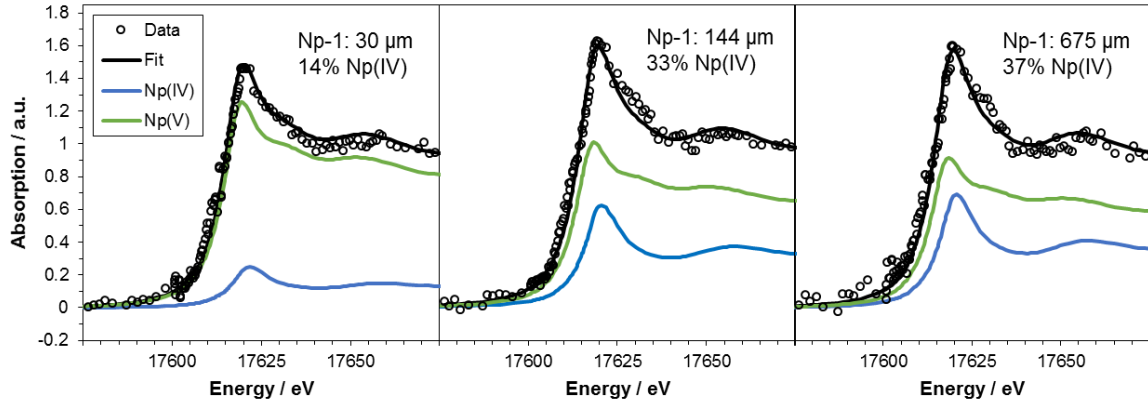


**Figure 4:** Normalized Np L<sub>III</sub>-edge  $\mu$ -XANES along the diffusion profile of sample Np-1 at 30  $\mu\text{m}$ , 144  $\mu\text{m}$ , and 675  $\mu\text{m}$  diffusion depth.

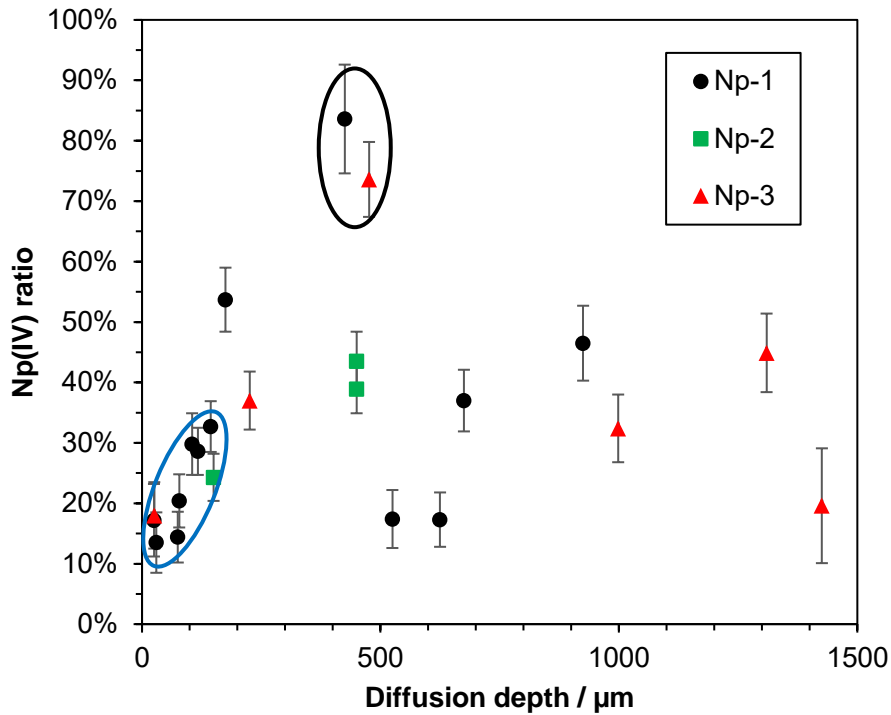


**Figure 5:**  $\mu$ -XANES from the diffusion samples Np-1/2/3. The blue circle covers the range of a possible redox gradient and the black circle two spots with exceptional high Np(IV) fractions.

On the first  $\sim 150 \mu\text{m}$  diffusion depth increases the Np(IV) fraction from 10% and up to about 35%. This might be explained by the different redox potentials of the pore water outside and inside the clay, leading to a redox gradient on the first  $\mu\text{m}$  of the profiles. The other possibility could be a slower kinetic of the reduction than the diffusion of incoming Np(V). Behind those 150  $\mu\text{m}$  the following Np(IV) fractions look on the first sight quite scattered, but most of them are in the range between 20–50% Np(IV) with an average value of 36%. Only two spots at

about 500  $\mu\text{m}$  of sample Np-1 and Np-3, black encircled in Figure 5, have higher Np(IV) fractions of  $\sim 75\%$  Np(IV). To understand the reason for this extraordinary Np(V) reduction the surrounding of the spot of Np-3 at 480  $\mu\text{m}$  has been further investigated with a high resolution  $\mu\text{-XRF}$  scan ( $120 \times 170 \mu\text{m}^2$ ; step size and a beam size of 5  $\mu\text{m}$ ) and a  $\mu\text{-XRD}$  scan shown in Figure 6. These  $\mu\text{-XRF}$  scans clearly show high intensities for Fe and S and the  $\mu\text{-XRD}$  scan identifies pyrite as the responsible source. Nevertheless, small amounts of oxygenated Fe(II) species as  $\text{FeS}_2(\text{OH})^-$ ,  $\text{FeO}(\text{OH})^-$ , and  $\text{FeO}(\text{OH})_2^{2-}$  may also be present, according to pH and the oxidative behavior of the mineral pyrite under the aerobic conditions of the performed experiment, including a possible passivation with Fe(III) oxyhydroxides [32-34]. However, in contrast to [5], one can see no Np uptake on the pyrite phase itself, but a lowering of the Np concentration (bottom left in Figure 6). A reason for this could be the different sample preparation, which includes in [5] polishing. A freshly polished pyrite surface shows for example a much higher uptake of Uranium than a weathered surface [35]. Note, that the effect of pyrite on its ambient redox potential stays visible from the higher grade of reduction of Np(V) to Np(IV) in the immediate surrounding.

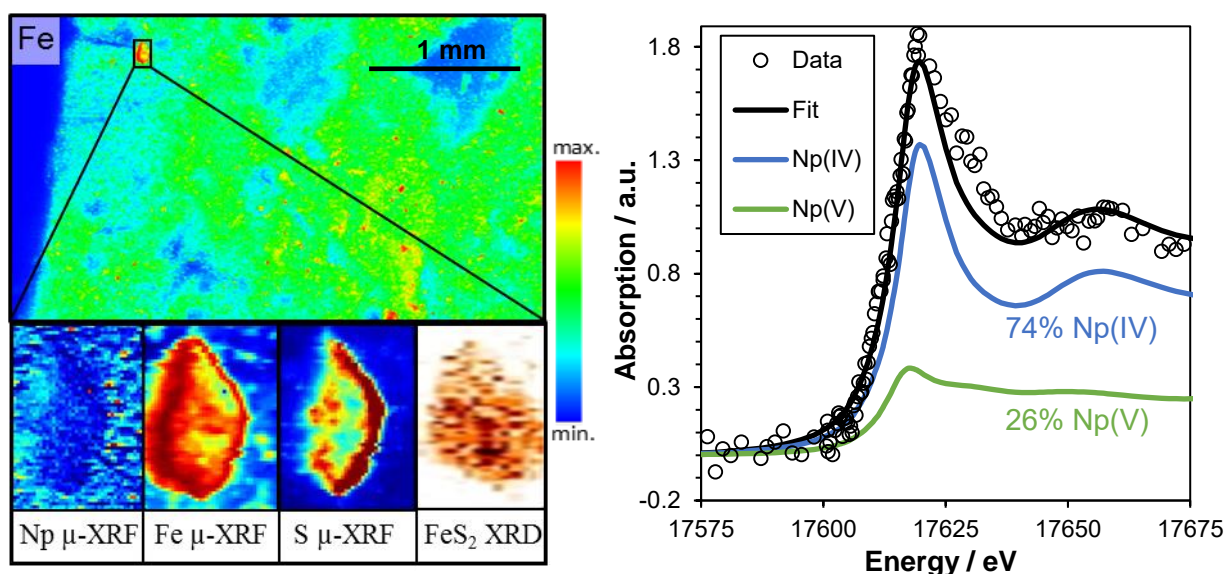


**Figure 6:** The marked area of sample Np-3 has been further investigated with a high-resolution  $\mu\text{-XRF}$  mapping ( $120 \times 170 \mu\text{m}$ , 5  $\mu\text{m}$  step size and beam size) and a  $\mu\text{-XRD}$  mapping (X-ray energy 17.62 keV), which was calculated by the reflexes around the ROI at  $2\theta = 24.5^\circ$  (also see SI). The  $\mu\text{-XANES}$  spectra (right) from this area at a diffusion distance of 480  $\mu\text{m}$  shows an increased white line corresponding to  $74 \pm 6\%$  Np(IV).

Figure 7 shows the determined fractions of Np(IV) and Np(V) from the  $\mu\text{-XANES}$  measurements in Bq/g of the samples Np-1 and Np-3. The shown fits for the Np(V) diffusion

use the same diffusion parameters as mentioned above, except that  $C_0$  was corrected for the amount reduced to Np(IV). This means a lowered  $C_0$  by subtracting the amount hold back by Np(IV) of 17% for Np-1 and 18% for Np-3 (first value at the interface of Table 5). While the Np(V) distribution shows the typical diffusive transport behavior, the distribution of the related Np(IV) shows none.

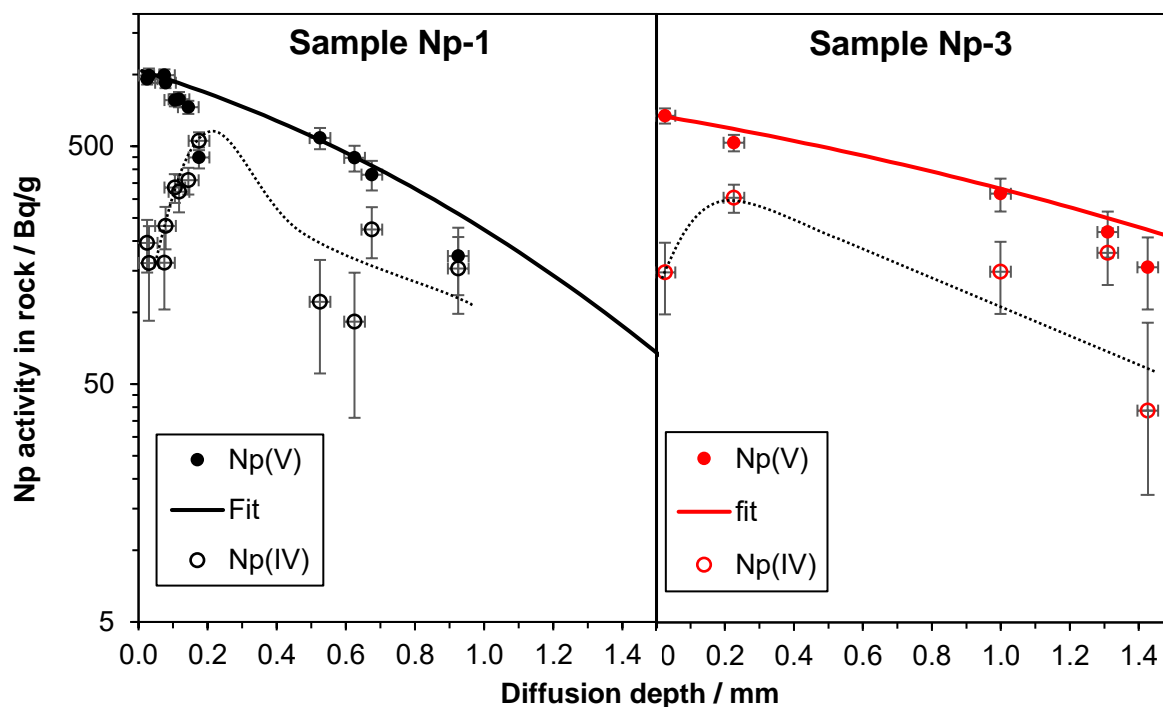


**Figure 7:** Calculations of the Np(V) and Np(IV) fractions in Bq/g of sample Np-1 and Np-3. The fits are the same as in Figure 3, except that the functions have been adjusted to the Np(V) start concentration. The dotted lines are added to guide the viewer's eye to the Np(IV) distribution.

The  $\mu$ -XANES of sample Np-0 have been measured at Np “hot spots” (with radius  $\leq 10 \mu\text{m}$ ) determined from high resolution  $\mu$ -XRF scans using the edge-contrast method. From this investigation are shown three  $\mu$ -XANES spectra in Figure 8. These Np „hot spots“ are with fractions of  $> 50\%$  stronger dominated by Np(IV) as the randomly chosen spots from the other samples. Furthermore, the Np(IV)/Np(V) ratio increases along the Np diffusion pathway, leading to 100% Np(IV) at 1700  $\mu\text{m}$  (see also SI).



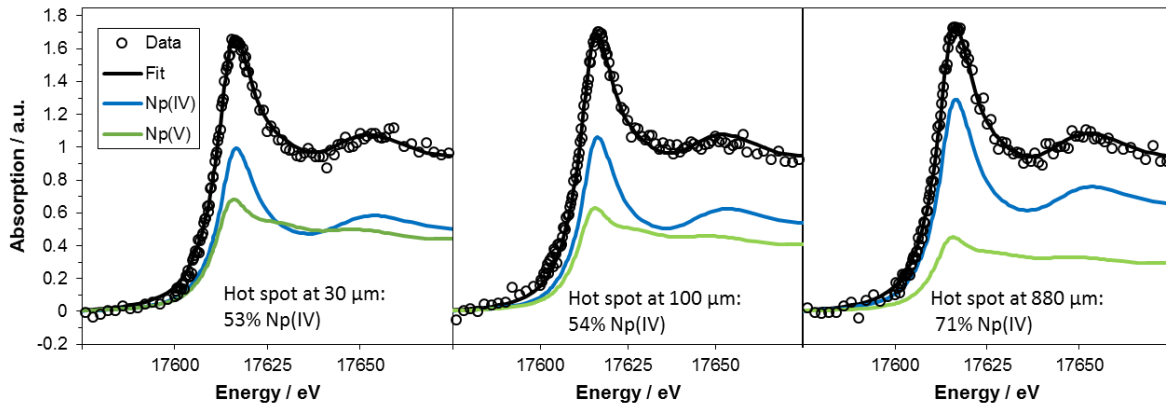


**Figure 8:** Normalized Np  $L_{III}$ -edge  $\mu$ -XANES spectra at Np „hot spots“ from the diffusion profile of Np-0.

It is also striking, that the fits for the XANES spectra of the „hot spots“ agree very well with the reference spectra from aquatic Np(IV) and Np(V) species. Merging the spectra of the representative (not encircled) spots in Figure 5 for Np-1/2/3 in Figure 9 shows in contrast to that, some deviations between the spectra and the fit with 36% Np(IV). Especially the changed shoulder on the high energy side of the main peak cannot be fixed with the used reference spectra. If the changes derive from different axial and equatorial Np-O distances due to interactions of the Np species with the OPA surface cannot be verified [36, 37]. The XANES spectra of a sorption sample prepared of montmorillonite in a solution of  $8 \cdot 10^{-6}$  M Np(V) at pH 9.5 did not show similar deviations. However, a comparison might be difficult, as the Np concentration differs with factor of  $>10^3$  mol/kg.

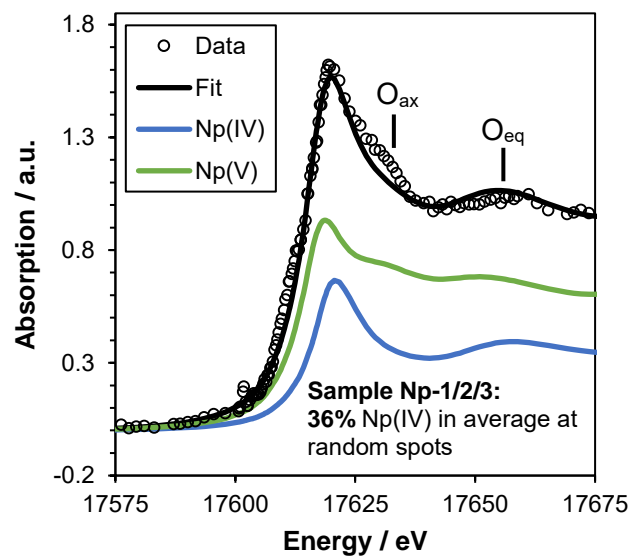


**Figure 9:** This Np  $L_{III}$ -edge  $\mu$ -XANES spectra is the merge of all not encircled spots of Np-1/2/3 in Figure 5.

## **Conclusion**

The  $\mu$ -XANES speciation investigation of the diffusion profiles of Np showed, that Np(V) is partially reduced to Np(IV) along its diffusion in the OPA bore cores even when the experiments are performed under ambient air conditions. Nevertheless, Np(V) remains with  $64\% \pm 13\%$  the dominant species and most relevant for the diffusive transport. This was shown from the randomly chosen  $\mu$ -XANES spots, as the Np “hot spots” contain a much higher fraction of Np(IV).

The combination of  $\mu$ -XANES with  $\mu$ -XRD and  $\mu$ -XRF scans at a  $\sim 100 \mu\text{m}^2$  phase of pyrite further proved that this mineral is capable of a strong Np(V) reduction in its vicinity.

The diffusion experiments provided additional data for the development of a robust and reliable reactive transport model, together with diffusion parameters for Np(V) diffusion parallel to the OPA bedding. The investigation of the diffusion of Np(V) in a high saline background electrolyte (1 M NaCl) showed a stronger retardation of Np than the experiments with OPA PW, due to the influence of the elevated pH and less sorption competing bivalent cations.

In total, this study increased the understanding of the retardation of mobile Np(V) released from a radioactive waste repository in argillaceous rock.

## **Acknowledgement**

This work has been supported by the European FP7 TALISMAN project, under contract with the European Commission (contract TALI-C01-15, TALI-C03-09).

## **References**

1. Brauer, V. and P. Hoth, *Argillaceous rock as host rock for final storage of radioactive waste in Germany*. Atw-International Journal for Nuclear Power, 2007. 52(5): p. 325.
2. NAGRA, *Projekt Opalinuston–Synthese der geowissenschaftlichen Untersuchungsergebnisse, Entsorgungsnachweis für abgebrannte Brennelemente, verglaste hochaktive sowie langlebige mittelaktive Abfälle*. Technical Report NTB 02-03, NAGRA Nationale Genossenschaft für die Lagerung radioaktiver Abfälle, Wettingen, 2002.
3. Fröhlich, D.R., S. Amayri, J. Drebert, and T. Reich, *Sorption of neptunium(V) on Opalinus Clay under aerobic/anaerobic conditions*. Radiochimica Acta, 2011. 99(2): p. 71-77.

4. Amayri, S., A. Jermolajev, and T. Reich, *Neptunium(V) sorption on kaolinite*. *Radiochimica Acta*, 2011. 99(6): p. 349-357.
5. Fröhlich, D.R., S. Amayri, J. Drebert, D. Grolimund, J. Huth, U. Kaplan, J. Krause, and T. Reich, *Speciation of Np(V) uptake by Opalinus Clay using synchrotron microbeam techniques*. *Analytical and Bioanalytical Chemistry*, 2012. 404(8): p. 2151-62.
6. Bradbury, M.H. and B. Baeyens, *Modelling sorption data for the actinides Am(III), Np(V) and Pa(V) on montmorillonite*. *Radiochimica Acta*, 2006. 94(9-11): p. 619-625.
7. Kozai, N., T. Ohnuki, and S. Muraoka, *Sorption characteristics of neptunium by sodium-smectite*. *Journal of Nuclear Science and Technology*, 1993. 30(11): p. 1153-1159.
8. Nagasaki, S. and S. Tanaka, *Sorption equilibrium and kinetics of  $NpO_2^+$  on dispersed particles of Na-montmorillonite*. *Radiochimica Acta*, 2000. 88(9-11): p. 705-709.
9. Schmeide, K. and G. Bernhard, *Sorption of Np(V) and Np(IV) onto kaolinite: Effects of pH, ionic strength, carbonate and humic acid*. *Applied Geochemistry*, 2010. 25(8): p. 1238-1247.
10. Wu, T., S. Amayri, J. Drebert, L.R. Van Loon, and T. Reich, *Neptunium(V) sorption and diffusion in Opalinus Clay*. *Environmental Science & Technology*, 2009. 43(17): p. 6567-6571.
11. Marsac, R., N.L. Banik, J. Lützenkirchen, C.M. Marquardt, K. Dardenne, D. Schild, J. Rothe, A. Diascorn, T. Kupcik, T. Schäfer, and H. Geckeis, *Neptunium redox speciation at the illite surface*. *Geochimica et Cosmochimica Acta*, 2015. 152: p. 39-51.
12. Amayri, S., D.R. Fröhlich, U. Kaplan, N. Trautmann, and T. Reich, *Distribution coefficients for the sorption of Th, U, Np, Pu, and Am on Opalinus Clay*. *Radiochimica Acta*, 2016. 104(1): p. 33-40.
13. Kozai, N., K. Inada, T. Kozaki, S. Sato, H. Ohashi, and T. Banba, *Apparent diffusion coefficients and chemical species of Np(V) in compacted Na-montmorillonite*. *Journal of Contaminant Hydrology*, 2001. 47(2-4): p. 149-158.
14. Mukai, S. and S. Kataoka, *Diffusion of some radionuclides in compacted Ca-bentonite under reducing condition*. *Radiochimica Acta*, 1998. 82: p. 179-182.
15. Tachi, Y., T. Nakazawa, M. Ochs, K. Yotsuji, T. Suyama, Y. Seida, N. Yamada, and M. Yui, *Diffusion and sorption of neptunium(V) in compacted montmorillonite: effects of carbonate and salinity*. *Radiochimica Acta*, 2010. 98(9-11): p. 711-718.
16. Yamaguchi, T., S. Nakayama, S. Nagao, and M. Kizaki, *Diffusive transport of neptunium and plutonium through compacted sand-bentonite mixtures under anaerobic conditions*. *Radiochimica Acta*, 2007. 95(2): p. 115-125.

17. Pearson, F.J., *Opalinus Clay experimental water: AI type*. PSI technical report TM-44-98-07, 1998, Villigen, Switzerland: Paul Scherrer Institut.
18. Kumar, S., A.S. Pente, R.K. Bajpai, C.P. Kaushik, and B.S. Tomar, *Americium sorption on smectite-rich natural clay from granitic ground water*. Applied Geochemistry, 2013. 35: p. 28-34.
19. Van Loon, L.R., J.M. Soler, and M.H. Bradbury, *Diffusion of HTO,  $^{36}\text{Cl}^-$  and  $^{125}\text{I}^-$  in Opalinus Clay samples from Mont Terri: Effect of confining pressure*. Journal of Contaminant Hydrology, 2003. 61(1-4): p. 73-83.
20. Van Loon, L.R., J.M. Soler, W. Müller, and M.H. Bradbury, *Anisotropic diffusion in layered argillaceous rocks: A case study with Opalinus Clay*. Environmental Science & Technology, 2004. 38(21): p. 5721-5728.
21. Yaroshchuk, A.E. and L.R. Van Loon, *Improved interpretation of in-diffusion measurements with confined swelling clays*. Journal of Contaminant Hydrology, 2008. 97(1-2): p. 67-74.
22. Van Loon, L.R., P. Wersin, J.M. Soler, J. Eikenberg, T. Gimmi, P. Hernan, S. Dewonck, and S. Savoye, *In-situ diffusion of HTO,  $^{22}\text{Na}^+$ ,  $\text{Cs}^+$  and  $\text{I}^-$  in Opalinus Clay at the Mont Terri underground rock laboratory*. Radiochimica Acta, 2004. 92(9-11): p. 757-763.
23. Borca, C.N., D. Grolimund, M. Willimann, B. Meyer, K. Jefimovs, J. Vila-Comamala, and C. David, *The microXAS beamline at the swiss light source: Towards nano-scale imaging*. Journal of Physics: Conference Series, 2009. 186: p. 012003.
24. Ravel, B. and M. Newville, *ATHENA, ARTEMIS, HEPHAESTUS: data analysis for X-ray absorption spectroscopy using IFEFFIT*. Journal of Synchrotron Radiation, 2005. 12(Pt 4): p. 537-41.
25. Reich, T., G. Bernhard, G. Geipel, H. Funke, C. Hennig, A. Rossberg, W. Matz, N. Schell, and H. Nitsche, *The Rossendorf Beam Line ROBL - a dedicated experimental station for XAFS measurements of actinides and other radionuclides*. Radiochimica Acta, 2000. 88(9-11): p. 633-637.
26. Denecke, M.A., K. Dardenne, and C.M. Marquardt, *Np(IV)/Np(V) valence determinations from Np  $L_3$  edge XANES/EXAFS*. Talanta, 2005. 65(4): p. 1008-1014.
27. Soderholm, L., M.R. Antonio, C. Williams, and S.R. Wasserman, *XANES spectroelectrochemistry: a new method for determining formal potentials*. Analytical Chemistry, 1999. 71(20): p. 4622-4628.
28. De Nolf, W., F. Vanmeert, and K. Janssens, *XRDUA: crystalline phase distribution maps by two-dimensional scanning and tomographic (micro) X-ray powder diffraction*. Journal of Applied Crystallography, 2014. 47(3): p. 1107-1117.

29. Visconti, F., J.M. De Paz, and J.L. Rubio, *Calcite and gypsum solubility products in water-saturated salt-affected soil samples at 25°C and at least up to 14 dS m<sup>-1</sup>*. European Journal of Soil Science, 2010. 61(2): p. 255-270.
30. Fröhlich, D.R., S. Amayri, J. Drebert, and T. Reich, *Influence of temperature and background electrolyte on the sorption of neptunium(V) on Opalinus Clay*. Applied Clay Science, 2012. 69: p. 43-49.
31. Li, P., Z. Liu, F. Ma, Q. Shi, Z. Guo, and W. Wu, *Effects of pH, ionic strength and humic acid on the sorption of neptunium(V) to Na-bentonite*. Journal of Molecular Liquids, 2015. 206: p. 285-292.
32. Das, D.K., P.N. Pathak, S. Kumar, and V.K. Manchanda, *Sorption behavior of Am<sup>3+</sup> on suspended pyrite*. Journal of Radioanalytical and Nuclear Chemistry, 2009. 281(3): p. 449-455.
33. Bostick, B.C., S. Fendorf, B.T. Bowie, and P.R. Griffiths, *Influence of cadmium sorption on FeS<sub>2</sub> oxidation*. Environmental Science & Technology, 2000. 34(8): p. 1494-1499.
34. Behra, P., P. Bonnissel-Gissing, M. Alnot, R. Revel, and J.J. Ehrhardt, *XPS and XAS study of the sorption of Hg(II) onto pyrite*. Langmuir, 2001. 17(13): p. 3970-3979.
35. Scott, T.B., O.R. Tort, and G.C. Allen, *Aqueous uptake of uranium onto pyrite surfaces; reactivity of fresh versus weathered material*. Geochimica et Cosmochimica Acta, 2007. 71(21): p. 5044-5053.
36. Hudson, E.A., P.G. Allen, L.J. Terminello, M.A. Denecke, and T. Reich, *Polarized x-ray-absorption spectroscopy of the uranyl ion: Comparison of experiment and theory*. Physical Review B, 1996. 54(1): p. 156-165.
37. Conradson, S.D., K.D. Abney, B.D. Begg, E.D. Brady, D.L. Clark, C. Den Auwer, M. Ding, P.K. Dorhout, F.J. Espinosa-Faller, P.L. Gordon, R.G. Haire, N.J. Hess, R.F. Hess, D.W. Keogh, G.H. Lander, A.J. Lupinetti, L.A. Morales, M.P. Neu, P.D. Palmer, P. Paviet-Hartmann, S.D. Reilly, W.H. Runde, D.C. Tait, D.K. Veirs, and F. Wastin, *Higher order speciation effects on plutonium L<sub>3</sub> X-ray absorption near edge spectra*. Inorganic Chemistry, 2004. 43: p. 116-131.

### **List of figures**

Figure 1:  $\mu$ -XRF mappings showing the natural distribution of the elements Ca, Fe, S, and Si in sample Np-3. The investigated area is  $3.5 \times 2.0 \text{ mm}^2$  and was scanned with a step size of  $10 \mu\text{m}$  at  $17620 \text{ eV}$ . ..... h

Figure 2: Np  $\mu$ -XRF mapping of sample Np-3 (left) from the same area as shown in Figure 1 and the corresponding 2D diffusion profile (right). ..... h

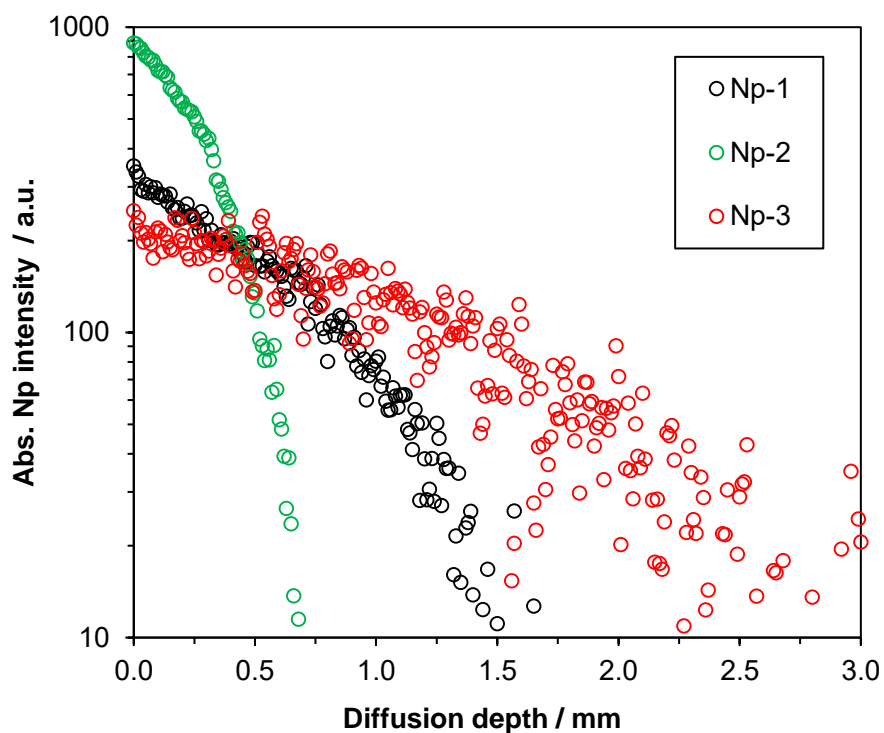
Figure 3: Diffusion profiles of the samples Np-1/2/3 with Np activity in Opalinus Clay in Bq/g and the modeled fit curves of the Np diffusion. .... i

Figure 4: Normalized Np L <sub>III</sub> -edge $\mu$ -XANES along the diffusion profile of sample Np-1 at 30 $\mu$ m, 144 $\mu$ m, and 675 $\mu$ m diffusion depth.....	k
Figure 5: $\mu$ -XANES from the diffusion samples Np-1/2/3. The blue circle covers the range of a possible redox gradient and the black circle two spots with exceptional high Np(IV) fractions. ....	k
Figure 6: The marked area of sample Np-3 has been further investigated with a high-resolution $\mu$ -XRF mapping (120 $\times$ 170 $\mu$ m, 5 $\mu$ m step size and beam size) and a $\mu$ -XRD mapping (X-ray energy 17.62 keV), which was calculated by the reflexes around the ROI at $2\Theta = 24.5^\circ$ (also see SI). The $\mu$ -XANES spectra (right) from this area at a diffusion distance of 480 $\mu$ m shows an increased white line corresponding to $74 \pm 6\%$ Np(IV). ....	l
Figure 7: Calculations of the Np(V) and Np(IV) fractions in Bq/g of sample Np-1 and Np-3. The fits are the same as in Figure 3, except that the functions have been adjusted to the Np(V) start concentration. The dotted lines are added to guide the viewer's eye to the Np(IV) distribution. ....	m
Figure 8: Normalized Np L <sub>III</sub> -edge $\mu$ -XANES spectra at Np „hot spots“ from the diffusion profile of Np-0.....	n
Figure 9: This Np L <sub>III</sub> -edge $\mu$ -XANES spectra is the merge of all not encircled spots of Np-1/2/3 in Figure 5. ....	n
Figure 10: Diffusion profiles of the samples Np-1/2/3 in absolute intensities from $\mu$ -XRF measurements. ....	t
Figure 11: Diffractogram taken from the $\mu$ -XRD mapping shown in Figure 6 for sample Np-3. The green lines represent the reference reflexes of pyrite (PDF 03-065-1211).....	u

**List of tables**

Table 1: Composition of the Sr-free Synthetic OPA pore water.....	c
Table 2: Description of the diffusion experiments. ....	d
Table 3: Results of the HTO through-diffusion experiments for $\epsilon$ and $D_e$ in OPA from Mont Terri parallel to the bedding. ....	e
Table 4: Fit results of the Np diffusion profiles for the distribution coefficient $K_d$ , the effective diffusion $D_e$ , the rock capacity factor $\alpha$ , the diffusion-accessible porosity $\epsilon$ and the accumulated Np activity in the bore Cores. ....	j
Table 5: Percentages of Np(IV) fractions from LCF Calculations for Np-1/2/3 in Dependency of the Diffusion Distance in $\mu$ m.....	t

## Supplementary information



**Figure 10:** Diffusion profiles of the samples Np-1/2/3 in absolute intensities from  $\mu$ -XRF measurements.

**Table 5:** Percentages of Np(IV) fractions from LCF Calculations for Np-1/2/3 in Dependency of the Diffusion Distance in  $\mu\text{m}$ .

Np-0 (PW, 28 d)		Np-1 (PW, 61 d)		Np-2 (1 M NaCl, 61 d)		Np-3 (PW, 83 d)	
$\mu\text{m}$	Np(IV) /%	$\mu\text{m}$	Np(IV) /%	$\mu\text{m}$	Np(IV) /%	$\mu\text{m}$	Np(IV) /%
30	$53 \pm 2$	25	$17 \pm 6$	150	$24 \pm 4$	26	$18 \pm 6$
100	$54 \pm 2$	30	$14 \pm 5$	450	$44 \pm 5$	226	$37 \pm 5$
880	$71 \pm 2$	75	$14 \pm 4$	450	$39 \pm 4$	480	$74 \pm 6$
1700	$100 \pm \text{nv}$	78	$20 \pm 4$			999	$32 \pm 6$
		105	$30 \pm 5$			1310	$45 \pm 7$
		117	$29 \pm 4$			1426	$20 \pm 10$
		144	$33 \pm 4$				
		175	$54 \pm 5$				
		425	$84 \pm 9$				
		525	$17 \pm 5$				
		625	$17 \pm 5$				
		675	$37 \pm 5$				
		925	$47 \pm 6$				

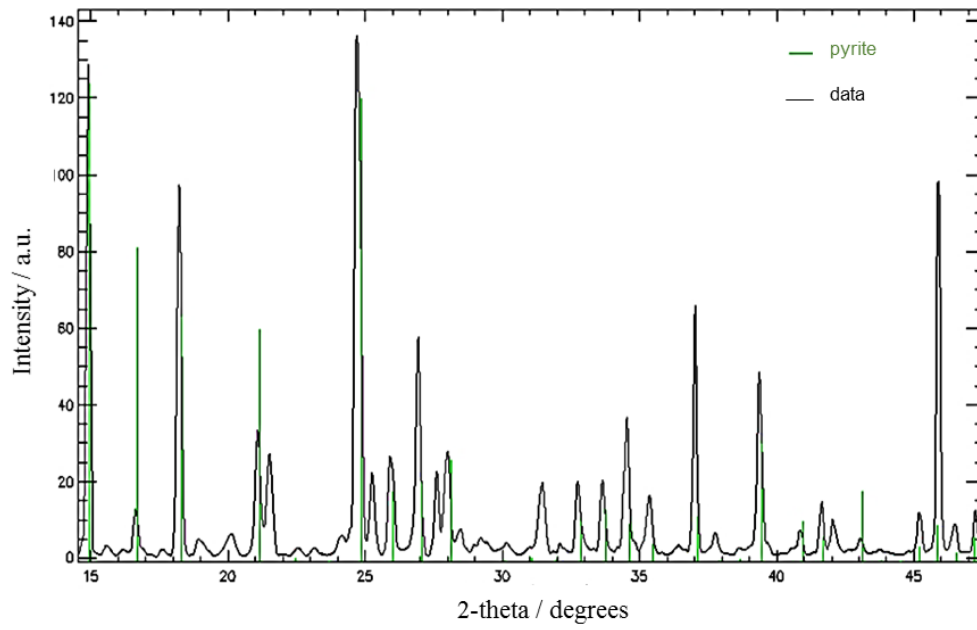


**Figure 11:** Diffractogram taken from the  $\mu$ -XRD mapping shown in Figure 6 for sample Np-3. The green lines represent the reference reflexes of pyrite (PDF 03-065-1211).





# NEPTUNIUM SORPTION ON PURE CLAY MINERALS

## Experimental

### Determination of the correction parameter $A$ for pH measurement in brine solutions

The correction parameter  $A$  for a saline solution can be determined analogously to the following description for a 3 M NaCl solution. Therefore, two stock solutions are needed:

- a) a 3 M NaCl solution
- b) and a solution with 0.02 M HCl and 2.98 M NaCl

Based on  $pH = -\log[H^+]$ , solution b) has a pH of 1.7. The correctness of this preparation can be checked by an additional blank sample containing 0.02 M HCl in MilliQ water. The 1:1 dilution of solution b) with solution a) yields solution c) with pH 2.0. The solutions d) with pH 2.3 and e) with pH 2.6 can be prepared with the same 1:1 dilution. The correction parameter  $A$  is calculated from the measured pH values of the solutions c)–e) using Eq. 5.

## Materials

### Chemicals

All solutions were prepared from “suprapure” grade chemicals obtained from Roth, Merck, Sigma Aldrich or Fluka and MilliQ water (18.2 M $\Omega$ , Synergy<sup>TM</sup> Millipore water system, Millipore GmbH, Germany) .

### *<sup>237</sup>Np and <sup>239</sup>Np stock solutions*

Chemically <sup>237</sup>Np and <sup>239</sup>Np react identically, but exhibit different radioactive properties, since they are both Np isotopes. The half-life of the  $\beta$ -decay of <sup>239</sup>Np with 2.36 d is much shorter than the  $\alpha$ -decay of <sup>237</sup>Np of  $2.14 \times 10^6$  years. The shorter half-life provides enhanced detectability of the decay through  $\gamma$ -ray spectroscopy so that the <sup>239</sup>Np isotope was used in this thesis in batch sorption studies as a tracer ( $10^{-12}$  M), whilst the more commonly used Np concentration of  $8 \times 10^{-6}$  M was adjusted with <sup>237</sup>Np.

For each experiment the <sup>239</sup>Np stock solution was freshly prepared by irradiation of <sup>238</sup>U (30 mg of UO<sub>2</sub>(NO<sub>3</sub>)<sub>2</sub>·H<sub>2</sub>O in 1 mL MilliQ water) at the research reactor TRIGA Mainz (Mark II) for 6 h with a neutron flux of  $7 \times 10^{11}$  n/cm<sup>2</sup> s<sup>-1</sup> (100 kW). The <sup>239</sup>U generated by neutron capture of <sup>238</sup>U decays with a half-life of 23.5 min through  $\beta$ -decay to <sup>239</sup>Np. After one day, more <sup>239</sup>Np had been formed and the hazardous radiation of the short-lived fission products was decreased. <sup>239</sup>Np was separated from remaining U and fission products by anion-exchange chromatography as described by Seibert et al. in [85] and Amayri et al. in [86].

The  $^{237}\text{Np}$  stock solution was prepared by dissolving the  $\text{NpO}_2$  in hot aqua regia (nitric acid and hydrochloric acid in a mixing ratio of 1:3). A further application of anion-exchange chromatography provided the  $^{237}\text{Np}$  stock solution.

Fuming the stock solutions several times with 1 M  $\text{HClO}_4$  oxidizes the contained Np to  $\text{Np(VI)}$ . The residue was taken up with MilliQ water and a spatula of  $\text{NaNO}_2$  was added. This reduces  $\text{Np(VI)}$  to  $\text{Np(V)}$ , which was used in the experiments. Furthermore, the pH of the Np stock solution was adjusted to pH 4 by adding a few  $\mu\text{L}$  of 5 M  $\text{NaOH}$  solution, and the Np concentration was checked by  $\gamma$ -ray spectroscopy.

### ***Illite***

For the batch sorption experiments on conditioned Na-illite, illite du Puy powder was used as base mineral. This clay mineral was obtained from the PSI in Villigen, Switzerland, which was supplied by the French Commissariat à l’Energie Atomique, Service for Waste Storage and Disposal Studies (CEA-Saclay) [87]. The illite powder received was further finely crushed with mortar and pestle to obtain a grain size  $< 63 \mu\text{m}$ . Therefore, sieves with mesh sizes of 250  $\mu\text{m}$ , 150  $\mu\text{m}$ , and 63  $\mu\text{m}$  were used. The following purification procedure was applied in order to increase the homogeneity of the illite used and to obtain a single phase illite system.

### **Purification of illite du Puy**

The purification of the illite du Puy, its transformation into the homoionic Na-form, and the adjustment to the background electrolyte followed the procedure described in [87] of Poinsot, Baeyens, and Bradbury.

#### *Background electrolyte purification*

Impurities can significantly reduce the available sorption sites on the illite surface. Especially with regard to the purification and transformation treatment of illite, the removal of those trace metals from the background electrolyte is very important. This was achieved by using  $\text{Al}_2\text{O}_3$  as scavenger. Therefore, about 7 g of  $\text{Al}_2\text{O}_3$  were filled in a dialysis bag, which was thoroughly washed beforehand with MilliQ water. Then 80 mL of 1 M  $\text{NaCl}$  solution were added and the bag sealed with a small air reservoir for optimal mixing. This bag was put in a 1 L polyethylene container filled with 1 M  $\text{NaCl}$  and placed in an end-over-end rotator for one day.

#### *Transformation into the Na-form*

About 120 g of the illite, which was crushed to a grain size  $< 63 \mu\text{m}$  was added to 2 L of purified 1 M  $\text{NaCl}$  solution, shaken end-over-end for at least 3 hours and allowed to flocculate overnight, so that it was possible to decant the supernatant solution. Three more repetitions of this

procedure are sufficient according to [87] to remove any soluble salts and to transform the illite into the homo-ionic Na-form.

#### *Separation of the Na-illite fraction < 0.5 $\mu\text{m}$*

The 2 L suspension was divided into twelve 250 mL centrifuge bottles and filled up to maximal filling with MilliQ-water. These bottles were shaken end-over-end for about 15 min and afterwards centrifuged for 7 min at 600 g. This speed is sufficient to remove the Na-illite fraction with a size  $> 0.5 \mu\text{m}$  from the suspension. The fraction  $< 0.5 \mu\text{m}$  was decanted into a 5 L container, which contained 1 L of 1 M NaCl solution. The 1 M NaCl was added to stop a further hydrolysis of the clay and to flocculate the clay particles. The 250 mL centrifuge bottles were filled again with MilliQ water, shaken for 15 min, centrifuged and decanted as described before. This procedure was stopped after 15 cycles, when no more clay particles were obtained. The remaining residue was significantly darker in color and discarded. About 30% of the initial illite was obtained in the  $< 0.5 \mu\text{m}$  Na-illite fraction.

#### *Acid treatment*

The possibly occurring hydrolysis of illite due to the washing procedure with MilliQ water can lead to unwanted precipitations of metal hydroxy compounds. These were removed by acidification of the stock solution by adjustment of the pH to 3.5 by adding  $\text{HNO}_3$ . After one hour the suspension was centrifuged for 7 min at 600 g, the supernatant solution decanted and the clay re-suspended in about 450 mL 1 M NaCl solution.

#### *Conditioning of the < 0.5 $\mu\text{m}$ Na-illite fraction to the NaCl concentrations*

The 450 mL were divided into 6 washed dialysis bags (75 mL each), with a little air pocket for better mixing, sealed and placed in 0.5 L polyethylene bottles containing 0.1, 1.0, and 3.0 M NaCl solution. These bottles containing the suspension in the dialysis bags floating in NaCl solution were shaken end-over-end for several hours and the NaCl solution afterwards discarded until the the electric conductivity of the solutions was constant. These values were 10.3 mS/cm for the 0.1 M NaCl solution, 84.7 mS/cm for 1 M NaCl solution, and 198.7 mS/cm for the 3 M NaCl solution.

#### *Determination of the Na-illite concentration*

The solid-to-liquid (S/L) ratios were determined by evaporating three 1 mL samples of the well-stirred suspensions in open snap-on-cap glass vials at 110 °C for at least three days. To subtract the contribution of the background electrolytes, two 1 mL samples of each NaCl concentration were taken and evaporated, too. The final, conditioned Na-illite stock suspension had a concentration of about 90 g/L.

### **Mineralogical composition of illite du Puy and the purified Na-illite**

The initial, untreated illite du Puy was analyzed by the French National Institute for Agronomy Research (INRA), Laboratory for Soil Science by XRD. The results show 74 wt.% of illite and kaolinite and about 20 wt.% calcite (including some siderite) and < 5 wt.% quartz. In contrast, the analysis of the further purified and conditioned Na-illite fraction, showed only reflexes of illite and kaolinite [87].

### ***Kaolinite***

Kaolinite is a 1:1 layer type clay mineral and is contained in many natural soils and clays. The fraction of kaolinite in OPA is about 22 wt.% and thus of high relevance for further considerations of the diffusion of radionuclides in the host rock [20]. The kaolinite used in the experiments is KGa-1b from Washington County, Georgia, USA, which is a well-known reference material for kaolinite and has already been characterized physically and chemically [88-91]. As kaolinite has a very low CEC of 18.3 meq per kg many studies have been performed with the aim of a better understanding of the surface complexation of Np(V) on the clay mineral surface under various conditions [86, 92, 93]. The elemental composition is shown in Table 5. SiO<sub>2</sub> and Al<sub>2</sub>O<sub>3</sub> can be seen as kaolinites key constituents. These are followed by TiO<sub>2</sub> with 1.6 wt.% and other smaller impurities [94].

**Table 5:** Chemical results in wt.% of (crude) KGa-1b measured by XFA [94].

	SiO <sub>2</sub>	Al <sub>2</sub> O <sub>3</sub>	TiO <sub>2</sub>	Fe <sub>2</sub> O <sub>3</sub>	K <sub>2</sub> O	MgO	Na <sub>2</sub> O	CaO	L.o.I
Wt.%	45.2	39.1	1.64	0.21	0.02	0.05	0.04	0.02	13.7

The TiO<sub>2</sub> was determined by XRD as anatase [94]. This phase can be expected to be of further relevance for Np(V) sorption experiments as it has been shown to increase the U(VI) sorption on KGa-1b [95]. In this study, Payne et al. investigated the UO<sub>2</sub><sup>2+</sup> sorption as a function of pH at various S/L-ratios. Transmission electron microscope (TEM) measurements and energy dispersive X-ray spectroscopy (EDS) showed that the uranyl cation was preferentially adsorbed by Ti-rich impurity phases in the form of anatase.

The aim of the present study was to investigate whether the Np(V) sorption on KGa-1b is similarly influenced by the anatase phase as the U(VI) sorption in [95]. For this reason it was checked whether kaolinite KGa-1b can be purified as was done with the illite du Puy. This purification of kaolinite followed closely the procedure described for illite. Therefore a particle size < 0.5 μm can be expected for the purified kaolinite suspension. About 58% of the untreated KGa-1b is < 2 μm, 32% is < 0.5 μm, and the rest < 44 μm [94].

A successful removal of the anatase phase from KGa-1b should show a measurable effect on the Np(V) sorption. Sorption results for the single phase kaolinite could be compared with those of Amayri et al. in [86] for the natural kaolinite KGa-1b.

The average anatase particle size in the batch sorption experiment with Np(V) on pure anatase was  $< 5 \mu\text{m}$ .

### **Batch sorption experiments**

The batch sorption experiments were performed using 10 mL polycarbonate centrifuge tubes (Beckman Coulter, USA). For the experiments with illite the required volume of the concentrated and conditioned Na-illite suspension was calculated for 8 mL final volume. This was filled up to 7.5 mL with the background electrolyte solution. A volume of 0.5 mL was left free for pH adjustments and the addition of the Np stock solution, so that the end volume of 8 mL was achieved just one day before the end of the experiment. The pH was adjusted by adding NaOH and HCl solutions with concentrations up to 5 M in the range of some  $\mu\text{L}$  to the samples using calibrated, appropriate pipettes (Eppendorf, Germany). The pH was measured using a pH electrode (blue line 16 pH, Schott, Germany) connected to a pH meter (Cond pH 720, WTW GmbH, Germany) equipped with a temperature sensor and calibrated with certified buffers (Schott, Germany). An error of about  $\pm 0.05$  was determined for the measurements.

In experiments under ambient air conditions and  $\text{pH} > 7$  the equilibrium concentration of carbonate in solution was calculated with the program Minteq and the corresponding quantities added to the samples in form of concentrated  $\text{NaHCO}_3$  and  $\text{Na}_2\text{CO}_3$  solutions [70]. The calculations with the program Minteq were performed using the specific ion interaction theory (SIT) and a  $\text{CO}_2$  concentration in the ambient air of  $3.8 \times 10^{-4} \text{ atm}$ .

Within three days the sample conditioning and pH adjustment was achieved and the aliquot of the Np stock solution was added. About 100  $\mu\text{L}$  were sufficient to yield a final Np concentration of about  $8 \times 10^{-6} \text{ M}$  in the vials, which was used in the batch and diffusion experiments. In the time between the pH measurements and adjustments the samples were kept suspended by an end-over-end rotator (SB 3, Stuart Scientific, UK). The suspensions were kept in contact with the added radionuclide Np for three days, while the pH was monitored to prevent any pH shifts. To determine the Np concentration in solution and the sorbed Np concentration on the clay surface, the solid phase was separated by centrifugation with an ultra-centrifuge at 108,800 g (30,000 rpm) for 1 hour (Avanti J-30I, Beckman Coulter, USA). Afterwards a sample of 1 mL was taken from the supernatant and measured by  $\gamma$ -ray spectroscopy.

## XRF and XANES measurements

### *Sample preparation*

The samples for the XRF and XANES measurements were prepared from Np(V) diffusion experiments with intact bore cores of OPA with a diameter of about 2.63 cm and a height of about 1.1 cm. For these measurements samples with the size of about 0.5 cm had to be prepared from the OPA bore cores. During preparation it is necessary to know, in each step, exactly which the primary, radioactive side of the bore core is. Therefore, the secondary, inactive sides were marked with an Edding™ pen. Marking the secondary side keeps the pen uncontaminated and the primary side will be indicated immediately for each fragment in the cleaving process. For the cleaving, a stainless steel razor blade was used. The blade was pressed parallel to the bedding of the OPA on the secondary side of the bore core. This keeps the cleaving instrument uncontaminated and the primary side further untouched. The cleaving is eased along the OPA layers, which are indicated by calcite phases. These are visible as small white lines on the surface. The final sample was prepared from a fragment with a very smooth area to reduce any distortions and artefacts in the later measurements. The sample surface with the diffusion profile was not further processed.



**Figure 18:** Preparation of the diffusion profile samples from OPA bore cores (diameter 2.54 cm, height in this case 5 mm). When possible, the bore cores were cleaved (dotted lines) along the bedding as it was eased.

### *Diffusion sample imaging with $\mu$ -XRF*

The Np diffusion profiles were measured by fast  $\mu$ -XRF scans. The excitation X-ray energy of 17.61 keV, which is needed for the Np L<sub>III</sub>-edge, is also sufficient for the fluorescence of further elements contained in OPA, as shown in Figure 19. The Np L $\alpha$  X-ray emission line is, at 13.944 keV, very close to the Sr K $\alpha$  line of 14.165 keV, so that they overlap. As can be seen in this figure, Sr shows high count rates in the investigated samples, as it is contained in OPA with more than 200  $\mu$ g/g OPA. This represents a problem for the measurement of Np in the diffusion profiles by  $\mu$ -XRF. The ROI for Np L $\alpha$  intensity is in Figure 19 marked red and is clearly located on the Sr K $\alpha$  line.

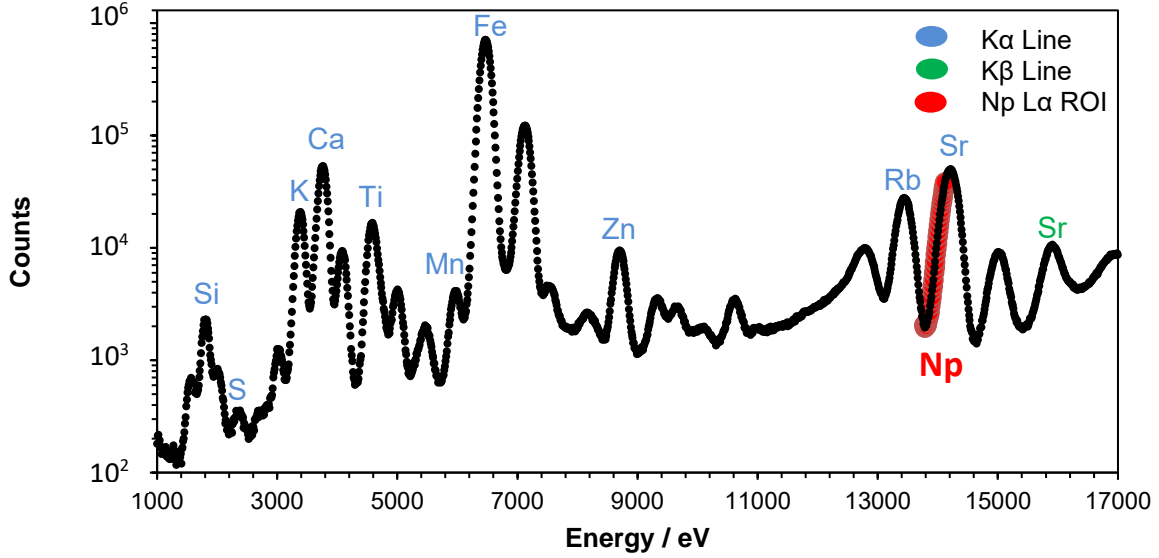


**Figure 19:** X-ray fluorescence spectrum of the elements contained in OPA. Labelled are the recorded ROIs. Marked in red, is the ROI of the Np L $\alpha$  fluorescence, which is located on the K $\alpha$  Line of Sr.

As Sr is also excited at an energy slightly below the Np L<sub>III</sub>-edge, it was possible to subtract these pure Sr counts from the Np L $\alpha$  ROI at 17.55 keV from the sum of the fluorescence of both elements in the Np L $\alpha$  ROI at 17.62 keV to yield the pure Np counts (eq 9, Figure 20). This chemical imaging approach is also referred to as absorption edge difference or absorption edge contrast imaging [35, 96, 97].

$$I(Np) = I(Np \text{ L}\alpha \text{ ROI})_{17.62 \text{ keV}} - I(Np \text{ L}\alpha \text{ ROI})_{17.55 \text{ keV}} \quad (9)$$

Another approach could have been a normalization of the counts of the Np L $\alpha$  ROI to the Sr K $\beta$  ROI as in Eq. 10, but the results were unsatisfactory, due to a too high Sr heterogeneity in some mineral phases.

$$I(Np_{norm}) = \frac{I(Np \text{ L}\alpha \text{ ROI})}{I(Sr \text{ K}\beta \text{ ROI})} \quad (10)$$



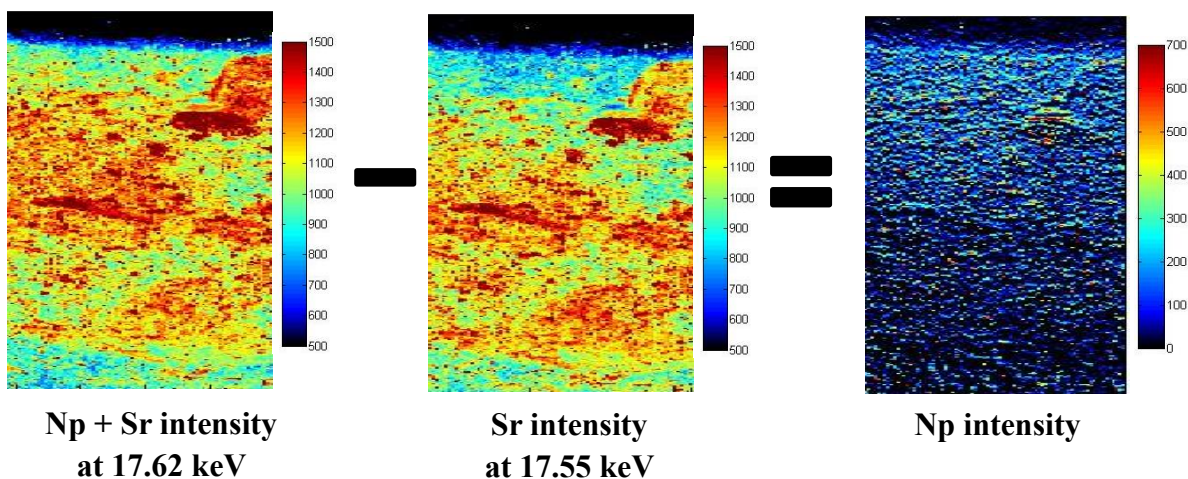


**Figure 20:** Visualization of the calculation of the Np intensities by subtraction of scans with an excitation energy below the Np L<sub>III</sub>-edge (17.55 keV) of those above the Np L<sub>III</sub>-edge (17.62 keV) of the same area (step size 10 μm).

### ***Np XANES measurements***

The XANES measurements used the same experimental setup as shown in Figure 14, which means that the XANES data was collected in the fluorescence mode. Furthermore, the same energy ROI as in the XRF measurements was used to detect the Np fluorescence caused by the X-ray absorption at the Np L<sub>III</sub>-edge. The fluorescence was dead-time corrected by an SLS in-house java applet code and the XANES spectra further processed with the program ATHENA for background removal and normalization of the spectra. Further details can be found in the related manuscript.

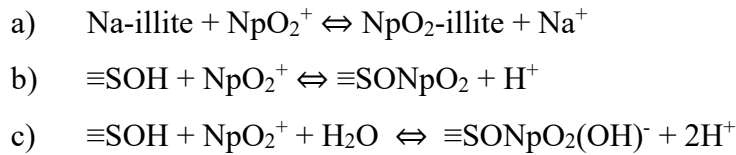
### **Sorption modeling**

The sorption modeling of Np(V) on Na-illite used the cation exchange capacity (CEC) and specific surface area values shown in Table 6. The specific surface area of the conditioned Na-illite was determined by adsorption of ethylene glycol monoethyl ether (EGME) and for OPA with the N<sub>2</sub>-BET method.

**Table 6:** Cation exchange capacity (CEC) and specific surface area of conditioned Na-illite and OPA.

<b>Mineral</b>	<b>CEC / meq/kg</b>	<b>Specific surface area / m<sup>2</sup>/g</b>
Conditioned Na-illite [87]	0.13	129
OPA [98]	0.10	41

The following reactions a) to c) of Np(V) with Na-illite were assumed. Reaction a) shows the cation exchange reaction und reaction b) and c) reactions with strong sorption sites of Na-illite. The modeling was done using the program Visual Minteq applying the Davies theory for ion activity correction and the thermodynamic data base of the program [70].



### Investigation of diffusion experiments with imaging plates

In this work, imaging plates (IPs) were used for the investigation of diffusion experiments. Besides the capability study of a diffusion profile measurement, this system was used to prove the homogenous distribution of activity on the primary site of the bore cores and to look for possible cracks in the bore core after the diffusion experiment. Figure 21 shows three different measuring arrangements, which have been tested for this purpose.

- Small fragments of bore cores from diffusion experiments were placed in a sample holder made of a Plexiglas plate with boreholes in which the samples were laid. The idea of this concept was to avoid a contamination by direct contact between samples and the IPs, so that the IP could be reused.
- A sharper picture was achieved by placing the samples directly on the IP. Therefore, the IP was covered with Mylar foil, which was disposed of afterwards.
- The IPs were covered with Mylar foil and wrapped around the cylindrical bore cores to inspect their sides, i.e. the clay/steel interfaces. This was done to test for leakage in case of a failed diffusion experiment.

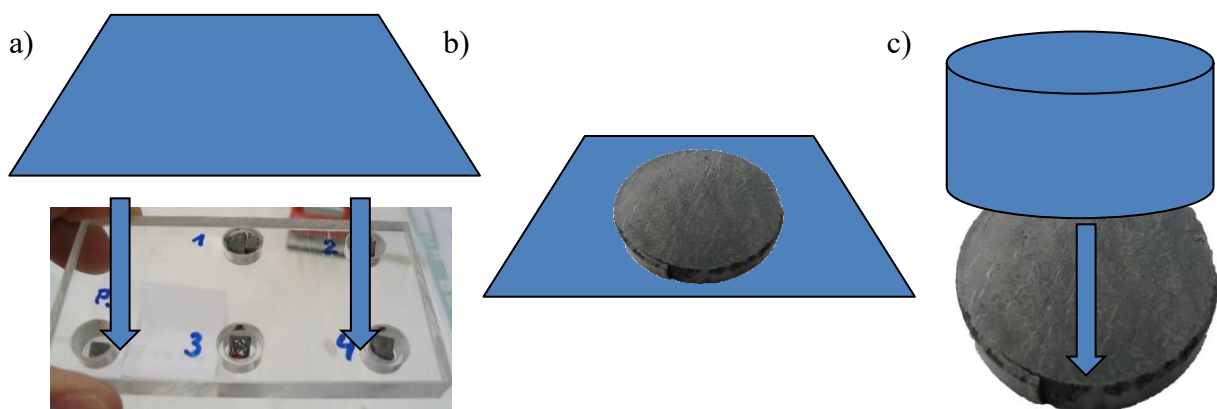


**Figure 21:** Measuring arrangements with a) several radioactive bore core fragments set in boreholes in a Plexiglas plate, which was subsequently covered with an IP, b) a bore core on an IP, and c) an IP wrapped around a bore core to investigate the clay/steel cylinder interface.

The sample preparation for the  $^{237}\text{Np}$  diffusion profile measurements is shown in Figure 22. This was done similarly to the described sample preparation for the XRF/XANES measurements, with cleaving along the bedding. Nevertheless, an attempt was made to get as many thin cleavage products for this investigation as possible without losing the integrity of the fragments. Their, mostly rough, surfaces were not further processed in order to keep the authenticity of the diffusion profiles.



**Figure 22:** Preparation of diffusion profile samples for IP measurement from diffusion of  $8 \times 10^{-6}$  M Np into OPA. The dotted line indicates the cleave locations, the red line the interface between the bore core and the Np solution of the primary reservoir.

Different measuring arrangements for the diffusion profile investigation with IPs were tested. The spherical radiation of the activity in the samples in connection with the three-dimensional position on the IP caused a blurredness of the images and made the determination of the solid/liquid interfaces difficult. However, in view of diffusion profiles in the single digit mm range, this is very important. Therefore, different shieldings and methods were tested, to get a sharper sample image and to enhance the retrievability of the interfaces. Placing the samples next to each other was the most suitable method. The samples were just laid side by side on an IP, as shown in Figure 23 and Figure 31. As the interfaces stayed perfectly sharp on both sides after the cleaving, they could be placed directly next to each other. Neighboring cleavage products were laid together in pairs, with the radioactive interfaces in touch with each other's and the inactive ones only in touch with the inactive ones.

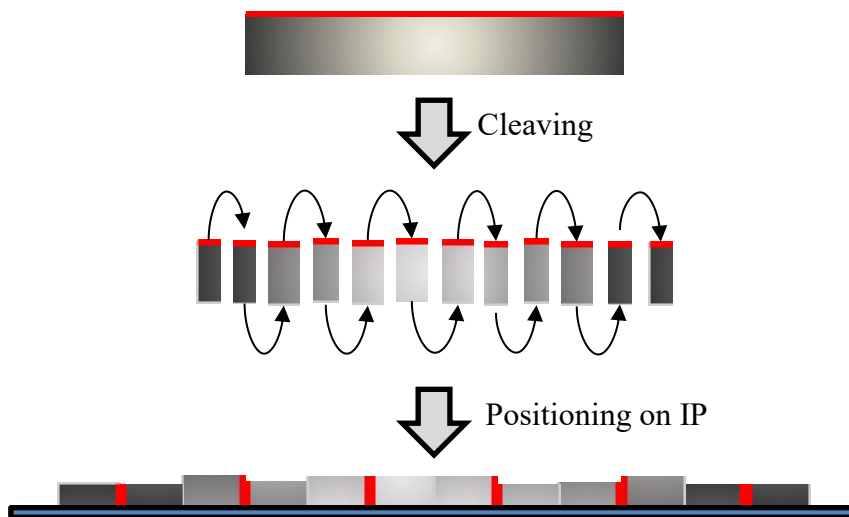


**Figure 23:** Diffusion profile positioning on the IP. The red lines indicate the radioactive interfaces.

All images obtained from the IPs were analyzed with the FLA-5000 Imaging System of FUJIFILM Life Science, with a maximum resolution of 25  $\mu\text{m}$ . Further image processing was done with the program ImageJ 1.48v [99].

## RESULTS

The results section is divided into two parts. The first is about the Np(V) sorption on pure mineral phases and the second is about the investigations of diffusion experiments with imaging plates (IPs).

### **Np(V) sorption on pure mineral phases**

Sorption investigations on pure clay mineral phases are especially needed to enhance the understanding of the Np(V) sorption on heterogeneous and complex natural clay minerals like OPA.

Sorption experiments in different NaCl solutions with Np(V) on the pure clay mineral Na-illite were performed to further investigate the Np(V) sorption on clay minerals in high saline background electrolyte solutions. Furthermore, it was the aim to model the results using the program Minteq based on the 2SPNE SC/CE sorption model [70].

For the common reference mineral kaolinite KGa-1b a purification procedure was tested. The aim was to separate the contained impurity phase of TiO<sub>2</sub> (anatase). Payne et al. showed that even 1–2 wt.% anatase in KGa-1b is very important for the total U(VI) uptake [95]. Furthermore, for a valuation of the general relevance of anatase the Np(V) uptake by TiO<sub>2</sub> was investigated by an additional batch sorption study.

### ***Np(V) sorption on Na-illite***

This investigation started with a sorption isotherm of Np(V) on Na-illite in NaCl solutions (with 0.1, 1.0, and 2.6 M) at pH 7.6, which is the pH of the synthetic OPA pore water (OPA PW). It was the aim to facilitate the comparison with results of related Np(V) sorption experiments on OPA [100]. In Figure 24 log  $K_d$  values are plotted for the sorption of  $8 \times 10^{-6}$  M Np(V) on Na-illite prepared under ambient air conditions. The applied S/L ratios were in the range of 2 to 20 g/L. From the results on average, a log  $K_d$  of about 1.65 (with  $K_d$  in L/kg) was obtained. The influence of the NaCl salinity on the Np(V) sorption on Na-illite is negligible, as the results are similar for all three ionic strengths. Similar results were obtained for the influence of the NaCl concentration on the sorption of Np(V) on OPA [100]. However, note that with a log  $K_d$  of 1.65 (with  $K_d$  in L/kg) the sorption on Na-illite is significantly lower than the sorption of Np(V) on OPA in NaCl solutions with a log  $K_d$  of 2 (if  $K_d$  determined in L/kg) [100].

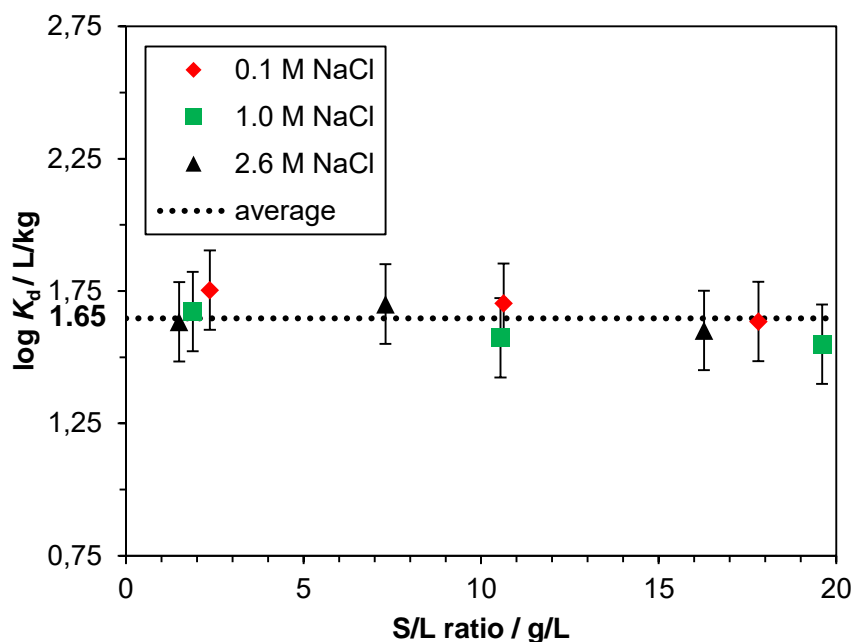


**Figure 24:** Sorption isotherm for the sorption of  $8 \times 10^{-6}$  M Np(V) on Na-illite in 0.1, 1.0, and 2.6 M NaCl solution at pH 7.6 under ambient air conditions.

Figure 25 shows the results for the sorption of  $8 \times 10^{-6}$  M Np(V) on Na-illite ( $S/L \sim 4$  g/L) prepared under ambient air conditions in 0.1 and 3.0 M NaCl solution in the pH range from pH 4 to 9. The results from sorption modeling for the experiment in 0.1 M NaCl solution is shown as a black curve. The related model parameters are presented in Table 7 and Table 6 for further specifications about Na-illite.

**Table 7:** Surface complexation constants for the sorption of Np(V) on the strong sorption sites of Na-illite and the cation exchange ( $I = 0.1$  M NaCl).

reaction	log $K$	log $K$ [101]
$\equiv\text{SOH} + \text{NpO}_2^+ \leftrightarrow \equiv\text{SONpO}_2 + \text{H}^+$	-2.0	-2.0
$\equiv\text{SOH} + \text{NpO}_2^+ + \text{H}_2\text{O} \leftrightarrow \equiv\text{SONpO}_2(\text{OH})^- + 2\text{H}^+$	-10.0	-10.3
$\text{Na-illite} + \text{NpO}_2^+ \leftrightarrow \text{NpO}_2\text{-illite} + \text{Na}^+$	0	0

Figure 25 presents, additionally, the data for the sorption experiment of Np(V) on Na-illite in 0.1 M NaClO<sub>4</sub> solution. This experiment by Gorgeon was performed under similar conditions ( $1.1 \times 10^{-6}$  M Np(V),  $S/L \sim 9$  g/L), except for the much lower carbonate concentration in solution and the anion of the background electrolyte [101]. Gorgeon determined the carbonate concentration to  $\sim 10^{-5}$  M, which is negligibly low. As one can see, the complexation constants

in Table 7 are similar to those of Gorgeon in [101] and therefore in line with further literature [61].

The  $\log K_d$  values presented are, up to pH 8, in a similar range to those of Gorgeon. As for the sorption isotherm experiment the effect of NaCl salinity on the Np(V) sorption is negligible. As shown in the modeling curve below, the sorption falls above pH 8.5, due to the higher Np(V) carbonate complexation. This trend is consistent with the sorption data of the present work. In contrast, Gorgeon's data shows further increasing sorption, due to the very low carbonate concentration.

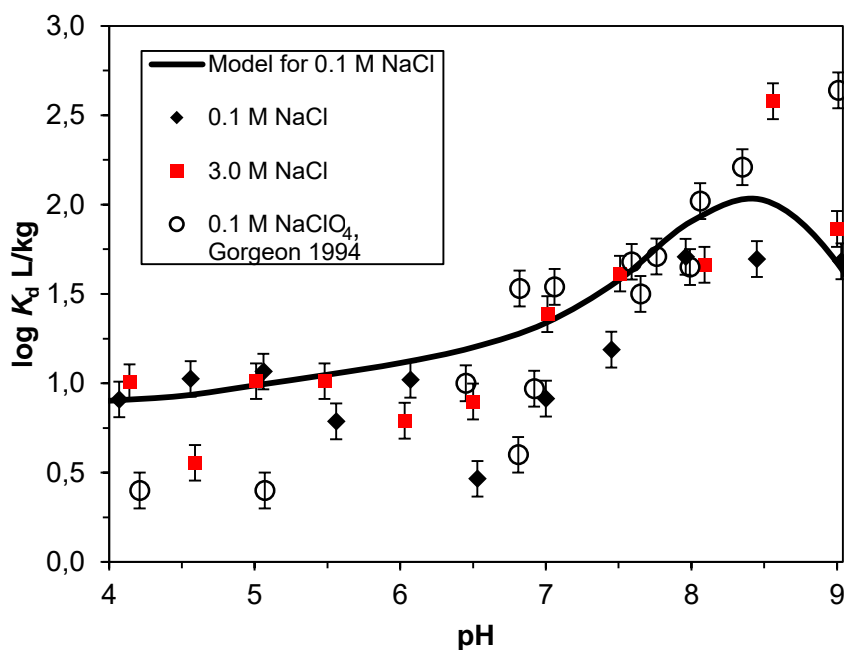


**Figure 25:** Plotted  $\log K_d$  values (with  $K_d$  in L/kg) of the sorption of  $8 \times 10^{-6}$  M Np(V) on  $\sim 4$  g/L Na-illite in 0.1 and 3.0 M NaCl solution under ambient air conditions, together with data of Gorgeon for  $1.1 \times 10^{-6}$  M Np(V) on  $\sim 9$  g/L Na-illite in 0.1 M NaClO<sub>4</sub> solution [101].

Marsac et al. studied in [102] the sorption of Np(V) on Na-illite under inert gas conditions for different Np concentrations and depending on the pH. They found stronger discrepancies between their results and those of Gorgeon. The  $\log K_d$  values in [102] are increased by one log unit. This behavior was explained by a partial reduction of Np(V) and the formation of a stable Np(IV) surface species, due to the lower redox potential of the oxygen-free conditions. Another explanation might derive from differences in the purification process, not described in detail by Marsac et al.

### ***Sorption of Np(V) on natural and purified KGa-1b***

The success of the purification process of the kaolinite KGa-1b was investigated by XRF analysis and Np(V) sorption studies.

The results of the pH dependent batch sorption experiments with Np(V) under ambient air conditions with the treated and untreated KGa-1b clay mineral for the pH range 6–10 are shown in Figure 26. The dotted line represents sorption values < 5%. Below pH 7 a low Np sorption can be seen in both experiments. In the acidic pH range, cation exchange is the dominating process, which is particularly weak for kaolinite. Above pH 7.5 the sorption increases until about pH 8.5, so that the sorption edge is achieved in both experiments at about pH 8. The strong drop of the  $\log K_d$  above pH 9 derives from ambient air conditions and is related to the carbonate complexation of Np(V). This leads for both the treated and untreated kaolinite to a maximum between pH 8.5 and 9 with a  $\log K_d$  of about 2.7 ( $K_d$  in L/kg), which is similar to other studies [86, 92, 93]. Hence, it can be concluded that the purification treatment of the kaolinite was without relevant impact for the Np(V) sorption.

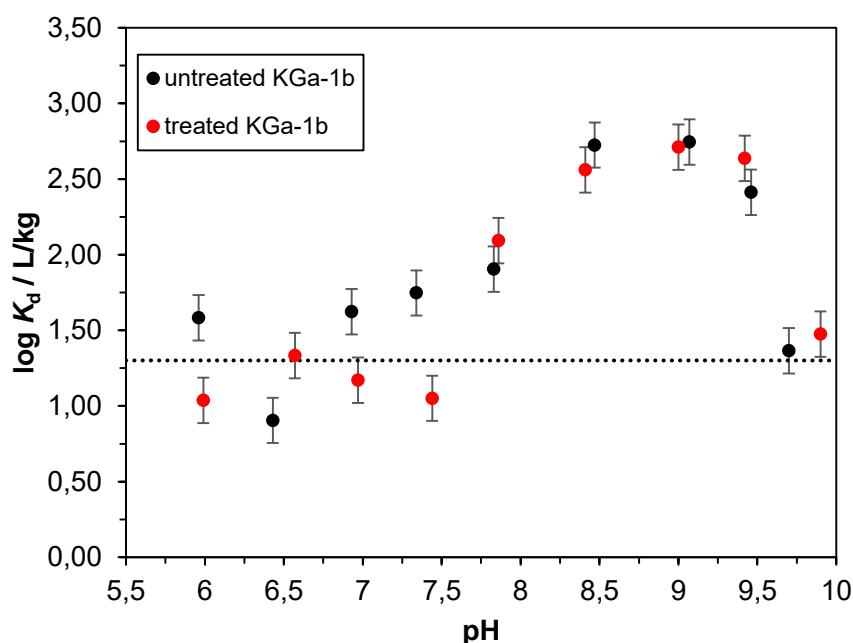


**Figure 26:** Log  $K_d$  values ( $K_d$  in L/kg) for the sorption of  $8 \times 10^{-6}$  M Np(V) on untreated KGa-1b (4 g/L) and treated KGa-1b ( $\sim 2.5$  g/L) in 0.1 M NaClO<sub>4</sub> solution under ambient air conditions. The dotted line represents sorption below 5%.

The treated and untreated KGa-1b powders were analyzed by XRF to validate the success of the purification. The results of the XRF analysis are shown in Table 8. No significant changes in the TiO<sub>2</sub> fraction can be observed. Even though the treated kaolinite contains a factor of



about 10 less SO<sub>3</sub>, this seems not to be of relevance, as the initial fraction is, at 0.013 wt.%, too low to be further significant.

**Table 8:** Chemical composition of treated/untreated kaolinite KGa-1b determined by XRF analysis in wt.%.

KGa-1b	SiO <sub>2</sub>	Al <sub>2</sub> O <sub>3</sub>	TiO <sub>2</sub>	Fe <sub>2</sub> O <sub>3</sub>	P <sub>2</sub> O <sub>5</sub>	CaO	K <sub>2</sub> O	Na <sub>2</sub> O	Cr <sub>2</sub> O <sub>3</sub>	NiO	SO <sub>3</sub>
Untreated	44.87	39.08	1.64	0.23	0.03	0.04	0.02	0	0.0171	0.0016	0.013
Treated	44.53	38.96	1.72	0.23	0.04	0.02	0.02	0.13	0.0172	0.0018	0.001

### ***Relevance of anatase in KGa-1b with regard to Np(V)***

In order to ascertain the influence of the anatase phase in KGa-1b on the investigated Np(V) sorption, three samples were prepared in 0.1 M NaCl solution to study the sorption of Np(V) on anatase depending on the S/L-ratio. KGa-1b contains about 1.7 wt.% anatase. This means that samples with 4 g/L kaolinite might contain about 0.07 g/L anatase. As no literature data of the Np(V) sorption on anatase was available, the intention was to investigate the sorption on a logarithmic scale from 0.02, 0.2, and 2 g/L at pH 8 in 50 mL centrifuge tubes, so that 1 mg, 10 mg, and 100 mg anatase could be weighed in.

The results are displayed in Figure 27. The sample with 2 g/L showed 90% sorption of the initial  $8 \times 10^{-6}$  M Np(V), which leads to a log  $K_d$  of 3.81 (with  $K_d$  in L/kg). This is almost 2 log units more than determined for the sorption of Np(V) on KGa-1b with a log  $K_d$  of about 2 (with  $K_d$  in L/kg), as it was shown above in Figure 26. For the sample with 0.2 g/L a log  $K_d$  of 2.92 was determined, but is flawed by a much higher margin of error, while the sorption of the sample with the lowest anatase concentration was not determinable.

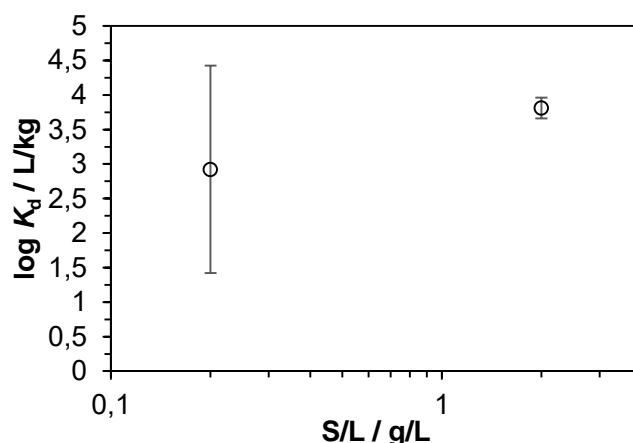


**Figure 27:** Log  $K_d$  values for the sorption of  $8 \times 10^{-6}$  M Np(V) on 0.2 and 2 g/L anatase at pH 8 under ambient air conditions in 0.1 M NaCl solution. The sorption for the sample with 0.02 g/L was below the detection limit.

Nevertheless, these results mean, even for low wt.% anatase, a strong effect on the Np(V) sorption and might be also relevant for other metals at low concentrations. Furthermore, this strong uptake is comparable to the results of the investigation of the sorption of U(VI) on KGa-1b, as described in [95]. This study showed, by application of an EDS/TEM examination, that most of the sorbed uranyl cations were found on the surfaces of phases of anatase. Comparable results can therefore be expected for the sorption of the neptunyl ion on KGa-1b. Both actinyl ions show a similar sorption and diffusion behavior in studies with OPA PW as background electrolyte [55, 72, 103], even though this further depends, for U(VI), on the formation of the complex  $\text{Ca}_2\text{UO}_2(\text{CO}_2)_{3(\text{aq})}$ . Otherwise, U(VI) sorption should be stronger [55, 104].

The relevance of the above-mentioned sorption results should be demonstrated more clearly next. If one assumes that the total Np(V) sorption in the above-mentioned experiment in Figure 26 with 4 g/L KGa-1b occurs on the anatase surface the theoretical S/L-ratio would be 65.4 mg/L (1.636 wt.% anatase in 4 g/L, see Table 8). This S/L-ratio changes the log  $K_d$  of about 2.0 (with  $K_d$  in L/kg) at pH 8 (Figure 26) into a log  $K_d$  of about 3.8, as shown in Table 9. This is identical to the determined log  $K_d$  of 3.81 in the above-mentioned batch experiment with 2 g/L anatase at pH 8.

**Table 9:** Sorption of  $8 \times 10^{-6}$  M Np(V) at pH 8 (see Figure 26) with regard to the total amount of KGa-1b (left column) or only the fraction of contained anatase in KGa-1b (1.636 wt.%, right column).

	Np(V) sorption on KGa-1b	Np(V) sorption on anatase*
S/L /g/L	4.0	0.0654
log $K_d$ / L/kg	2	3.8

\*This assumes no Np(V) sorption on the kaolinite phase of KGa-1b.

The sorption experiments with the kaolinite KGa-1b and anatase indicate a limited applicability of kaolinite KGa-1b and kaolinite from Georgia, USA, in general as a reference mineral for Np(V) sorption studies, or trace metals sorption studies, which is supported by the study of Payne et al. in [95]. Any further “bottom-up” approaches for the sorption of Np(V) on heterogenic clay minerals should also consider minerals with wt.% in the single digit range like  $\text{TiO}_2$  as possibly relevant.

$\text{TiO}_2$  is contained in OPA (BHE-241) with 0.9 wt.% ([105]) in a non-negligible amount. Multiplication of this percentage with the above-mentioned log  $K_d$  of 3.81 ( $K_d = 6481$  L/kg) yields a log  $K_d$  value of 1.76 (with  $K_d$  in L/kg) for the single phase of anatase. This is already

near to the log  $K_d$  value of 2.12 ( $K_d$  in L/kg) determined by Fröhlich et al. for the sorption of  $9 \times 10^{-6}$  M Np(V) in 0.1 M NaClO<sub>4</sub> on OPA at pH 7.8, which is near to pH 8 of the batch experiment with anatase. However, the sorption values for Np(V) on kaolinite and illite at pH 8 can also be taken into consideration for this comparison. One can assume 22 wt.% kaolinite and 44 wt.% illite for this calculation. The related values from this work are shown in Table 10. The log  $K_d$  value of 1.91 for illite is taken from the modeling curve in Figure 24. The resulting  $K_d$  of this bottom-up approach for the sorption of Np(V) on OPA can be calculated with Eq. 11

$$K_d(OPA) = \sum_i CF_i \cdot K_{d,i} \quad (11)$$

with  $CF_i$  as conversion factor, which is related to the wt.% of the respective mineral [60].

As shown in Table 10, this results in sum in a log  $K_d$  of 2.06, which is closer to the log  $K_d$  of 2.33 determined by Fröhlich et al. for Np(V) on OPA in 0.1 M NaClO<sub>4</sub>, even though it is still lower. Without anatase this calculation yields a log  $K_d$  of 1.76 (with  $K_d$  in L/kg). This shows on the one side the high relevance of this mineral, but on the other side it shows that this approach is still not sufficient. For more precise predictions and calculations, it is surely important to investigate the influence of the mineral anatase more intensively. This involves batch series dependent on the S/L-ratio and in a wide range of pH and further background electrolytes and salinities.

**Table 10:**  $K_d$  values and conversion factors  $CF_i$  used for the calculation of the bottom-up approach for the uptake of Np(V) on OPA. Furthermore, the related literature value and the most important experimental details are given.

mineral	$CF_i$	$K_{d,i}$	log $K_{d,i}$	pH	c(Np) / mol/L
Anatase*	0.009	6481	3.81	8	$8 \times 10^{-6}$
Kaolinite**	0.22	100	2.0	8	$8 \times 10^{-6}$
Illite*	0.44	81	1.91	8	$8 \times 10^{-6}$
$\sum_{OPA}$ (eq 10)	0.67	116	2.06	-	-
OPA* [83]	-	214	2.33	7.8	$9 \times 10^{-6}$

\*in 0.1 M NaCl    \*\* in 0.1 M NaClO<sub>4</sub>

## Diffusion experiment investigations with IPs

### *<sup>237</sup>Np activity leakage visualization*

In contrast to other diffusion experiments performed, diffusion cell 28 had a leakage of activity into the secondary reservoir. This should be excluded under the specific experimental conditions and was therefore further investigated with IPs. A short description of the diffusion experiment of cell 28 is given in Table 11.

**Table 11:** Short description of the diffusion experiment of cell 28.

Running time	Np concentration / BGE	Bore core diameter	Height	OPA bedding
33 days	$8 \times 10^{-6}$ M / OPA PW	2.54 cm	1.1 cm	parallel

Figure 28 clearly shows Np activity on the primary and the secondary sites, which are the solid/liquid interfaces. Spot “a” indicates an area on the secondary side with slightly increased activity and was therefore suspected as a potential leakage location. Figure 29 shows the 360° image of the side of the bore, which was without direct contact to the reservoirs. As one can see, the suspected leakage range was positioned in the middle and the primary side at the bottom of the IP.

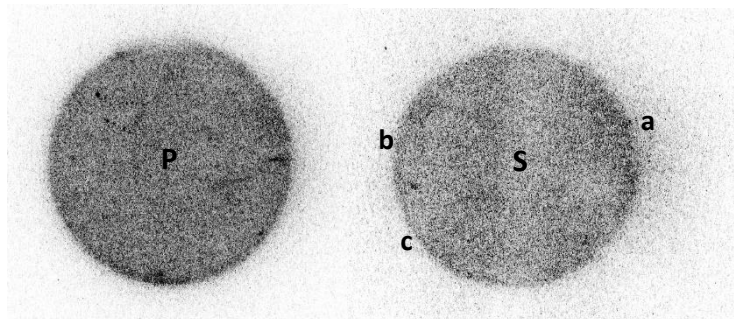


**Figure 28:** Results of the IP measurement (5 h) of the primary (P) and secondary (S) sites of the OPA bore core of cell 28.

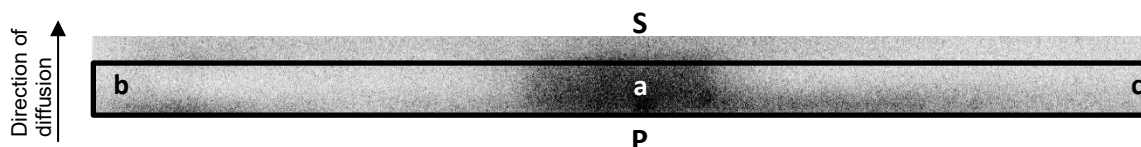


**Figure 29:** 360° image of the outside clay/steel cylinder interface of the bore core (cell 28). This was investigated with an IP wrapped (5 h) around the bore core with the primary site at the bottom side of the IP.

Perhaps, this investigation might help in the future to understand other problems occurring in diffusion experiments. In subsequent experiments related to this work more attention was paid

to the fitting of the bore cores into the steel cylinders. Even though both are prepared with high precision instruments, there was usually a gap with a size  $< 0.1$  mm. In the experiments with an OPA bedding perpendicular to the diffusion this gap was always successfully sealed by the expanding bore core during the conditioning. However, for the diffusion parallel to the bedding a reduction of this gap size seems favorable. Therefore, in subsequent diffusion experiments the fitting was adjusted by using elastic Teflon tape with 0.1 mm thickness.

### ***Comparison between diffusion profiles from IPs and $\mu$ -XRF investigations***

The aim of this investigation was the valuation of diffusion profiles obtained from IP measurements. Beamtime at a synchrotron facility is very valuable and should be planned consciously. Furthermore, the transport of radioactive samples to a synchrotron radiation facility is expensive. In view of safety aspects, this transport must be avoided if there is no compelling necessity. Hence, IPs might be used for a pre-evaluation of radioactive samples, which are intended for measurements at large research infrastructures such as synchrotron facilities.

Subsequent to the measurements described in the manuscript “Speciation study of Np diffusion in Opalinus Clay”, the three bore cores Np-1/2/3 were cleaved (see the experimental section) to obtain the diffusion profile samples for the IP investigation. The results of both the IP and the  $\mu$ -XRF investigation can be therefore taken for a direct comparison.

Figure 30 shows the IP images of the primary sites of the bore cores of the cells Np-1 and Np-2. Both experiments had a starting concentration of  $8 \times 10^{-6}$  M Np(V), the same runtime and were measured simultaneously on the same IP. Np-3 had a longer running time and could not be investigated similarly due to a lack of time in view of the upcoming sample transport. As one can see, the exposure of bore core Np-2 was much stronger. Nevertheless, this is in accordance with the  $\mu$ -XRF results in the above-mentioned manuscript, where the reasons for this difference have been explained in detail. Besides that, a relatively homogenous Np uptake can be seen. Only a few spots with a substantially higher uptake are visible. These hot spots can be derived from the OPA heterogeneity. However, a deeper investigation of these specific mineral phases was not possible.

The sample arrangement for the diffusion profile analysis and the related images are shown in Figure 31. The radioactive, primary (P) sides and secondary (S) sides are marked. In contrast to the quite homogenous diffusion into the bore core for the cells Np-1 and Np-2, the diffusion experiment Np-3 shows a somewhat inconsistent picture of the diffusion. However, no

experimental problems such as clogged circulation of the radioactive solution were identified. Some mineral phases in OPA can be impassable for the Np(V) diffusion, so that this inconsistency might be caused by natural heterogeneity. Nevertheless, the comparison with the  $\mu$ -XRF data is still possible, as the IP diffusion profiles could be obtained from the same part of the bore (Figure 31: Np-3, a) left side) from which the sample for the  $\mu$ -XRF analysis was prepared.

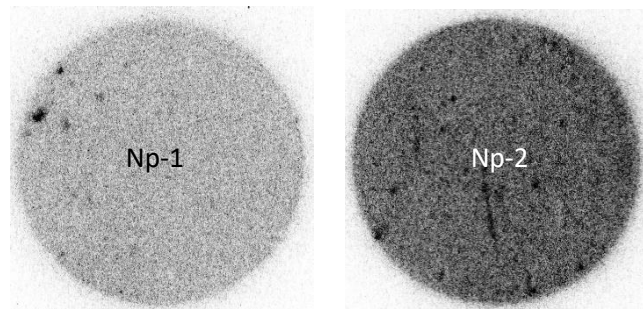


**Figure 30:** Comparison of the IP exposure (72 h) of the primary sites of the cells Np-1 and Np-2.

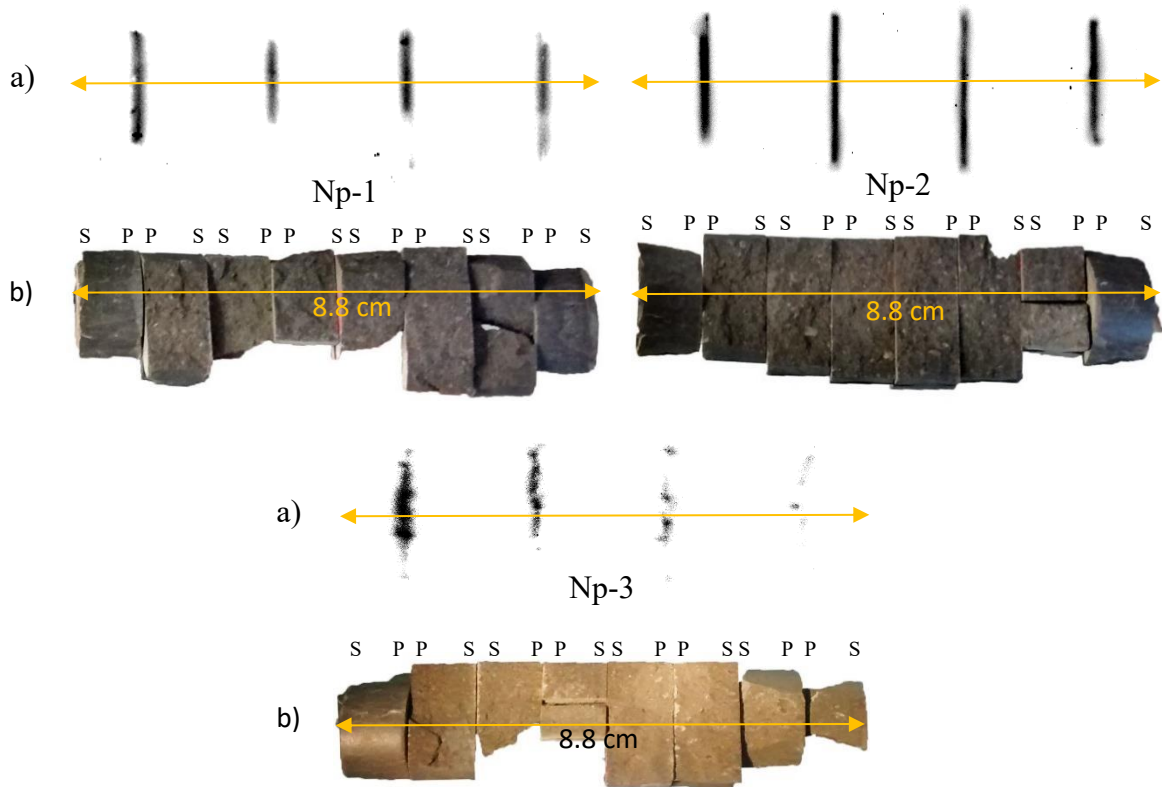


**Figure 31:** Measuring arrangement of the cleaved OPA samples of Np-1/2/3 and the resulting IP image after 72 h of exposure.

The diffusion profiles obtained from the measurements in Figure 31 are shown in Figure 32. The exposure of the IP is displayed in logarithmic units of the measured gray value. The dotted lines are derived from exponential fit functions of the shown background behind the respective

diffusion profile in the sample. The background fit functions are displayed together with their equations in Figure 33. The smaller investigated area of sample Np-3 compared to samples Np-1 and Np-2 results in a larger scattering of the data at the end of the profile of Figure 32. However, this effect is not strong.

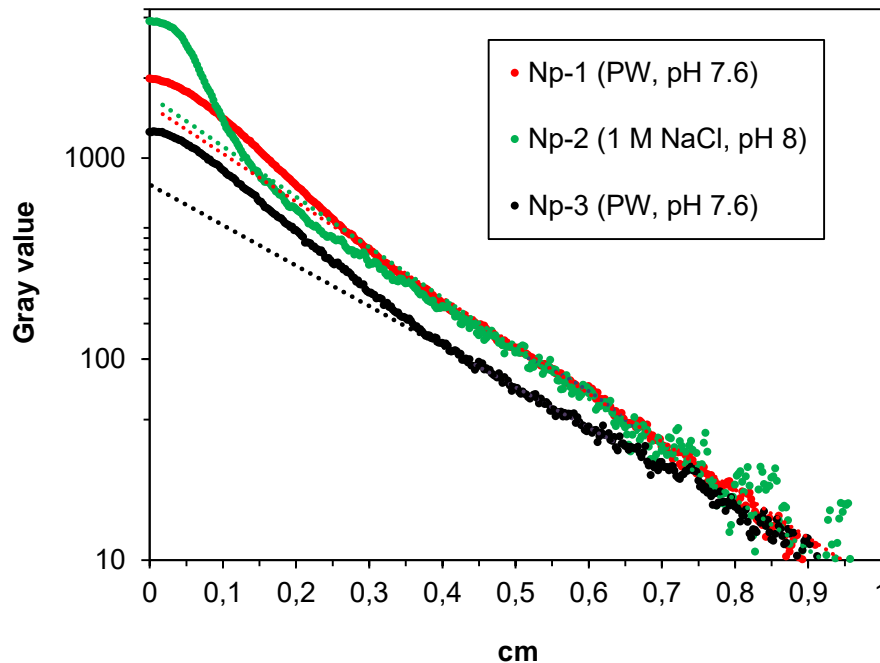


**Figure 32:** Results of the diffusion profile analysis with IPs of the diffusion experiments Np-1/2/3.

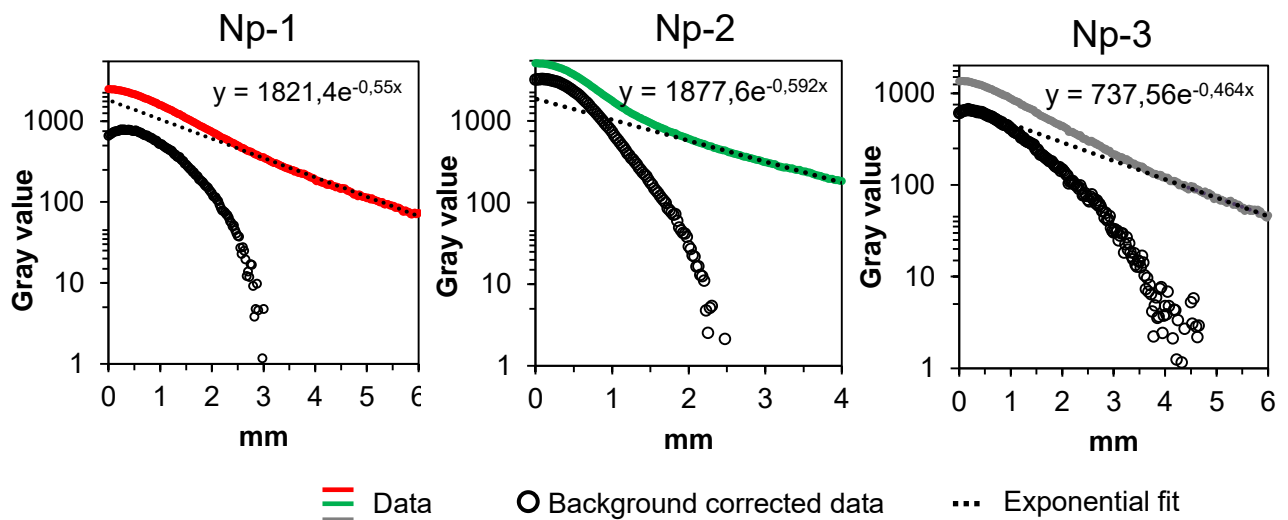


**Figure 33:** The red, green, and grey lines show the diffusion profiles of the cells Np-1/2/3 from IP measurement, the dotted lines indicates the exponential fits of the background and the open circles represent the corrected diffusion profiles, providing the Np diffusion profiles with the final diffusion depth.

The observed exponential dependency of the background can be explained with the absorption of  $\gamma$  rays in matter. The intensity of  $\gamma$  rays from activity in the radioactive interface drops exponential as the  $\gamma$  rays cross the three-dimensional sample.

However, this background subtraction method must be further developed, as the calculated gray values of the diffusion profiles of Np-1 and Np-3 in Figure 33 increase on the first hundred  $\mu\text{m}$ , which cannot be explained logically.

The gray values of the diffusion profiles displayed in Figure 33 were converted for Figure 34 into “Np activity in rock” (in Bq/g). This was done identically as in the related manuscript for the results of the  $\mu\text{-XRF}$  measurements. For reasons of clarity this figure compares the background corrected diffusion profiles from IP measurement with the clearer modelling curves of the  $\mu\text{-XRF}$  data.

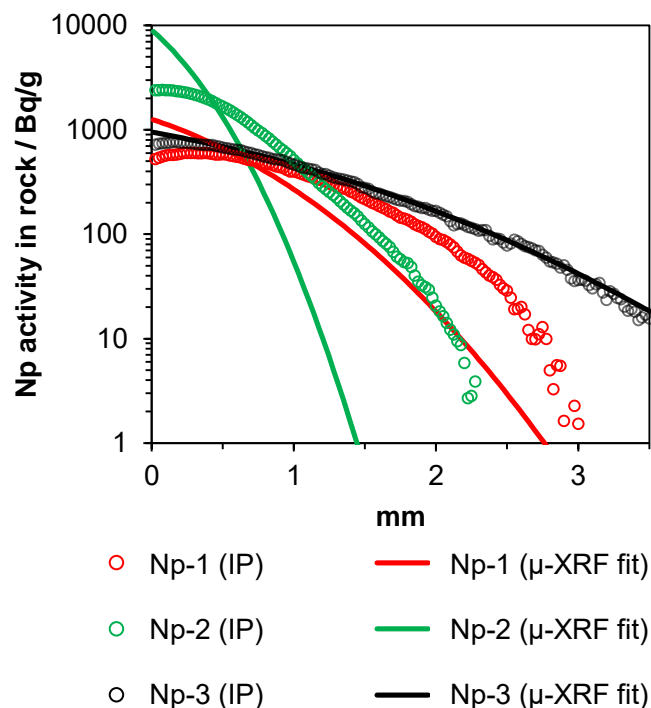


**Figure 34:** Comparison of the results from IP measurements (circles) and from modeling of the  $\mu\text{-XRF}$  data of samples Np-1/2/3.

The comparison in Figure 34 between the results of the Np diffusion modeling of the  $\mu\text{-XRF}$  data and the analysis with IPs shows high concordance in some aspects, but also discrepancies. A high concordance can be seen for sample Np-3. The  $\mu\text{-XRF}$  modeling curve starts exactly with the same initial Np activity at the solid/liquid interface and further follows the profile obtained by the IP. For the other two profiles the diffusion depth seems to be overestimated. This causes lower activities at the solid/liquid interfaces, as the Np amount in the profile must still be equal.



In general, one can see less scattering in the data of the profiles from the IP analysis than in the profiles from  $\mu$ -XRF measurement, which are shown in the manuscript. This is due to the fact that the sample area investigated by IPs was, with several  $\text{cm}^2$ , much larger than those  $\text{mm}^2$  investigated by  $\mu$ -XRF. Furthermore, this method shows a high sensitivity. The profiles cover concentration ranges over more than three magnitudes. Nevertheless, an improved background subtraction method must be developed to stop the overestimation of the diffusion depths.

Despite those unsolved problems, Figure 35 shows the feasibility of the modeling of the Np diffusion for profiles obtained by IPs. Therefore, the diffusion profiles from IP measurement have been modeled identically to the  $\mu$ -XRF diffusion profiles in the manuscript. For the comparison between the  $\mu$ -XRF and IP diffusion profiles analysis the model parameters are given for both methods in Table 12.

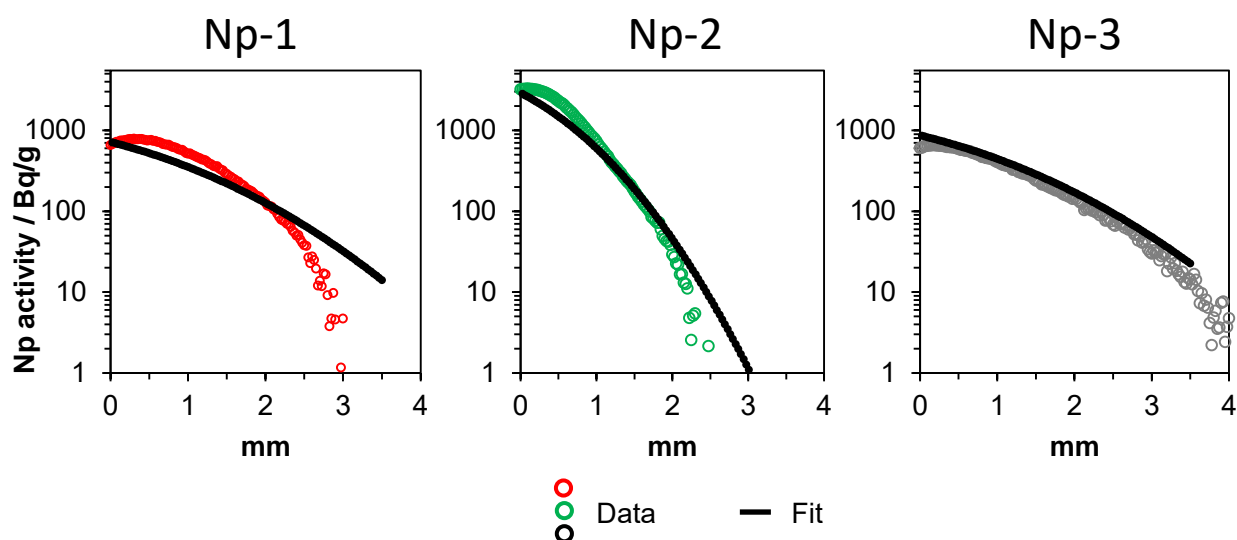


**Figure 35:** Np diffusion profiles from IP measurements with the results from diffusion modeling for the samples Np-1/2/3.

**Table 12:** Results for the diffusion profile modeling obtained from  $\mu$ -XRF and IP analysis.

	$\mu$ -XRF			IP		
	$\log(K_d / \text{L/kg})$	$D_e / 10^{-12} \text{ m}^2/\text{s}$	$\alpha$	$\log(K_d / \text{L/kg})$	$D_e / 10^{-12} \text{ m}^2/\text{s}$	$\alpha$
Np-1	$1.4 \pm 0.1$	$4.4 \pm 4$	$65 \pm 6$	$1.0 \pm 0.1$	$4.0 \pm 2$	$26 \pm 3$
Np-2	$2.6 \pm 0.1$	$12.8 \pm 4$	$862 \pm 78$	$1.8 \pm 0.1$	$7.2 \pm 2$	$144 \pm 14$
Np-3	$1.3 \pm 0.1$	$8.3 \pm 4$	$49 \pm 4$	$1.1 \pm 0.1$	$3.7 \pm 2$	$32 \pm 3$

As already mentioned, the wider diffusion profiles lead to lower values for the Np activity concentration in the profiles. Hence, the resulting  $\log K_d$  values from the modeling are lower than can be expected from the  $\mu$ -XRF analysis. Those values for the distribution coefficients

were higher and comparable to related batch and diffusion experiments. For more details see the manuscript or Wu et al. [72]. Nonetheless, the determined  $D_e$  values from IP measurement are both almost the same and comparable to that of Np-1 in Table 12 as determined for the  $\mu$ -XRF profile.

For the final conclusions on the investigations of diffusion experiments of radionuclides with IPs, it can be stated that these measurements are definitely a helpful tool for monitoring and verification of a failure-free operation of diffusion cells. Especially when the bore core of the diffusion experiment is already partially disassembled and the abrasive peeling method is not further applicable, an investigation with IPs may be appropriate. The big advantage of IPs compared to the abrasive peeling method is that the diffusion profiles can be determined in a non-destructive way, so that they can be further analyzed by other spatially resolved methods. With a view towards of similar investigations in the future, the disappointing results for the cell Np-2 and promising ones for Np-3 could indicate that the quality of the results decreases with decreasing diffusion depths. However, this might also depend on parameters such as the accumulated activity in the sample, the sample height, and, last but not least, an improved background subtraction.

## CONCLUSIONS AND OUTLOOK

As the conclusions of the single manuscripts have already explained in detail before, this chapter aims on the overall conclusion and meaning of the described results related to a deep geological repository in argillaceous rock.

In general, the extensive sorption, diffusion, and speciation studies provide deep insights into the complex migration and retardation of Np(V) in the natural argillaceous rock OPA. The numerous  $K_d$  and  $D_e$  values, depending on pH, electrolyte, salinity and Np concentration, will be adopted into databases to improve the long-time safety assessment calculations.

Based on the temperatures in a deep geological repository for HLW, this work showed that increased temperatures lead to an increase of the effective diffusion of Np(V) in OPA. The related activation energies for the diffusion of Np(V) can therefore improve the safety assessment. Furthermore, reports about an increased sorption of Np(V) on OPA with increased temperatures due to endothermic sorption enthalpy could not be confirmed. This means that sorption is not directly affected by the temperature – at least in NaCl solutions.

The combination of  $\mu$ -XRF measurements with  $\mu$ -XRD and  $\mu$ -XANES showed the influence of OPA heterogeneity on Np(V) diffusion and speciation. This is the first time that diffusion parameters have been obtained for Np(V) by use of synchrotron radiation. The unique combination of those different methods makes it possible to connect the diffusion parameters directly with Np speciation and related redox-active minerals for a single diffusion experiment. The increasing Np(IV)/Np(V) ratio on the first 150  $\mu\text{m}$  behind the solid/liquid interface, due to the different redox conditions inside and outside the bore core, shows the high sensitivity and precision of the performed  $\mu$ -XANES investigation and points out the strong redox sensitivity of Np under environmental conditions. As the redox potential measurement on the inside of solids is hard to manage, Np functions as a redox probe. The average fraction of  $36 \pm 13\%$  Np(IV) in the diffusion profiles points at a relatively constant redox potential. This knowledge might be important for similar OPA diffusion studies performed under ambient air conditions.

Compared to such advanced synchrotron-based techniques the application of IPs, as conducted in a diffusion profile analysis in this work, is almost antiquated. This method points to the early beginnings of the discovery of radioactivity. Nevertheless, the modern application with high-resolution and high sensitive IPs seems promising. It is a non-destructive analysis method, which could open up more opportunities for combined speciation and diffusion studies in

connection with redox-sensitive radionuclides. The general feasibility and value of this method has been shown in this work.

With regard to a HLW repository in argillaceous rock in the region of northern Germany, where higher saline groundwater is expected, this work demonstrated multiple possible effects of these higher salinities. An additional summary of the  $\log K_d$  values from Np(V) diffusion experiments using different saline NaCl solutions in this work is given in Table 13 together with the results of the related batch experiments. The results do not indicate an influence of the NaCl salinity on the sorption of Np(V) on OPA. This does not apply to the Np diffusion in OPA. The decrease of the  $D_e$  with the NaCl concentration was verified and derived to a reduced diffuse double layer porosity, which shows that the influence of high saline ground water on radionuclide diffusion can be complex.

**Table 13:** Results from the different Np(V) diffusion experiments with regard to  $\alpha$ ,  $D_e$ , and  $\log K_d$ . The values in brackets are from the related batch sorption experiments. The abbreviation “AP” behind the first three cell names stands for the applied abrasive peeling method in contrast to the parameter determination by  $\mu$ -XRF.

Cell	Electrolyte	T / °C	$\alpha$	$D_e$ / $10^{-12} \text{ m}^2/\text{s}$	$\log K_d$ / L/kg
Cell 3 (AP)	1 M NaCl	60	$834 \pm 8$	$17.5 \pm 1.8$	$2.5 \pm 0.1$ ( $2.2 \pm 0.1$ at 80 °C)
Cell 1 (AP)	1 M NaCl	24	$742 \pm 9$	$6.9 \pm 1.2$	$2.5 \pm 0.1$ ( $2.0 \pm 0.1$ )
Cell 2 (AP)	3 M NaCl	24	$455 \pm 7$	$2.4 \pm 1.0$	$2.3 \pm 0.1$
Np-2 (XRF)	1 M NaCl	24	$862 \pm 78$	$12.8 \pm 4.0$	$2.6 \pm 0.1$ ( $2.3 \pm 0.1$ )

Sorption studies on single mineral phases are very important to improve the understanding of Np(V) sorption on OPA or other natural argillaceous rocks. Only with detailed knowledge can the radionuclide migration in the host rock be assessed correctly. This was done for the sorption of Np(V) on Na-illite (du Puy) and the kaolinite KGa-1b, as illite and kaolinite are both important mineral phases in OPA. Concerning Na-illite, the influence of NaCl concentration and the pH on the sorption of Np(V) on purified and conditioned Na-illite was further investigated. In addition, the Np(V) sorption study on KGa-1b was tested to separate anatase ( $\text{TiO}_2$ ) impurities from KGa-1b. Even though this failed, it was shown that this phase is very important for the total sorption of Np(V) on KGa-1b under the investigated conditions. The

determined  $\log K_d$  of about 3.8 (with  $K_d$  in L/kg) at pH 8 for Np(V) on anatase is noticeably high. According to the wt.% of anatase contained in KGa-1b this might be, for comparable experimental conditions ( $c(\text{Np(V)})$ , S/L, pH), sufficient to describe the complete sorption of Np(V) on KGa-1b. When considering bottom-up approaches for the sorption of Np(V) on natural clay minerals, it might be appropriate to take the specific fractions of anatase into consideration. This relevance has also been demonstrated for OPA.

## LIST OF ABBREVIATIONS AND TERMS

1:1 clays	Non-swelling clays like kaolinite comprising TO-layers
2:1 clays	Swelling clays like montmorillonite comprising TOT-layers
2SPNE SC/CE model	Two site protolysis non-electrostatic surface complexation and cation-exchange model
$\alpha$	Rock capacity factor
$\varepsilon$	Diffusion accessible porosity
a	year (annus)
A	Activity
An/Actinide	Series of the 15 metallic chemical elements with atomic numbers from 89 to 103, actinium to lawrencium
Anisotropy	The property of being directionally dependent
AkEnd	Arbeitskreis Auswahlverfahren Endlagerstandorte
AtG	Atom Energy Act (Atomenergiegesetz)
Batch	Experimental series in which solely one parameter is varied
BfS	Federal Office for Radiation Protection (Bundesamt für Strahlenschutz)
Bq	Bequerel
CEC	Cation exchange capacity
CF	Conversion factor
$D_e$	Effective diffusion coefficient
DDL	Diffuse double-layer comprising ions attracted to the surface charge via the Coulomb force
DOM	Dissolved organic matter
EDS	Energy dispersive X-ray spectroscopy
$E_h$	Redox potential measured against standard hydrogen electrode (SHE)
ECZ	Effective containment zone
EXAFS	Extended X-ray absorption fine structure
Fission products	Fragments like $^{90}\text{Sr}$ , $^{99}\text{Tc}$ , $^{129}\text{I}$ , and $^{137}\text{Cs}$ produced at the nuclear fission of a larger atomic nuclei like $^{235}\text{U}$ and $^{239}\text{Pu}$

GWd/t	Released energy per mass of nuclear fuel measured as gigawatt-days per metric tonne
HA	Humic acid
HCP	Hardened cement paste
HLW	High-level waste
HTO	Tritiated water
IAEA	International Atomic Energy Agency
ILW	Intermediate-level waste
$I$ (Ionic strength)	$I = \frac{1}{2} \sum_{i=1}^n c_i z_i^2$ , with $c_i$ the molar concentration and $z_i$ the charge number of the ion
IP	Imaging plate
$K_d$	Distribution coefficient
LLW	Low-level waste
LSC	Liquid scintillation counting
M	mol/L
Major actinides	Pu, U
Meq	milli equivalent
MOX	Mixed oxide nuclear fuel, usually comprising $UO_2$ and $PuO_2$
Minor actinides	Np, Am Cm, Bk, Cf
OPA	Opalinus Clay
$pH_{pznpc}$	pH with a zero net proton charge on the mineral surface
PW	Pore water
PSI	Paul Scherrer Institute
Radiotoxicity	The type and energy of rays, absorption in the organism, residence time in the body, etc. influence the degree of radiotoxicity of a radionuclide
ROI	Range of interest
Speciation	Analysis of the elemental species
S/L ratio	Solid-to-liquid ratio of suspensions, commonly in g/L

SLS	Swiss Light Source, PSI, Villigen, Switzerland
SIT	Specific ion interaction theorie
Sv	Sievert (Joule per kg), measure of the health effect of low level ionizing radiation and radiation dose quantities as equivalent dose or effective dose
TD-SDB	Thermodynamic sorption database
tHM	Tonne heavy metal
TOT-layer	Series of two tetrahedral (SiO <sub>2</sub> ) and one octahedral (AlO <sub>6</sub> ) layer (2:1 mineral)
TEM	Transmission electron microscope
X-rays	Electromagnetic waves with energies in the range 5–500 keV between ultraviolet light and $\gamma$ rays
XANES	X-ray absorption near edge structure
XAS	X-ray absorption spectroscopy
XRD	X-ray diffraction
XRF	X-ray fluorescence



## REFERENCES

1. Gompper, K., *Zur Abtrennung langlebiger Radionuklide*. Radioaktivität und Kernenergie. 2001, Karlsruhe: Forschungszentrum Karlsruhe.
2. International Atomic Energy Agency, *Disposal of radioactive waste*. IAEA Safety Standards Series No. SSR-5, 2011.
3. Campbell, D.O. and W.D. Burch, *The chemistry of fuel-reprocessing - present practices, future-trends*. Journal of Radioanalytical and Nuclear Chemistry-Articles, 1990. **142**(1): p. 303-320.
4. Poinssot, C., S. Bourg, and B. Boullis, *Improving the nuclear energy sustainability by decreasing its environmental footprint. Guidelines from life cycle assessment simulations*. Progress in Nuclear Energy, 2016. **92**: p. 234-241.
5. Baldwin, A.G., N.J. Bridges, and J.C. Braley, *Distribution of fission products into tributyl phosphate under applied nuclear fuel recycling conditions*. Industrial & Engineering Chemistry Research, 2016. **55**(51): p. 13114-13119.
6. Ochkin, A.V., *Some problems in reprocessing of fuel spent by modern power reactors*. Theoretical Foundations of Chemical Engineering, 2014. **48**(1): p. 34-38.
7. Takeda, T., *Minor actinides transmutation performance in a fast reactor*. Annals of Nuclear Energy, 2016. **95**: p. 48-53.
8. Lebreton, F., D. Prieur, D. Horlait, T. Delahaye, A. Jankowiak, C. Leorier, F. Jorion, E. Gavilan, and F. Desmouliere, *Recent progress on minor-actinide-bearing oxide fuel fabrication at CEA Marcoule*. Journal of Nuclear Materials, 2013. **438**(1-3): p. 99-107.
9. International Atomic Energy Agency, *Status of minor actinide fuel development*. IAEA Nuclear Energy Series, 2009, Wien: IAEA.
10. Martin, P., M. Pelletier, D. Every, and D. Buckthorpe, *French and United Kingdom experience of high-burnup mixed-oxide fuel in sodium-cooled fast breeder reactors*. Nuclear Technology, 2008. **161**(1): p. 35-44.
11. UK National Nuclear Laboratory, *Minor actinide transmutation*. Position Paper, 2013, Warrington, UK: National Nuclear Laboratory.
12. Kommission Lagerung hoch radioaktiver Abfallstoffe, *Abschlussbericht, Verantwortung für die Zukunft, Ein faires und transparentes Verfahren für die Auswahl eines nationalen Endlagerstandortes*. 2016, Berlin, Germany: Deutscher Bundestag.
13. <http://www.endlager-konrad.de/Konrad/DE/themen/umbau/umbaudauer/umbaudauer.html>. 20.02.2017 14:18 Uhr].

14. Niedersächsisches Ministerium für Umwelt und Klimaschutz, *Statusbericht des Niedersächsischen Ministeriums für Umwelt und Klimaschutz über die Schachtanlage Asse II*. 2008.
15. Chapman, N. and A. Hooper, *The disposal of radioactive wastes underground*. Proceedings of the Geologists Association, 2012. **123**(1): p. 46-63.
16. Anderson, C.-G., *Test manufacturing of copper canisters with cast inserts*. SKB TR-98-09, 1998, Stockholm, Sweden: Swedish Nuclear Fuel and Waste Management Co.
17. Raiko, H., *Disposal canister for spent nuclear fuel - design report*. POSIVA 2005-02, 2005.
18. Kronberg, M., J. Gugala, and K. Haapala, *State-of-the-art and proof-of-concept installations for repository concepts based in crystalline rock*. Mineralogical Magazine, 2015. **79**(6): p. 1665-1673.
19. Keller, S., *Eiszeitliche Rinnensysteme und ihre Bedeutung für die Langzeitsicherheit möglicher Endlagerstandorte mit hochradioaktiven Abfällen in Norddeutschland*. 2009, Hannover, Germany: Bundesanstalt für Geowissenschaften und Rohstoffe (BGR).
20. Nagra, *Projekt Opalinuston - Synthese der geowissenschaftlichen Untersuchungsergebnisse*. Technical Report 02-03, 2002, Wetingen, Switzerland: Nagra.
21. Organisation for Economic Co-operation and Development, *Safety of geological disposal of high-level and long-lived radioactive waste in France - An international peer review of the "Dossier 2005 Argile" concerning disposal in the Callovo-Oxfordian formation*. NEA No. 6178, 2006, Paris, France: OECD.
22. Organisation for Economic Co-operation and Development, *SAFIR 2: Belgian R&D programme on the deep disposal of high-level and long-lived radioactive waste. An International Peer Review*, 2003, Paris, France: OECD.
23. Rohstoffe, B.f.G.u., *Endlagerung radioaktiver Abfälle in tiefen geologischen Formationen Deutschlands – Untersuchung und Bewertung von Regionen mit potenziell geeigneten Wirtsgesteinsformationen*. 2007, Hannover/Berlin, Germany: BGR.
24. Pearson, F.J., *Opalinus Clay experimental water: A1 type*. PSI technical report TM-44-98-07, 1998, Villigen, Switzerland: Paul Scherrer Institut.
25. Brewitz, W., *Eignungsprüfung der Schachtanlage Konrad für die Endlagerung radioaktiver Abfälle: Abschlussbericht (GSF - T 136)*. 1982: GSF.
26. Horseman, S.T., Higgo, J. J. W., Alexander, J., Haarrington, J. F., *Water, gas and solute movement through argillaceous media*. Nuclear Energy Agency Rep. CC-96/1, 1996.

27. Glaus, M.A., B. Baeyens, M.H. Bradbury, A. Jakob, L.R. Van Loon, and A. Yaroshchuk, *Diffusion of  $^{22}\text{Na}$  and  $^{85}\text{Sr}$  in Montmorillonite: Evidence of interlayer diffusion being the dominant pathway at high compaction*. Environmental Science & Technology, 2007. **41**: p. 478-485.
28. Oscarson, D.W., *Surface diffusion: Is it an important transport mechanism in compacted clays?* Clays and Clay Minerals, 1994. **42**(5): p. 534-543.
29. Mauerhofer, E., K. Zhernosekov, and F. Rosch, *Limiting transport properties and hydration numbers of actinyl ions in pure water*. Radiochimica Acta, 2004. **92**(1): p. 5-10.
30. Glaus, M.A., S. Frick, R. Rossé, and L.R.V. Loon, *Comparative study of tracer diffusion of HTO,  $^{22}\text{Na}^+$  and  $^{36}\text{Cl}^-$  in compacted kaolinite, illite and montmorillonite*. Geochimica et Cosmochimica Acta, 2010. **74**(7): p. 1999-2010.
31. Van Loon, L.R., M.A. Glaus, and W. Müller, *Anion exclusion effects in compacted bentonites: Towards a better understanding of anion diffusion*. Applied Geochemistry, 2007. **22**(11): p. 2536-2552.
32. Coppin, F., G. Berger, A. Bauer, S. Castet, and M. Loubet, *Sorption of lanthanides on smectite and kaolinite*. Chemical Geology, 2002. **182**(1): p. 57-68.
33. Motta, M.M. and C.F. Miranda, *Molybdate adsorption on kaolinite, montmorillonite, and illite - constant capacitance modeling*. Soil Science Society of America Journal, 1989. **53**(2): p. 380-385.
34. Brady, P.V., R.T. Cygan, and K.L. Nagy, *Molecular controls on kaolinite surface charge*. Journal of Colloid and Interface Science, 1996. **183**(2): p. 356-364.
35. Huertas, F.J., L. Chou, and R. Wollast, *Mechanism of kaolinite dissolution at room temperature and pressure: Part I. Surface speciation*. Geochimica et Cosmochimica Acta, 1998. **62**(3): p. 417-431.
36. Bradbury, M.H. and B. Baeyens, *A mechanistic description of Ni and Zn sorption on Na-montmorillonite: Part II: modelling*. Journal of Contaminant Hydrology, 1997. **27**: p. 223-248.
37. Wanner, H., Y. Albinsson, O. Karnland, E. Wieland, P. Wersin, and L. Charlet, *The acid-base chemistry of montmorillonite*. Radiochimica Acta, 1994. **66-7**: p. 157-162.
38. Avena, M.J. and C.P. De Pauli, *Proton adsorption and electrokinetics of an Argentinean montmorillonite*. Journal of Colloid and Interface Science, 1998. **202**(1): p. 195-204.
39. Van Loon, L.R. and J.M. Soler, *Diffusion of HTO,  $^{36}\text{Cl}^-$ ,  $^{125}\text{I}$  and  $^{22}\text{Na}^+$  in Opalinus Clay: Effect of confining pressure, sample orientation, sample depth and temperature*. PSI Bericht Nr. 04-03, 2004.

40. Van Loon, L.R., W. Müller, and K. Iijima, *Activation energies of the self-diffusion of HTO, <sup>22</sup>Na<sup>+</sup> and <sup>36</sup>Cl in a highly compacted argillaceous rock (Opalinus Clay)*. Applied Geochemistry, 2005. **20**(5): p. 961-972.
41. Grolimund, D., Wang, H. A. O., Van Loon, L. R., Marone, F., Diaz, N., Kaestner, A., Jakob, A., *Microscopic chemical imaging: A key to understand ion mobility in tight formations*. The Clay Minerals Society Workshop Lectures Series. Vol. 21. 2016.
42. Langmuir, D., *Aqueous environmental geochemistry*. 1997, Prentice Hall, Upper Saddle River.
43. F. J. Pearson, D.A., A. Bath, J.-Y. Boisson, A. M. Fernández, H.-E. Gäbler, E. Gaucher, A. Gautschi, L. Griffault, P. Hernán, H. N. Waber, *Mont Terri Project – geochemistry of water in the Opalinus Clay formation at the Mont Terri Rock Laboratory*. Reports of the Federal Office for Water and Geology (FOWG), Geology Series 2003(No. 5.).
44. Wersin, P., Johnson, L. H., Schwyn, B., Berner, U., Curti, E., *Redox conditions in the near field of a repository for SF/HLW and ILW in Opalinus Clay*. Technical Report 02-13, 2003.
45. Pearson, F.J., Scholtis, A., Gautschi, A., Baeyens, B., Bradbury, M., Degueldre, C., *Chemistry of Porewater. In Mont Terri Rock Laboratory. Results of the hydrogeological, geochemical and geotechnical experiments performed in 1996 and 1997 (eds. M. Thury, P. Bossart)*. Landeshydrologie und -geologie, 1999: p. pp. 129-146.
46. Neck, V. and J.I. Kim, *Solubility and hydrolysis of tetravalent actinides*. Radiochimica Acta, 2001. **89**(1): p. 1-16.
47. Bagnoud, A., O. Leupin, B. Schwyn, and R. Bernier-Latmani, *Rates of microbial hydrogen oxidation and sulfate reduction in Opalinus Clay rock*. Applied Geochemistry, 2016. **72**: p. 42-50.
48. Bagnoud, A., K. Chourey, R.L. Hettich, I. de Bruijn, A.F. Andersson, O.X. Leupin, B. Schwyn, and R. Bernier-Latmani, *Reconstructing a hydrogen-driven microbial metabolic network in Opalinus Clay rock*. Nature Communications, 2016. **7**.
49. Fröhlich, D.R., S. Amayri, J. Drebert, D. Grolimund, J. Huth, U. Kaplan, J. Krause, and T. Reich, *Speciation of Np(V) uptake by Opalinus Clay using synchrotron microbeam techniques*. Analytical and Bioanalytical Chemistry, 2012. **404**(8): p. 2151-62.
50. Vespa, M., R. Dähn, D. Grolimund, E. Wieland, and A.M. Scheidegger, *Co speciation in hardened cement paste: A macro- and micro-spectroscopic investigation*. Environmental Science & Technology, 2007. **41**(6): p. 1902-1908.

51. Mandaliev, P., R. Dähn, B. Wehrli, and E. Wieland, *Macro- and microspectroscopic study of Nd (III) uptake mechanisms in hardened cement paste*. Environmental Science & Technology, 2009. **43**(21): p. 8462-8468.
52. Wieland, E., N. Mace, R. Dähn, D. Kunz, and J. Tits, *Macro- and micro-scale studies on U(VI) immobilization in hardened cement paste*. Journal of Radioanalytical and Nuclear Chemistry, 2010. **286**(3): p. 793-800.
53. Denecke, M.A., B. Brendebach, W. De Nolf, G. Falkenberg, K. Janssens, and R. Simon, *Spatially resolved micro-X-ray fluorescence and micro-X-ray absorption fine structure study of a fractured granite bore core following a radiotracer experiment*. Spectrochimica Acta Part B-Atomic Spectroscopy, 2009. **64**(8): p. 791-795.
54. Zhao, P.H., M. Zavarin, R.N. Leif, B.A. Powell, M.J. Singleton, R.E. Lindvall, and A.B. Kersting, *Mobilization of actinides by dissolved organic compounds at the Nevada Test Site*. Applied Geochemistry, 2011. **26**(3): p. 308-318.
55. Joseph, C., L.R. Van Loon, A. Jakob, R. Steudtner, K. Schmeide, S. Sachs, and G. Bernhard, *Diffusion of U(VI) in Opalinus Clay: Influence of temperature and humic acid*. Geochimica et Cosmochimica Acta, 2013. **109**: p. 74-89.
56. Fröhlich, D.R., S. Amayri, J. Drebert, and T. Reich, *Influence of humic acid on neptunium(V) sorption and diffusion in Opalinus Clay*. Radiochimica Acta, 2013. **101**(9): p. 553-560.
57. Husar, R., S. Weiss, C. Hennig, R. Hübner, A. Ikeda-Ohno, and H. Zänker, *Formation of neptunium(IV)-silica colloids at near-neutral and slightly alkaline pH*. Environmental Science & Technology, 2015. **49**(1): p. 665-671.
58. Siever, R., *Silicon-abundance in natural waters*, in *Handbook of Geochemistry*, K.H. Wedepohl, Editor. 1972, Springer: Berlin, Heidelberg, New York. p. pp 14-I-1-14-I-6.
59. Bradbury, M.H. and B. Baeyens, *A mechanistic description of Ni and Zn sorption on Na-montmorillonite: Part I: Titration and sorption measurements*. Journal of Contaminant Hydrology, 1997. **27**: p. 199-222.
60. Bradbury, M.H. and B. Baeyens, *Predictive sorption modelling of Ni(II), Co(II), Eu(III), Th(IV) and U(VI) on MX-80 bentonite and Opalinus Clay: A "bottom-up" approach*. Applied Clay Science, 2011. **52**(1-2): p. 27-33.
61. Bradbury, M.H. and B. Baeyens, *Sorption modelling on illite. Part II: Actinide sorption and linear free energy relationships*. Geochimica et Cosmochimica Acta, 2009. **73**(4): p. 1004-1013.
62. Bradbury, M.H. and B. Baeyens, *Experimental measurements and modeling of sorption competition on montmorillonite*. Geochimica et Cosmochimica Acta, 2005. **69**(17): p. 4187-4197.

63. Bradbury, M.H. and B. Baeyens, *Sorption modelling on illite Part I: Titration measurements and the sorption of Ni, Co, Eu and Sn*. *Geochimica et Cosmochimica Acta*, 2009. **73**(4): p. 990-1003.
64. Bradbury, M.H. and B. Baeyens, *Modelling the sorption of Zn and Ni on Ca-montmorillonite*. *Geochimica et Cosmochimica Acta*, 1999. **63**(3-4): p. 325-336.
65. Bradbury, M.H., B. Baeyens, H. Geckeis, and T. Rabung, *Sorption of Eu(III)/Cm(III) on Ca-montmorillonite and Na-illite. Part 2: Surface complexation modelling*. *Geochimica et Cosmochimica Acta*, 2005. **69**(23): p. 5403-5412.
66. Bradbury, M.H. and B. Baeyens, *Sorption of Eu on Na- and Ca-montmorillonites: Experimental investigations and modelling with cation exchange and surface*. *Geochimica et Cosmochimica Acta*, 2002. **66**(13): p. 2325-2334.
67. Bradbury, M.H. and B. Baeyens, *Modelling the sorption of Mn(II), Co(II), Ni(II), Zn(II), Cd(II), Eu(III), Am(III), Sn(IV), Th(IV), Np(V) and U(VI) on montmorillonite: Linear free energy relationships and estimates of surface binding constants for some selected heavy metals and actinides*. *Geochimica et Cosmochimica Acta*, 2005. **69**(4): p. 875-892.
68. Marques Fernandes, M., B. Baeyens, and M.H. Bradbury, *The influence of carbonate complexation on lanthanide/actinide sorption on montmorillonite*. *Radiochimica Acta*, 2008. **96**(9-11): p. 691-697.
69. Soltermann, D., B. Baeyens, M.H. Bradbury, and M. Marques Fernandes, *Fe(II) uptake on natural montmorillonites. II. surface complexation modeling*. *Environmental Science & Technology*, 2014. **48**(15): p. 8698-8705.
70. Gustafsson, J.P., *Visual MINTEQ v 3.0*. 2004, Stockholm, Sweden: Swedish Royal Institute of Technology (KTH).
71. Van Loon, L.R., P. Wersin, J.M. Soler, J. Eikenberg, T. Gimmi, P. Hernan, S. Dewonck, and S. Savoye, *In-situ diffusion of HTO, <sup>22</sup>Na<sup>+</sup>, Cs<sup>+</sup> and I in Opalinus Clay at the Mont Terri underground rock laboratory*. *Radiochimica Acta*, 2004. **92**(9-11): p. 757-763.
72. Wu, T., S. Amayri, J. Drebert, L.R. Van Loon, and T. Reich, *Neptunium(V) sorption and diffusion in Opalinus Clay*. *Environmental Science & Technology*, 2009. **43**(17): p. 6567-6571.
73. Van Loon, L.R., J.M. Soler, W. Müller, and M.H. Bradbury, *Anisotropic diffusion in layered argillaceous rocks: A case study with Opalinus Clay*. *Environmental Science & Technology*, 2004. **38**(21): p. 5721-5728.
74. Fanghänel, T., V. Neck, and J.I. Kim, *The ion product of H<sub>2</sub>O, dissociation constants of H<sub>2</sub>CO<sub>3</sub> and Pitzer parameters in the system Na<sup>+</sup>/H<sup>+</sup>/OH<sup>-</sup>/HCO<sub>3</sub><sup>-</sup>/CO<sub>3</sub><sup>2-</sup>/ClO<sub>4</sub><sup>-</sup>/H<sub>2</sub>O at 25°C*. *Journal of Solution Chemistry*, 1996. **25**(4): p. 327-343.

75. Yaroshchuk, A.E. and L.R. Van Loon, *Improved interpretation of in-diffusion measurements with confined swelling clays*. Journal of Contaminant Hydrology, 2008. **97**(1-2): p. 67-74.
76. Grolimund, D., M. Senn, M. Trottmann, M. Janousch, I. Bonhoure, A.M. Scheidegger, and M. Marcus, *Shedding new light on historical metal samples using micro-focused synchrotron X-ray fluorescence and spectroscopy*. Spectrochimica Acta Part B-Atomic Spectroscopy, 2004. **59**(10-11): p. 1627-1635.
77. <https://www.psi.ch/media/the-swiss-light-source-sls>. 16.11.16.
78. Teo, B.K., *EXAFS: Basic principle and data analysis*. Springer Verlag, 1986.
79. Koningsberger, D.C., B.L. Mojet, G.E. van Dorssen, and D.E. Ramaker, *XAFS spectroscopy; fundamental principles and data analysis*. Topics in Catalysis, 2000. **10**(3-4): p. 143-155.
80. Reich, T., G. Bernhard, G. Geipel, H. Funke, C. Hennig, A. Rossberg, W. Matz, N. Schell, and H. Nitsche, *The Rossendorf Beam Line ROBL - a dedicated experimental station for XAFS measurements of actinides and other radionuclides*. Radiochimica Acta, 2000. **88**(9-11): p. 633-637.
81. Mori, C., T. Suzuki, S. Koido, H. Miyahara, A. Uritani, T. Aoyama, and K. Nishizawa, *Measurement of the radioactivity distribution of material-surfaces with an imaging plate*. Nuclear Instruments & Methods in Physics Research Section a-Accelerators Spectrometers Detectors and Associated Equipment, 1994. **353**(1-3): p. 371-374.
82. Amemiya, Y. and J. Miyahara, *Imaging plate illuminates many fields*. Nature, 1988. **336**(6194): p. 89-90.
83. Fröhlich, D.R., S. Amayri, J. Drebert, and T. Reich, *Influence of temperature and background electrolyte on the sorption of neptunium(V) on Opalinus Clay*. Applied Clay Science, 2012. **69**: p. 43-49.
84. Runde, W., S.D. Conradson, D.W. Efurud, N. Lu, C.E. VanPelt, and C.D. Tait, *Solubility and sorption of redox-sensitive radionuclides (Np, Pu) in J-13 water from the Yucca Mountain site: comparison between experiment and theory*. Applied Geochemistry, 2002. **17**: p. 837-853.
85. Seibert, A., A. Mansel, C.M. Marquardt, H. Keller, J.V. Kratz, and N. Trautmann, *Complexation behaviour of neptunium with humic acid*. Radiochimica Acta, 2001. **89**(8): p. 505-510.
86. Amayri, S., A. Jermolajev, and T. Reich, *Neptunium(V) sorption on kaolinite*. Radiochimica Acta, 2011. **99**(6): p. 349-357.
87. Poinssot, C., Baeyens, B., Bradbury, M. H., *Experimental studies of Cs, Sr, Ni, and Eu sorption on Na-illite and the modelling of Cs sorption*. PSI Bericht Nr. 99-06, 1999.

88. Moll, W.F., *Baseline studies of The Clay Minerals Society Source Clays: Geological origin*. Clays and Clay Minerals, 2001. **49**(5): p. 374-380.
89. Chipera, S.J. and D.L. Bish, *Baseline studies of The Clay Minerals Society Source Clays: Powder X-ray diffraction analyses*. Clays and Clay Minerals, 2001. **49**(5): p. 398-409.
90. Kogel, J.E. and S.A. Lewis, *Baseline studies of The Clay Minerals Society Source Clays: Chemical analysis by inductively coupled plasma-mass spectroscopy (ICP-MS)*. Clays and Clay Minerals, 2001. **49**(5): p. 387-392.
91. Mermut, A.R. and A.F. Cano, *Baseline studies of The Clay Minerals Society Source Clays: Chemical analyses of major elements*. Clays and Clay Minerals, 2001. **49**(5): p. 381-386.
92. Niitsu, Y., S. Sato, H. Ohashi, Y. Sakamoto, S. Nagao, T. Ohnuki, and S. Muraoka, *Effects of humic acid on the sorption of neptunium(V) on kaolinite*. Journal of Nuclear Materials, 1997. **248**: p. 328-332.
93. Schmeide, K. and G. Bernhard, *Sorption of Np(V) and Np(IV) onto kaolinite: Effects of pH, ionic strength, carbonate and humic acid*. Applied Geochemistry, 2010. **25**(8): p. 1238-1247.
94. Pruetz, R.J. and H.L. Webb, *Sampling and analysis of KGa-1B well-crystallized kaolin source clay*. Clays and Clay Minerals, 1993. **41**(4): p. 514-519.
95. Payne, T.E., J.A. Davis, G.R. Lumpkin, R. Chisari, and T.D. Waite, *Surface complexation model of uranyl sorption on Georgia kaolinite*. Applied Clay Science, 2004. **26**(1-4): p. 151-162.
96. Gualda, G.A.R., A.S. Pamukcu, L.L. Claiborne, and M.L. Rivers, *Quantitative 3D petrography using X-ray tomography 3: Documenting accessory phases with differential absorption tomography*. Geosphere, 2010. **6**(6): p. 782-792.
97. Tsuchiyama, A., K. Uesugi, T. Nakano, and S. Ikeda, *Quantitative evaluation of attenuation contrast of X-ray computed tomography images using monochromatized beams*. American Mineralogist, 2005. **90**(1): p. 132-142.
98. Joseph, C., K. Schmeide, S. Sachs, V. Brendler, G. Geipel, and G. Bernhard, *Sorption of uranium(VI) onto Opalinus Clay in the absence and presence of humic acid in Opalinus Clay pore water*. Chemical Geology, 2011. **284**(3-4): p. 240-250.
99. Rasband, W. *ImageJ 1.48v*. 2016.
100. Rosemann, J., *Einfluss der Salinität auf die Sorption von Np(V) an Opalinuston, Diplomarbeit*. Insitut für Kernchemie 2012, Mainz: Johannes Gutenberg Universität Mainz.



101. Gorgeon, L., *Contribution à la modélisation physico-chimique de la rétention de radioéléments à vie longue par des matériaux argileux*, PhD Thesis, 1994, Université Paris 6.
102. Marsac, R., N.L. Banik, J. Lützenkirchen, C.M. Marquardt, K. Dardenne, D. Schild, J. Rothe, A. Diascorn, T. Kupcik, T. Schäfer, and H. Geckeis, *Neptunium redox speciation at the illite surface*. *Geochimica et Cosmochimica Acta*, 2015. **152**: p. 39-51.
103. Amayri, S., D.R. Fröhlich, U. Kaplan, N. Trautmann, and T. Reich, *Distribution coefficients for the sorption of Th, U, Np, Pu, and Am on Opalinus Clay*. *Radiochimica Acta*, 2016. **104**(1).
104. Krepelova, A., S. Sachs, and G. Bernhard, *Uranium(VI) sorption onto kaolinite in the presence and absence of humic acid*. *Radiochimica Acta*, 2006. **94**(12): p. 825-833.
105. Fröhlich, D.R., S. Amayri, J. Drebert, and T. Reich, *Sorption of neptunium(V) on Opalinus Clay under aerobic/anaerobic conditions*. *Radiochimica Acta*, 2011. **99**(2): p. 71-77.

## LIST OF FIGURES

Figure 1: Radiotoxicity of the activity inventory per tHM from ingestion (4% $^{235}\text{U}$ , burn-up: 40 GWd/t) [1].....	3
Figure 2: Schematic illustration of the multi-barrier concept for deep geological disposal [15]. .....	6
Figure 3: Overview of the salt and argillaceous rock formations suitable for a repository in Germany [23]. .....	9
Figure 4: Schematic view of different types of pore water in Opalinus Clay, modified from [20]. .....	11
Figure 5: Schematic picture of the pore space of compacted bentonite and the effect of mechanical compaction and changes of ionic strength on the pore space. The total pore space equals the interlayer and the interparticle pore space. The interparticle pore space equals the double layer pore space (3) and the free pore space (4). Anion diffusion takes place in the free water pore space [31]. .....	12
Figure 6: Schematic view of the anisotropy of OPA with respect to diffusion [39].....	14
Figure 7: “Three-dimensional visualization of undisturbed reactive solute transport pattern and geochemical heterogeneity in an Opalinus Clay rock sample” [41]. The chemical nature of the components was assigned based on combined $\mu$ -XRF and $\mu$ -XRD results. The reactive transport pattern of Cs after in-diffusion is achieved by absorption-edge contrast tomography.....	14
Figure 8: Pourbaix diagram for the system $\text{Np-O}_2\text{-H}_2\text{O}$ at 25 °C [42]. .....	15
Figure 9: Schematic picture of major redox-active phases present in technical barrier and host rock [44]. .....	16
Figure 10: The left side shows normalized Np $L_{\text{III}}$ -edge $\mu$ -XANES spectra of the marked spots on the $\mu$ -XRF scan on the right side (500 × 500 $\mu\text{m}$ , step size of 5 $\mu\text{m}$ ; $E = 17,700 \text{ eV}$ ) performed on an OPA thin section sample contacted with Np(V) [49]. .....	17
Figure 11: Schematic representation of the experimental set-up of a through-diffusion experiment (top) [39] and the corresponding experimental realization in the laboratory. 19	19
Figure 12: Sample results of an HTO through-diffusion experiment. Flux $J$ and accumulated activity of HTO in the low concentration reservoir plotted against the time in days. ....	21
Figure 13: Overview of the SLS beamlines (left), aerial view of the SLS (top right) and the schematic depiction of the synchrotron radiation emitted by undulators (bottom right) [77]. .....	24

Figure 14: Standard $\mu$ -XAS experimental setup in the experimental safety hutch of a beamline in a synchrotron facility (left) [76] and at the SLS, before the final sample adjustment (right). .....	24
Figure 15: Interaction of X-rays with the electron shell of an atom [78]......	25
Figure 16: Constructive and destructive interferences in dependency of the wavelength of the photoelectron (left) [79]. XANES spectra of the $L_{III}$ -absorption edge of aquatic Np(IV) and Np(V) species were measured by Reich et al. and used as reference spectra (right) [80]......	26
Figure 17: Drawing of the measuring arrangement of vegetables for IP exposure for 192 h [81]......	27
Figure 18: Preparation of the diffusion profile samples from OPA bore cores (diameter 2.54 cm, height in this case 5 mm). When possible, the bore cores were cleaved (dotted lines) along the bedding as it was eased. ....	43
Figure 19: X-ray fluorescence spectrum of the elements contained in OPA. Labelled are the recorded ROIs. Marked in red, is the ROI of the Np $L\alpha$ fluorescence, which is located on the $K\alpha$ Line of Sr.....	44
Figure 20: Visualization of the calculation of the Np intensities by subtraction of scans with an excitation energy below the Np $L_{III}$ -edge (17.55 keV) of those above the Np $L_{III}$ -edge (17.62 keV) of the same area (step size 10 $\mu$ m). ....	45
Figure 21: Measuring arrangements with a) several radioactive bore core fragments set in boreholes in a Plexiglas plate, which was subsequently covered with an IP, b) a bore core on an IP, and c) an IP wrapped around a bore core to investigate the clay/steel cylinder interface.....	46
Figure 22: Preparation of diffusion profile samples for IP measurement from diffusion of $8 \times 10^{-6}$ M Np into OPA. The dotted line indicates the cleave locations, the red line the interface between the bore core and the Np solution of the primary reservoir. ....	47
Figure 23: Diffusion profile positioning on the IP. The red lines indicate the radioactive interfaces. ....	48
Figure 24: Sorption isotherm for the sorption of $8 \times 10^{-6}$ M Np(V) on Na-illite in 0.1, 1.0, and 2.6 M NaCl solution at pH 7.6 under ambient air conditions. ....	50
Figure 25: Plotted log $K_d$ values (with $K_d$ in L/kg) of the sorption of $8 \times 10^{-6}$ M Np(V) on $\sim$ 4 g/L Na-illite in 0.1 and 3.0 M NaCl solution under ambient air conditions, together with data of Gorgeon for $1.1 \times 10^{-6}$ M Np(V) on $\sim$ 9 g/L Na-illite in 0.1 M NaClO <sub>4</sub> solution [101]......	51

Figure 26: Log $K_d$ values ( $K_d$ in L/kg) for the sorption of $8 \times 10^{-6}$ M Np(V) on untreated KGa-1b (4 g/L) and treated KGa-1b ( $\sim 2.5$ g/L) in 0.1 M NaClO <sub>4</sub> solution under ambient air conditions. The dotted line represents sorption below 5%. .....	52
Figure 27: Log $K_d$ values for the sorption of $8 \times 10^{-6}$ M Np(V) on 0.2 and 2 g/L anatase at pH 8 under ambient air conditions in 0.1 M NaCl solution. The sorption for the sample with 0.02 g/L was below the detection limit. ....	53
Figure 28: Results of the IP measurement (5 h) of the primary (P) and secondary (S) sites of the OPA bore core of cell 28.....	56
Figure 29: 360° image of the outside clay/steel cylinder interface of the bore core (cell 28). This was investigated with an IP wrapped (5 h) around the bore core with the primary site at the bottom side of the IP. ....	56
Figure 30: Comparison of the IP exposure (72 h) of the primary sites of the cells Np-1 and Np-2. ....	58
Figure 31: Measuring arrangement of the cleaved OPA samples of Np-1/2/3 and the resulting IP image after 72 h of exposure. ....	58
Figure 32: Results of the diffusion profile analysis with IPs of the diffusion experiments Np-1/2/3. ....	59
Figure 33: The red, green, and grey lines show the diffusion profiles of the cells Np-1/2/3 from IP measurement, the dotted lines indicates the exponential fits of the background and the open circles represent the corrected diffusion profiles, providing the Np diffusion profiles with the final diffusion depth.....	59
Figure 34: Comparison of the results from IP measurements (circles) and from modeling of the $\mu$ -XRF data of samples Np-1/2/3. ....	60
Figure 35: Np diffusion profiles from IP measurements with the results from diffusion modeling for the samples Np-1/2/3.....	61

## LIST OF TABLES

Table 1: Average inventory of spent nuclear fuel in Germany, one year after removal from a reactor with initial 4% $^{235}\text{U}$ and a burn-up of 40 GWd/t [1].....	2
Table 2: Half-life, activity inventory, and effective dose factor for ingestion of long-lived radionuclides contained in spent nuclear fuel [1]. .....	3
Table 3: Overview on the isolation properties of typical host rock formations as geological barriers [15].....	8
Table 4: Composition of OPA PW [24] compared to the mine water at pit Konrad [25].....	10
Table 5: Chemical results in wt.% of (crude) KGa-1b measured by XFA [94].....	41
Table 6: Cation exchange capacity (CEC) and specific surface area of conditioned Na-illite and OPA.....	45
Table 7: Surface complexation constants for the sorption of Np(V) on the strong sorption sites of Na-illite and the cation exchange ( $I = 0.1 \text{ M NaCl}$ ). .....	50
Table 8: Chemical composition of treated/untreated kaolinite KGa-1b determined by XRF analysis in wt.%. .....	53
Table 9: Sorption of $8 \times 10^{-6} \text{ M Np(V)}$ at pH 8 (see Figure 26) with regard to the total amount of KGa-1b (left column) or only the fraction of contained anatase in KGa-1b (1.636 wt.%, right column). .....	54
Table 10: $K_d$ values and conversion factors $CF_i$ used for the calculation of the bottom-up approach for the uptake of Np(V) on OPA. Furthermore, the related literature value and the most important experimental details are given. ....	55
Table 11: Short description of the diffusion experiment of cell 28. ....	56
Table 12: Results for the diffusion profile modeling obtained from $\mu$ -XRF and IP analysis..	61
Table 13: Results from the different Np(V) diffusion experiments with regard to $\alpha$ , $D_e$ , and $\log K_d$ . The values in brackets are from the related batch sorption experiments. The abbreviation “AP” behind the first three cell names stands for the applied abrasive peeling method in contrast to the parameter determination by $\mu$ -XRF. ....	64

## **ACKNOWLEDGEMENT**

Diese Seite wurde aus datenschutzrechtlichen Gründen gelöscht

## CURRICULUM VITAE

---



**Jonathan Börner**

Formerly Jonathan Rosemann

Born on 20th January 1985  
in Kirchheimbolanden,  
married,  
two children

### Work experience

---

since 05/2017     Engineer at Safetec in Heidelberg. Assistance of the full system decontamination of the primary heat circuit of the nuclear power plant Biblis Block B for RWE.

### Education

---

since 11/2012     PhD student at the Institute of Nuclear Chemistry, Johannes Gutenberg-University Mainz, Germany, with the topic of the dissertation „Diffusion of Np in natural argillaceous host rock“

04/2005 – 09/2012     Study of chemistry at the Johannes Gutenberg-University, Mainz, Germany best grade „sehr gut“  
Diploma thesis „Influence of salinity on the sorption of Np(V) on natural argillaceous host rock“ at the Institute of Nuclear Chemistry, Johannes Gutenberg-University, Mainz, Germany

### Scientific projects

---

- Teaching at „Kernchemisches Praktikum I“ and mentor of student internships und degree theses

- Attendance at the following Summer Schools of the scientific field of research:
  - "Talisman Summer School 2014 and Plenary Meeting" in Avignon, France (06/2014)
  - "BMBF and 8<sup>th</sup> European Summer School" in Bonn, Germany (07/2014)
- Attendance and talks at following workshops:
 

Semi-annual workshops of the cooperative project "retention of long-lived radionuclides in natural argillaceous host rock and saline systems", „TRePro III Workshop“ in Karlsruhe (03/2014), AnXAS Workshop in Böttstein, Schweiz (05/2014 with best poster award), Seminar of the Institut für Nukleare Entsorgung in Karlsruhe (04/2016)
- EU funded **beamtime** at the microXAS beamline of the Swiss Light Source, PSI, Villigen, Switzerland:
  - „Speciation of Np along diffusion pathways in Opalinus Clay using micro-XAFS and micro-XRF“ (10/2013)
  - "Time series of Np(V) diffusion profile in opaline clay" (05/2015)

## Civilian service

---

05/2004 – 02/2005    Museum of Natural History Mainz

## School education

---

09/1995 – 03/2004    Bischöfliches Willigis Gymnasium Mainz, advanced courses of chemistry, mathematics and geography

## Linguistic and cultural stays

---

2006 und 2010    South Asia 4 months  
 2008    South America 3 months